

CMS Draft Analysis Note

The content of this note is intended for CMS internal use and distribution only

2021/02/08

Archive Hash: 86358e0-D

Archive Date: 2020/12/09

Measurements of Higgs differential cross section and interpretations in $H \rightarrow ZZ \rightarrow 4\ell (\ell = e, \mu)$ channel

M. Bonanomi², M.S. Chen¹, Q.Y. Guo^{1,4}, T. Javaid^{1,4}, P. Milenovic⁵, V. Milosevic⁵, M. Ahmad⁷, C. Ochando², G. Ortona², R. Salerno², R. Sharma¹, T. Sculac³, and D. Sperka⁶

¹ IHEP, Beijing

² Laboratoire Leprince-Ringuet

³ University of Split

⁴ Beihang University

⁵ University of Belgrade

⁶ Boston University

⁷ Tsinghua University

Abstract

Properties of the Higgs boson are measured in the $H \rightarrow ZZ \rightarrow 4\ell (\ell = e, \mu)$ decay channel. A data sample of proton-proton collisions at a center-of-mass energy of 13 TeV is used, corresponding to an integrated luminosity of 137 fb^{-1} recorded by the CMS detector at the LHC. The fiducial cross section is measured with respect to several observables sensitive to production and decay of Higgs where the observed results are compared with POWHEG, MADGRAPH5 and NNLOPS theory predictions. The possible interpretations of the results are reported.

This box is only visible in draft mode. Please make sure the values below make sense.

PDFAuthor:	Tahir Javaid
PDFTitle:	Measurements of Higgs differential cross section and interpretations in HZZ4 "(=e,") channel
PDFSubject:	CMS
PDFKeywords:	CMS, your topics

Please also verify that the abstract does not use any user defined symbols

1 Acknowledgments**2 Contents**

3	1	Introduction	2
4	2	Datasets, simulation samples and theoretical predictions	3
5	2.1	Triggers and Datasets	3
6	2.2	Simulation samples and theoretical predictions	6
7	3	Objects	8
8	3.1	Electrons	8
9	3.2	Muons	8
10	3.3	Photons for FSR recovery	9
11	3.4	Jets	9
12	4	Signal Modelling	13
13	5	Background Estimation	14
14	5.1	Estimation of ZZ normalization from Data	14
15	6	Analysis Strategy	15
16	6.1	Event Selection	15
17	6.2	Fiducial Volume Significance and Definition	16
18	6.3	Unfolding	17
19	6.4	Acceptance and other correction factors	17
20	6.5	Statistical Procedure	20
21	6.6	Extraction of differential $H \rightarrow 4\ell$ cross section	21
22	6.7	Effective Field Theory interpretations for Differential measurements	25
23	7	Systematic uncertainties	27
24	7.1	Systematic uncertainties treatment when combining the data sets	28
25	8	Results	33
26	8.1	Yields and distributions	33
27	8.2	Differential Cross Sections measurement results	37
28	8.3	Double differential cross section measurements	41
29	8.4	Effective Field Theory interpretations	41
30	A	Signal Shapes and Efficiencies	42
31	A.1	Differential bins - Higgs boson transverse momentum	42
32	A.2	Differential bins - rapidity of the Higgs boson	60
33	A.3	Signal fits in differential bins - number of jets	63

34 1 Introduction

35 The ATLAS and CMS collaborations first reported the discovery of a new boson in 2012 [1,
36 2] consistent with the standard model (SM) Higgs boson [3–8] based on proton-proton (pp)
37 collisions delivered by the CERN LHC at a center-of-mass energy of $\sqrt{s} = 7\text{ TeV}$ in years 2011
38 and 8 TeV in 2012. Subsequent studies by CMS using the full LHC Run 1 data set in various
39 decay channels and production modes and combined measurements from ATLAS and CMS
40 [9–12] showed that the properties of the new boson are so far consistent with expectations for
41 the SM Higgs boson.

42 The $H \rightarrow ZZ \rightarrow 4\ell$ decay channel ($\ell = e, \mu$) has a large signal-to-background ratio due to the
43 complete reconstruction of the final state decay products and excellent lepton momentum res-
44 olution and is one of the most important channels for studies of the Higgs boson’s properties.
45 Measurements performed using this decay channel and the Run 1 data set include the deter-
46 mination of the mass and spin-parity of the new boson [13–15], its width [16, 17] and fiducial
47 cross sections [18], as well as tests for anomalous HVV couplings [15, 17].

48 In this document we present measurements of the differential fiducial cross sections for the
49 Higgs boson production in the $H \rightarrow ZZ \rightarrow 4\ell$ decay channel at $\sqrt{s} = 13\text{ TeV}$ using 137 fb^{-1} of
50 pp collision data collected with the CMS experiment at the LHC in 2016, 2017 and 2018. Differ-
51 ential measurements for Higgs production variables have already been studied and published
52 under [19]. In this analysis, in addition, the full available dataset has been fully re-analyzed,
53 with several improvements:

- 54 • Analysis Ultra Legacy data.
- 55 • Revised measurement of lepton scale factors (Section 3.2.3)
- 56 • several additional (production and as well as decay) observables studied with opti-
57 mized binning.
- 58 • in addition to POWHEG AND NNLOPS, MADGRAPH5 IS USED AS ADDITIONAL
59 THEORY PREDICTION TO FOR COMPARISION OF THE OBSERVED RESULTS.
- 60 • EFFECTIVE FIELD THEORY (EFT) INTERPRETATIONS OF DIFFERENTIAL MEASURE-
61 MENTS ARE ALSO PRESENTED.

2 Datasets, simulation samples and theoretical predictions

2.1 Triggers and Datasets

This analysis uses a ultra legacy data sample recorded by the CMS experiment during 2016, 2017 and 2018, corresponding to 137 fb^{-1} of data.

The datasets used for 2016, 2017 and 2018 data taking are listed in Tables 1, 3, and 5, respectively, along with the integrated luminosity. The analysis relies on four different primary datasets (PDs), *DoubleMuon*, *MuEG*, *EGamma* (or *DoubleEG* and *SingleElectron* for 2016 and 2017), and *SingleMuon*, each of which combines a certain collections of HLT paths. To avoid duplicate events from different primary datasets, events are taken:

- from EGamma if they pass the diEle or triEle or singleElectron triggers,
- from DoubleMuon if they pass the diMuon or triMuon triggers and fail the diEle and triEle triggers,
- from MuEG if they pass the MuEle or MuDiEle or DiMuEle triggers and fail the diEle, triEle, singleElectron, diMuon and triMuon triggers,
- from SingleMuon if they pass the singleMuon trigger and fail all the above triggers.

The HLT paths used for 2016, 2017 and 2018 collision data are listed in Tables 2, 4 and 6, respectively.

Run-range	Dataset	Integrated luminosity
272007-275376	/DoubleMuon/Run2016C-21Feb2020_UL2016_HIPM-v1/MINIAOD /DoubleMuon/Run2016B-21Feb2020_ver1_UL2016_HIPM-v1/MINIAOD /MuonEG/Run2016B-21Feb2020_ver1_UL2016_HIPM-v1/MINIAOD /SingleElectron/Run2016B-21Feb2020_ver1_UL2016_HIPM-v1/MINIAOD /SingleMuon/Run2016B-21Feb2020_ver1_UL2016_HIPM-v1/MINIAOD	5.892 fb^{-1}
275657-276283	/DoubleMuon/Run2016C-17Jul2018-v1/MINIAOD /DoubleEG/Run2016C-21Feb2020_UL2016_HIPM-v1/MINIAOD /MuonEG/Run2016C-21Feb2020_UL2016_HIPM-v1/MINIAOD /SingleElectron/Run2016C-21Feb2020_UL2016_HIPM-v1/MINIAOD /SingleMuon/Run2016C-21Feb2020_UL2016_HIPM-v1/MINIAOD	2.646 fb^{-1}
276315-276811	/DoubleEG/Run2016D-21Feb2020_UL2016_HIPM-v1/MINIAOD /DoubleMuon/Run2016D-21Feb2020_UL2016_HIPM-v1/MINIAOD /MuonEG/Run2016D-21Feb2020_UL2016_HIPM-v1/MINIAOD /SingleElectron/Run2016D-21Feb2020_UL2016_HIPM-v1/MINIAOD /SingleMuon/Run2016D-21Feb2020_UL2016_HIPM-v1/MINIAOD	4.353 fb^{-1}
276831-277420	/DoubleEG/Run2016E-21Feb2020_UL2016_HIPM-v1/MINIAOD /DoubleMuon/Run2016E-21Feb2020_UL2016_HIPM-v1/MINIAOD /MuonEG/Run2016E-21Feb2020_UL2016_HIPM-v1/MINIAOD /SingleElectron/Run2016E-21Feb2020_UL2016_HIPM-v1/MINIAOD /SingleMuon/Run2016E-21Feb2020_UL2016_HIPM-v1/MINIAOD	4.117 fb^{-1}
277772-278808	/DoubleEG/Run2016F-21Feb2020_UL2016_v1/MINIAOD /DoubleMuon/Run2016F-21Feb2020_UL2016_v1/MINIAOD /MuonEG/Run2016F-21Feb2020_UL2016_v1/MINIAOD /SingleElectron/Run2016F-21Feb2020_UL2016_v1/MINIAOD /SingleMuon/Run2016F-21Feb2020_UL2016_v1/MINIAOD	3.186 fb^{-1}
278820-280385	/DoubleEG/Run2016G-21Feb2020_UL2016_v1/MINIAOD /DoubleMuon/Run2016G-21Feb2020_UL2016_v1/MINIAOD /MuonEG/Run2016G-21Feb2020_UL2016_v1/MINIAOD /SingleElectron/Run2016G-21Feb2020_UL2016_v1/MINIAOD /SingleMuon/Run2016G-21Feb2020_UL2016_v1/MINIAOD	7.721 fb^{-1}
280919-284044	/DoubleEG/Run2016H-21Feb2020_UL2016_v1/MINIAOD /DoubleMuon/Run2016H-21Feb2020_UL2016_v1/MINIAOD /MuonEG/Run2016H-21Feb2020_UL2016_v1/MINIAOD /SingleElectron/Run2016H-21Feb2020_UL2016_v2/MINIAOD /SingleMuon/Run2016H-21Feb2020_UL2016_v1/MINIAOD	8.857 fb^{-1}

Table 1: Datasets used in the 2016 analysis.

HLT path	prescale	primary dataset
HLT_Ele17_Ele12_CaloIdL_TrackIdL_IsoVL_DZ	1	DoubleEG
HLT_Ele23_Ele12_CaloIdL_TrackIdL_IsoVL_DZ	1	DoubleEG
HLT_DoubleEle33_CaloIdL_GsfTrkIdVL	1	DoubleEG
HLT_Ele16_Ele12_Ele8_CaloIdL_TrackIdL	1	DoubleEG
HLT_Mu17_TrkIsoVVL_Mu8_TrkIsoVVL	1	DoubleMuon
HLT_Mu17_TrkIsoVVL_TkMu8_TrkIsoVVL	1	DoubleMuon
HLT_TripleMu_12_10_5	1	DoubleMuon
HLT_Mu8_TrkIsoVVL_Ele17_CaloIdL_TrackIdL_IsoVL	1	MuonEG
HLT_Mu8_TrkIsoVVL_Ele23_CaloIdL_TrackIdL_IsoVL	1	MuonEG
HLT_Mu17_TrkIsoVVL_Ele12_CaloIdL_TrackIdL_IsoVL	1	MuonEG
HLT_Mu23_TrkIsoVVL_Ele12_CaloIdL_TrackIdL_IsoVL	1	MuonEG
HLT_Mu23_TrkIsoVVL_Ele8_CaloIdL_TrackIdL_IsoVL	1	MuonEG
HLT_Mu8_DiEle12_CaloIdL_TrackIdL	1	MuonEG
HLT_DiMu9_Ele9_CaloIdL_TrackIdL	1	MuonEG
HLT_Ele25_eta2p1_WPTight	1	SingleElectron
HLT_Ele27_WPtight	1	SingleElectron
HLT_Ele27_eta2p1_WPLoose_Gsf	1	SingleElectron
HLT_IsoMu20 OR HLT_IsoTkMu20	1	SingleMuon
HLT_IsoMu22 OR HLT_IsoTkMu22	1	SingleMuon

Table 2: Trigger paths used in 2016 collision data.

Run-range	Dataset	Integrated luminosity
297046-299329	/DoubleMuon/Run2017B-UL2017_MiniAODv2-v1/MINIAOD /DoubleEG/Run2017B-09Aug2019_UL2017-v1/MINIAOD /MuonEG/Run2017B-UL2017_MiniAODv2-v1/MINIAOD /SingleElectron/Run2017B-UL2017_MiniAODv2-v1/MINIAOD /SingleMuon/Run2017B-09Aug2019_UL2017-v1/MINIAOD	4.792 fb ⁻¹
299368-300676	/DoubleMuon/Run2017C-UL2017_MiniAODv2-v1/MINIAOD /DoubleEG/Run2017C-UL2017_MiniAODv2-v2/MINIAOD /MuonEG/Run2017C-UL2017_MiniAODv2-v1/MINIAOD /SingleElectron/Run2017C-UL2017_MiniAODv2-v1/MINIAOD /SingleMuon/Run2017C-09Aug2019_UL2017-v1/MINIAOD	9.755 fb ⁻¹
302030-303434	/DoubleMuon/Run2017D-UL2017_MiniAODv2-v1/MINIAOD /DoubleEG/Run2017D-UL2017_MiniAODv2-v1/MINIAOD /MuonEG/Run2017D-UL2017_MiniAODv2-v1/MINIAOD /SingleElectron/Run2017D-09Aug2019_UL2017-v1/MINIAOD /SingleMuon/Run2017D-09Aug2019_UL2017-v1/MINIAOD	4.319 fb ⁻¹
303824-304797	/DoubleMuon/Run2017E-09Aug2019_UL2017-v1/MINIAOD /DoubleEG/Run2017E-UL2017_MiniAODv2-v1/MINIAOD /MuonEG/Run2017E-UL2017_MiniAODv2-v1/MINIAOD /SingleElectron/Run2017E-UL2017_MiniAODv2-v1/MINIAOD /SingleMuon/Run2017E-09Aug2019_UL2017-v1/MINIAOD	9.424 fb ⁻¹
305040-306462	/DoubleMuon/Run2017F-UL2017_MiniAODv2-v1/MINIAOD /DoubleEG/Run2017F-09Aug2019_UL2017-v1/MINIAOD /MuonEG/Run2017F-UL2017_MiniAODv2-v1/MINIAOD /SingleElectron/Run2017F-UL2017_MiniAODv2-v1/MINIAOD /SingleMuon/Run2017F-09Aug2019_UL2017-v1/MINIAOD	13.50 fb ⁻¹
278820-280385	/DoubleMuon/Run2017G-09Aug2019_UL2017-v1/MINIAOD /DoubleEG/Run2017G??_MINIAOD /MuonEG/Run2017G??_MINIAOD /SingleElectron/Run2017G??_MINIAOD /SingleMuon/Run2017G?_MINIAOD	7.721 fb ⁻¹
281207-284068	/DoubleMuon/Run2017H-UL2017_MiniAODv2-v1/MINIAOD /DoubleEG/Run2017??_MINIAOD /MuonEG/Run2017H??_MINIAOD /SingleElectron/Run2017H??_MINIAOD /SingleMuon/Run2017H??_MINIAOD	8.857 fb ⁻¹

Table 3: Datasets used in the 2017 analysis.

HLT path	prescale	primary dataset
HLT_Ele23_Ele12_CaloIdL_TrackIdL_IsoVL_*	1	DoubleEG
HLT_DoubleEle33_CaloIdL_GsfTrkIdVL	1	DoubleEG
HLT_Ele16_Ele12_Ele8_CaloIdL_TrackIdL	1	DoubleEG
HLT_Mu17_TrkIsoVVL_Mu8_TrkIsoVVL_DZ_Mass3p8	1	DoubleMuon
HLT_Mu17_TrkIsoVVL_Mu8_TrkIsoVVL_DZ_Mass8	1	DoubleMuon
HLT_TripleMu_12_10_5	1	DoubleMuon
HLT_TripleMu_10_5_5_D2	1	DoubleMuon
HLT_Mu23_TrkIsoVVL_Ele12_CaloIdL_TrackIdL_IsoVL	1	MuonEG
HLT_Mu8_TrkIsoVVL_Ele23_CaloIdL_TrackIdL_IsoVL_DZ	1	MuonEG
HLT_Mu12_TrkIsoVVL_Ele23_CaloIdL_TrackIdL_IsoVL_DZ	1	MuonEG
HLT_Mu23_TrkIsoVVL_Ele12_CaloIdL_TrackIdL_IsoVL_DZ	1	MuonEG
HLT_DiMu9_Ele9_CaloIdL_TrackIdL_DZ	1	MuonEG
HLT_Mu8_DiEle12_CaloIdL_TrackIdL	1	MuonEG
HLT_Mu8_DiEle12_CaloIdL_TrackIdL_DZ	1	MuonEG
HLT_Ele35_WPTight_Gsf_v*	1	SingleElectron
HLT_Ele38_WPTight_Gsf_v*	1	SingleElectron
HLT_Ele40_WPTight_Gsf_v*	1	SingleElectron
HLT_IsoMu27	1	SingleMuon

Table 4: Trigger paths used in 2017 collision data.

Run-range	Dataset	Integrated luminosity
315252-316995	/DoubleMuon/Run2018A-UL2018_MiniAODv2-v1/MINIAOD /MuonEG/Run2018A-12Nov2019_UL2018_rsb-v1/MINIAOD /EGamma/Run2018A-12Nov2019_UL2018-v2/MINIAOD /SingleMuon/Run2018A-UL2018_MiniAODv2-v1/MINIAOD	X.XXX fb ⁻¹
317080-319310	/DoubleMuon/Run2018B-UL2018_MiniAODv2-v2/MINIAOD /MuonEG/Run2018B-12Nov2019_UL2018-v1/MINIAOD /EGamma/Run2018B-UL2018_MiniAODv2-v1/MINIAOD /SingleMuon/Run2018B-12Nov2019_UL2018-v2/MINIAOD	X.XXX fb ⁻¹
319337-320065	/DoubleMuon/Run2018C-12Nov2019_UL2018-v2/MINIAOD /MuonEG/Run2018C-12Nov2019_UL2018-v1/MINIAOD /EGamma/Run2018C-UL2018_MiniAODv2-v1/MINIAOD /SingleMuon/Run2018C-12Nov2019_UL2018-v2/MINIAOD	X.XXX fb ⁻¹
320673-325175	/DoubleMuon/Run2018D-UL2018_MiniAODv2-v1/MINIAOD /MuonEG/Run2018D-12Nov2019_UL2018_rsb-v1/MINIAOD /EGamma/Run2018D-UL2018_MiniAODv2-v1/MINIAOD /SingleMuon/Run2018D-12Nov2019_UL2018-v4/MINIAOD	X.XXX fb ⁻¹

Table 5: Datasets used in the 2018 analysis.

HLT path	prescale	primary dataset
HLT_Ele23_Ele12_CaloIdL_TrackIdL_IsoVL_v*	1	DoubleEG
HLT_DoubleEle25_CaloIdL_MW_v*	1	DoubleEG
HLT_Mu17_TrkIsoVVL_Mu8_TrkIsoVVL_DZ_Mass3p8_v*	1	DoubleMuon
HLT_Mu23_TrkIsoVVL_Ele12_CaloIdL_TrackIdL_IsoVL_v*	1	MuonEG
HLT_Mu8_TrkIsoVVL_Ele23_CaloIdL_TrackIdL_IsoVL_DZ_v*	1	MuonEG
HLT_Mu12_TrkIsoVVL_Ele23_CaloIdL_TrackIdL_IsoVL_DZ_v*	1	MuonEG
HLT_DiMu9_Ele9_CaloIdL_TrackIdL_DZ_v*	1	MuonEG
HLT_Ele32_WPTight_Gsf_v*	1	SingleElectron
HLT_IsoMu24_v*	1	SingleMuon

Table 6: Trigger paths used in 2018 collision data.

79 **2.1.1 Trigger Efficiency**

80 The efficiency in data of the combination of triggers used in the analysis with respect to the
 81 offline reconstruction and selection is measured by considering 4ℓ events triggered by single
 82 lepton triggers. Details on the procedures are described in $H \rightarrow ZZ \rightarrow 4\ell$ ($\ell = e, \mu$) analyses
 83 common note [19].

84 A summary of the trigger efficiencies in MC truth, and in MC and data using the tag and probe
 85 method are summarized in table 7. The trigger efficiency in simulation is found to be $> 99\%$ in
 86 each final state.

Final State	$gg \rightarrow H$ MC	$gg \rightarrow H$ MC (matching)	Data (matching)
$4e$	$0.991^{+.002}_{-.002}$	$0.948^{+.004}_{-.004}$	$0.982^{+.005}_{-.007}$
4μ	$0.997^{+.001}_{-.001}$	$0.997^{+.001}_{-.001}$	$1.000^{+.000}_{-.001}$
$2e2\mu$	$0.995^{+.001}_{-.001}$	$0.964^{+.002}_{-.002}$	$0.983^{+.003}_{-.004}$

Table 7: Trigger efficiencies measured using 4ℓ events in 2018 data (TBU).

87 **2.2 Simulation samples and theoretical predictions**

88 **2.2.1 Signal Samples**

89 Descriptions of the SM Higgs boson production are obtained using the POWHEG V2 [20–22]
 90 generator for the five main production modes: gluon fusion ($gg \rightarrow H$) including quark mass
 91 effects [23], vector boson fusion (VBF) [24], and associated production (WH , ZH and $t\bar{t} H$ [25]).
 92 In the case of WH and ZH the MiNLO HVJ extension of POWHEG is used [26]. The description
 93 of the decay of the Higgs boson to four leptons is obtained using the JHUGEN generator [27]. In
 94 the case of WH , ZH and $t\bar{t} H$, the Higgs boson is allowed to decay to $H \rightarrow ZZ \rightarrow 2\ell^2X$ such that
 95 4-lepton events where two leptons originate from the decay of associated Z , W bosons or top
 96 quarks are also taken into account in the simulation. Showering of parton-level events is done
 97 using PYTHIA8.209, and in all cases matching is performed by allowing QCD emissions at all
 98 energies in the shower and vetoing them afterwards according to the POWHEG internal scale.
 99 All samples are generated with the NNPDF 3.1 NLO parton distribution functions (PDFs) [28].
 100 The list of signal samples and their cross sections are shown in Table 8. For each year, corre-
 101 sponding simulation samples are reweighted to match the pileup distribution in data for which
 102 details are described in [19].

103 **2.2.2 Background Samples**

104 Production of ZZ via quark-antiquark annihilation is generated at next-to-leading order (NLO)
 105 using POWHEG V2 [29] and PYTHIA8, with the same settings as for the Higgs signal. As this

Process	Dataset Name	$\sigma \times BR (\times \epsilon_{\text{filter}})$
$gg \rightarrow H(124) \rightarrow ZZ \rightarrow 4\ell$	/GluGluHToZZTo4L_M124_13TeV_powheg2_JHUGenV7011_pythia8/[1]	12.18 fb
$gg \rightarrow H(125) \rightarrow ZZ \rightarrow 4\ell$	/GluGluHToZZTo4L_M125_13TeV_powheg2_JHUGenV7011_pythia8/[1]	12.18 fb
$gg \rightarrow H(126) \rightarrow ZZ \rightarrow 4\ell$	/GluGluHToZZTo4L_M126_13TeV_powheg2_JHUGenV7011_pythia8/[1]	12.18 fb
$qq \rightarrow Hqq \rightarrow ZZqq \rightarrow 4\ell qq$	/VBF_HToZZTo4L_M125_13TeV_powheg2_JHUGenV709_pythia8/[1]	1.044 fb
$qq \rightarrow W^+H \rightarrow W^+ZZ \rightarrow 4\ell + X$	/WplusH_HToZZTo4L_M125_13TeV_powheg2-minlo-HWJ_JHUGenV7011_pythia8/[1]	0.232 fb
$qq \rightarrow W^-H \rightarrow W^-ZZ \rightarrow 4\ell + X$	/WminusH_HToZZTo4L_M125_13TeV_powheg2-minlo-HWJ_JHUGenV7011_pythia8/[1]	0.147 fb
$q\bar{q} \rightarrow ZH \rightarrow ZZZ \rightarrow 4\ell + X$	/ZH_HToZZ_4LFilter_M125_13TeV_powheg2-minlo-HZJ_JHUGenV7011_pythia8/[1]	0.668 fb
$gg \rightarrow ttH \rightarrow ttZZ \rightarrow 4\ell + X$	/ttH_HToZZ_4LFilter_M125_13TeV_powheg_JHUGenV7011_pythia8/[1]	0.393 fb
$gg \rightarrow bbH \rightarrow bbZZ \rightarrow 4\ell + X$	/bbH_HToZZTo4L_M125_13TeV_JHUGenV7011_pythia8/[1]	0.135 fb
$q\bar{q}/qg \rightarrow tHq \rightarrow tqZZ \rightarrow 4\ell + X$	/tqH_HToZZTo4L_M125_13TeV_JHUGenV7011_pythia8/[1]	0.0213 fb

[1] HIG-RunII-Summer20UL18wmLHEGEN-000*

Table 8: Signal Monte Carlo samples and cross sections.

Process	Dataset Name	$\sigma \cdot BR$
$qq \rightarrow ZZ \rightarrow 4\ell$	/ZZTo4L_TuneCP5_13TeV_powheg_pythia8/	1.256 pb
$qq \rightarrow ZZ \rightarrow 4\ell$	/ZZTo4L_TuneCP5_13TeV-amcatnloFXFX-pythia8/	1.212 pb
$gg \rightarrow ZZ \rightarrow 4e$	/GluGluToContinToZZTo4e_13TeV_MCFM701/	0.00159 pb
$gg \rightarrow ZZ \rightarrow 4\mu$	/GluGluToContinToZZTo4mu_13TeV_MCFM701/	0.00159 pb
$gg \rightarrow ZZ \rightarrow 2e2\mu$	/GluGluToContinToZZTo2e2mu_13TeV_MCFM701/	0.00319 pb
$Z \rightarrow \ell\ell + \text{jets}$	/DYJetsToLL_M-50_TuneCUETP8M1_13TeV-amcatnloFXFX-pythia8/	6104 pb
$Z \rightarrow \ell\ell + \text{jets}$	/DYJetsToLL_M-10to50_TuneCUETP8M1_13TeV-amcatnloFXFX-pythia8/	18610 pb
$WZ \rightarrow 3\ell\nu$	/WZTo3LNu_TuneCUETP8M1_13TeV-powheg-pythia8/	4.430 pb
$t\bar{t}$	/TTJets_TuneCUETP8M1_13TeV-amcatnloFXFX-pythia8/	815.96 pb
$t\bar{t} \rightarrow 2\ell 2\nu 2b$	/TTTo2L2Nu_13TeV-powheg/	87.31 pb
ZZZ	/ZZZ_TuneCUETP8M1_13TeV-amcatnlo-pythia8/	0.01398 pb
WZZ	/WZZ_TuneCUETP8M1_13TeV-amcatnlo-pythia8/	0.05565 pb
WWZ	/WWZ_TuneCUETP8M1_13TeV-amcatnlo-pythia8/	0.1651 pb
$t\bar{t}+ZZ$	/TTZZ_TuneCUETP8M2T4_13TeV-madgraph-pythia8/	0.001572 pb
$t\bar{t}+WW$	/TTWW_TuneCUETP8M2T4_3TeV - madgraph - pythia8/	0.007883 pb
$t\bar{t}+Z$	/ttZJets_13TeV_madgraphMLM/	0.259 pb

Table 9: Background Monte Carlo samples and cross sections.

106 simulation covers a large range of ZZ invariant masses, dynamical QCD factorization and
 107 renormalization scales have been chosen, equal to m_{ZZ} .

108 The $gg \rightarrow ZZ$ process is simulated at leading order (LO) with MCFM [30, 31]. In order to match
 109 the $gg \rightarrow H \rightarrow ZZ$ transverse momentum spectra predicted by POWHEG at NLO, the showering
 110 for MCFM samples is performed with different PYTHIA8 settings, allowing only emissions up
 111 to the parton-level scale (“wimpy” shower).

112 Although not directly used to model data observations, additional MC samples of WZ , Drell-
 113 Yan+jets, $t\bar{t}$, and tribosons are generated using MADGRAPH5_AMCANTNLO [32] either inclu-
 114 sively or merging several jet multiplicities, as detailed in the table. Table 9 summarizes the MC
 115 simulation datasets used for this analysis.

116 3 Objects

117 This analysis follows the same object defintion as in [33] for each year. Detailed description
 118 on objection definitions and scale factors can be found in the corresponding analysis note [19].
 119 Since this analysis is based on Ultra Legacy (UL) full Run 2 data, most of the objects related
 120 ingredients will be reevaluated with respect to [19].

121 The reconstruction of the SM Higgs boson in the decay chain $H \rightarrow ZZ \rightarrow 4\ell$ requires very
 122 efficient lepton reconstruction and identification in order to be sensitive to a low mass Higgs,
 123 for which at least one of the leptons has a p_T within the range 5 - 15 GeV. In this kinematic
 124 region the need is for an optimal efficiency, while retaining the rate of misidentified leptons
 125 low enough. On the same time, to allow a precise measurement of the Higgs boson mass and
 126 together properties, which depend on the lepton kinematics, the analysis needs a precise mo-
 127 mentum measurement. For both reasons, the analysis will make use of high statistics sources
 128 of prompt leptons to measure efficiency, mis-identification rate, and energy scale/resolution.
 129 Muon Efficiency measuremens using UL dataset are described as follows:

130 3.1 Electrons

131 3.1.1 Electron Reconstruction and Identification

132 Referred to [19].

133 3.1.2 Electron Energy Calibrations

134 Referred to [19].

135 3.1.3 Electron Efficiency Measurements

136 Referred to [19].

137 3.2 Muons

138 3.2.1 Muon Reconstruction and Identification

139 Referred to [19].

140 3.2.2 Muon Energy Calibrations

141 Referred to [19].

142 3.2.3 Muon Efficiency Measurements

143 Muon efficiencies are measured with the Tag and Probe (T&P) method performed on $Z \rightarrow \mu\mu$
 144 and $J/\psi \rightarrow \mu\mu$ events in bins of p_T and η . More details on the methodology can be found
 145 in Ref. [34]. Measurements are extracted using 2016, 2017 and 2018 UL data. The Z sample
 146 is used to measure the muon reconstruction and identification efficiency at high p_T , and the
 147 efficiency of the isolation and impact parameter requirements at all p_T . The J/ψ sample is used
 148 to measure the reconstruction efficiency at low p_T , as it benefits from a better purity in that
 149 kinematic regime.

150 **Reconstruction and identification** Results for the muon reconstruction and identification
 151 efficiency for $p_T > 20$ GeV have been derived by the Muon POG. However, results for low p_T
 152 muons were derived using J/ψ events, with the same definitions of probe and passing probes.
 153 Events are selected using `HLT_Mu8_v*` or `HLT_Mu17_v*` or `HLT_Mu20_v*` triggers. The probe

154 in this measurement are tracks reconstructed in the inner tracker, and the passing probes are
 155 those that are also reconstructed as a global or tracker muon and passing the Muon POG Loose
 156 muon identification.

157 Details on the procedure can be found in Ref. [35]. The efficiency and scale factors used for low
 158 p_T muons are the ones derived using single muon ultra-legacy dataset.

159 The efficiency in data and simulation is shown in Fig. 1.

160 **Impact parameter requirements** The measurement is performed using Z events. Events
 161 are selected with `HLT_IsoMu20_v*` or `HLT_IsoMu22_v*` or `HLT_IsoMu22_eta2p1_v*` for
 162 2016, `HLT_IsoMu27_v*` for 2017 and `HLT_IsoMu24_v*` for 2018 measurements. For this mea-
 163 surement, the probe is a muon passing the POG Loose identification criteria, and it is consid-
 164 ered a passing probe if it satisfies the SIP3D, dxy , dz cuts of this analysis. The results are shown
 165 in Fig. 2.

166 **Isolation requirements** The isolation efficiency is measured using events from the Z decay
 167 for any p_T . The events are selected with the triggers as required for impact parameter require-
 168 ments measurements as explained in previous paragraph. To fit the FSR contribution in the
 169 low mass region, MC template convoluted with the Gaussian is used to better fit the dimuon
 170 invariant mass.

171 **Tracking** The efficiency to reconstruct a muon track in the inner detector can be measured
 172 using as probes tracks reconstructed in the muon system alone. However, since it comes out to
 173 be 100%, it is no more recommended by muon POG.

174 **Overall results** The product of all the data to simulation scale factors for muon tracking,
 175 reconstruction, identification, impact parameter and isolation requirements is shown in Fig. 3.
 176 The systematic effects on measurements are estimated by ¹:

- 177 1. Varying the analytical signal and background shape models used to fit the dimuon in-
 178 variant mass
- 179 2. Increasing and decreasing the number of bins in dimuon mass distribution
- 180 3. Increasing and decreasing the dimuon mass range
- 181 4. Relaxing and tightening a selection cut on tag muons

182 3.3 Photons for FSR recovery

183 Referred to [19].

184 3.4 Jets

185 Referred to [19].

¹For low p_T measurements of reconstruction and identification only first three systematic sources are used as recommended by muon POG

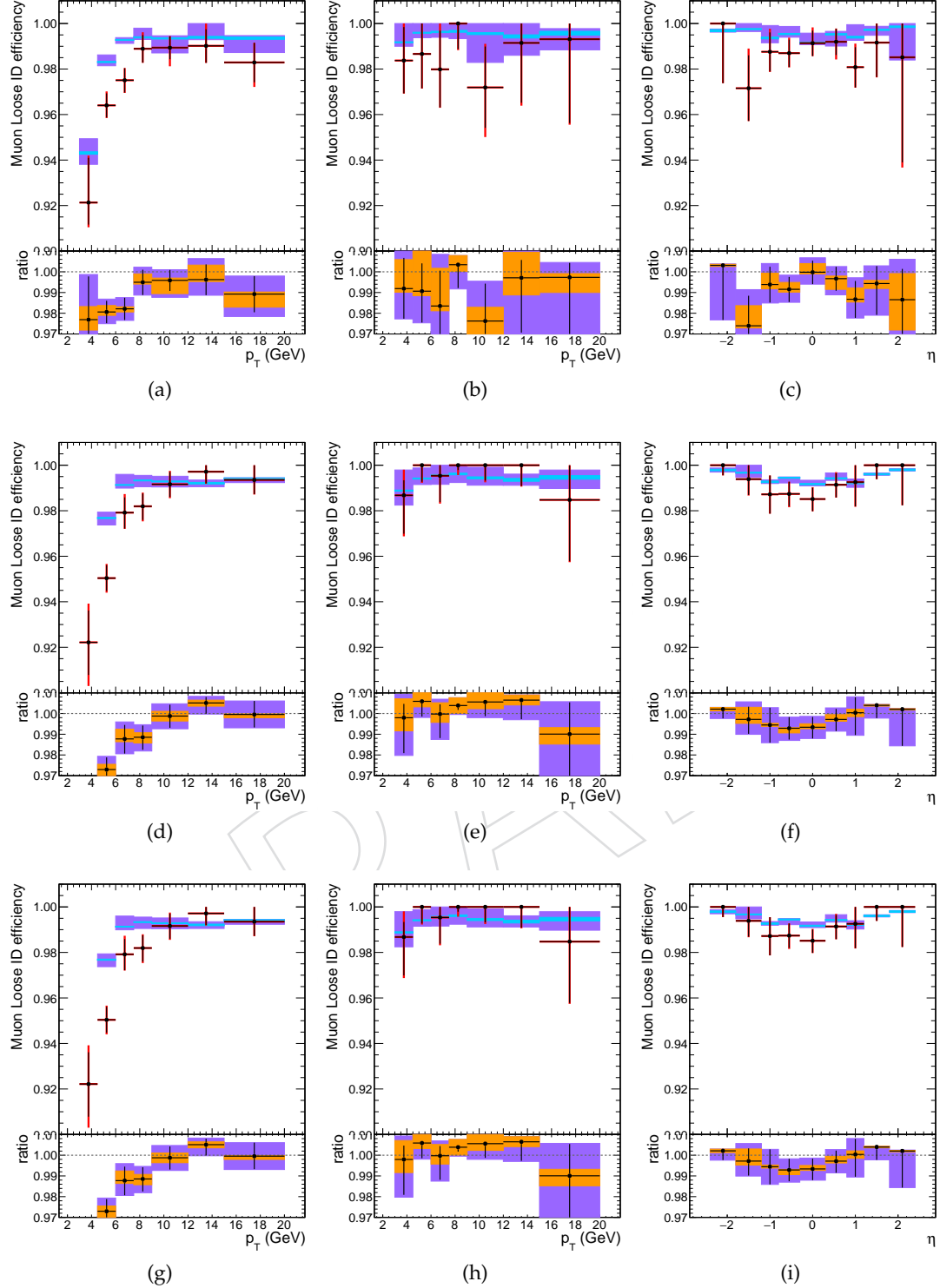


Figure 1: Muon reconstruction and identification efficiency at low p_T , measured with the tag&probe method on J/ψ events, as function of p_T in the barrel (left) and endcaps (center), and as function of η for $p_T > 7\text{ GeV}$ (right), for 2016 (top), 2017 (middle) and 2018 (bottom). In the upper panel, the larger error bars include also the systematical uncertainties, while the smaller ones are purely statistical. In the lower panel showing the ratio of the two efficiencies, the black error bars are for the statistical uncertainty, the orange rectangles for the systematical uncertainty and the violet rectangles include both uncertainties.

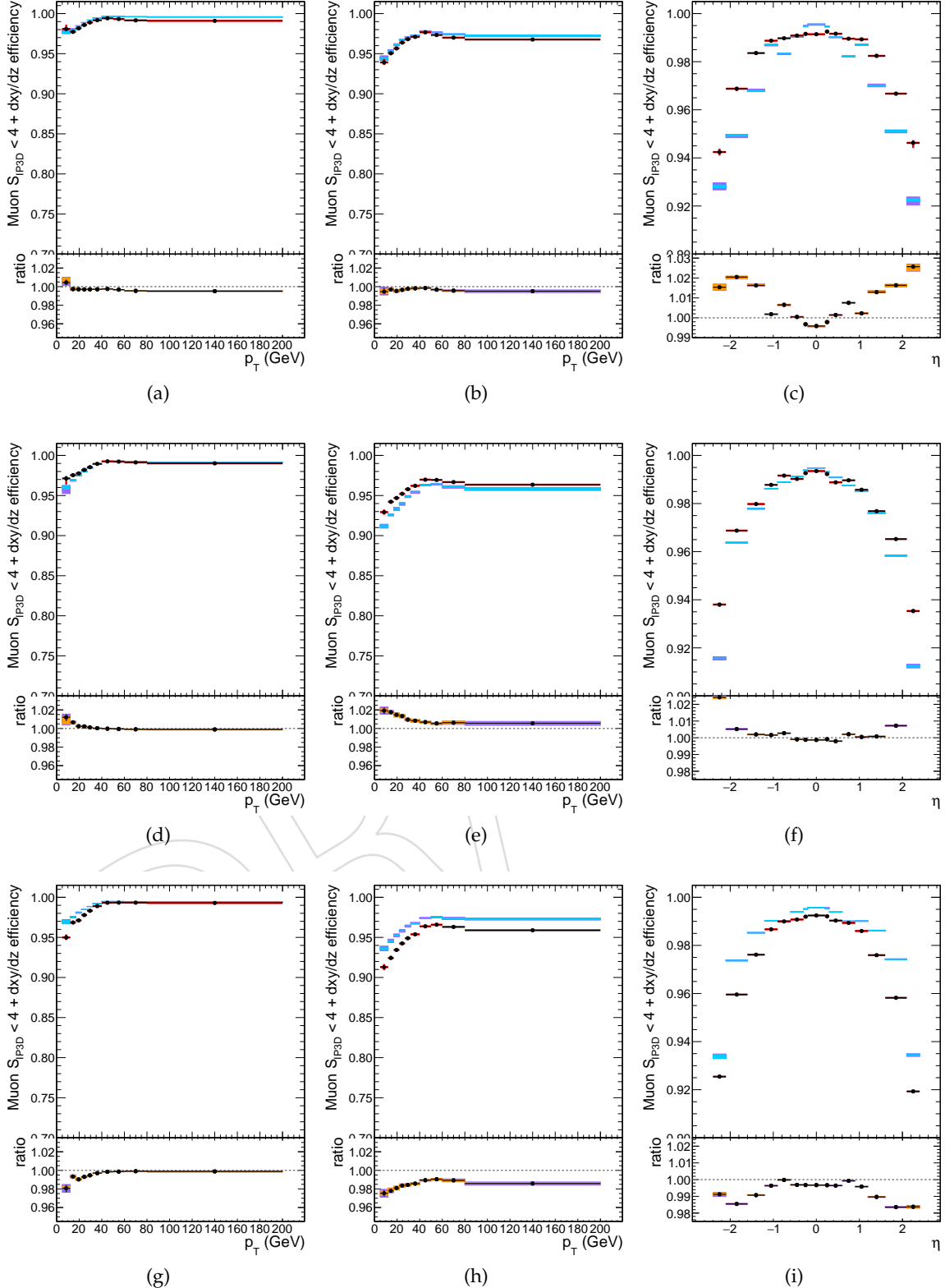


Figure 2: Efficiency of the muon impact parameter requirements, measured with the tag&probe method on Z events, as function of p_T in the barrel (left) and endcaps (center), and as function of η for $p_T > 20$ GeV (right), for 2016 (top), 2017 (middle) and 2018 (bottom). In the upper panel, the larger error bars include also the systematical uncertainties, while the smaller ones are purely statistical. In the lower panel showing the ratio of the two efficiencies, the black error bars are for the statistical uncertainty, the orange rectangles for the systematical uncertainty and the violet rectangles include both uncertainties.

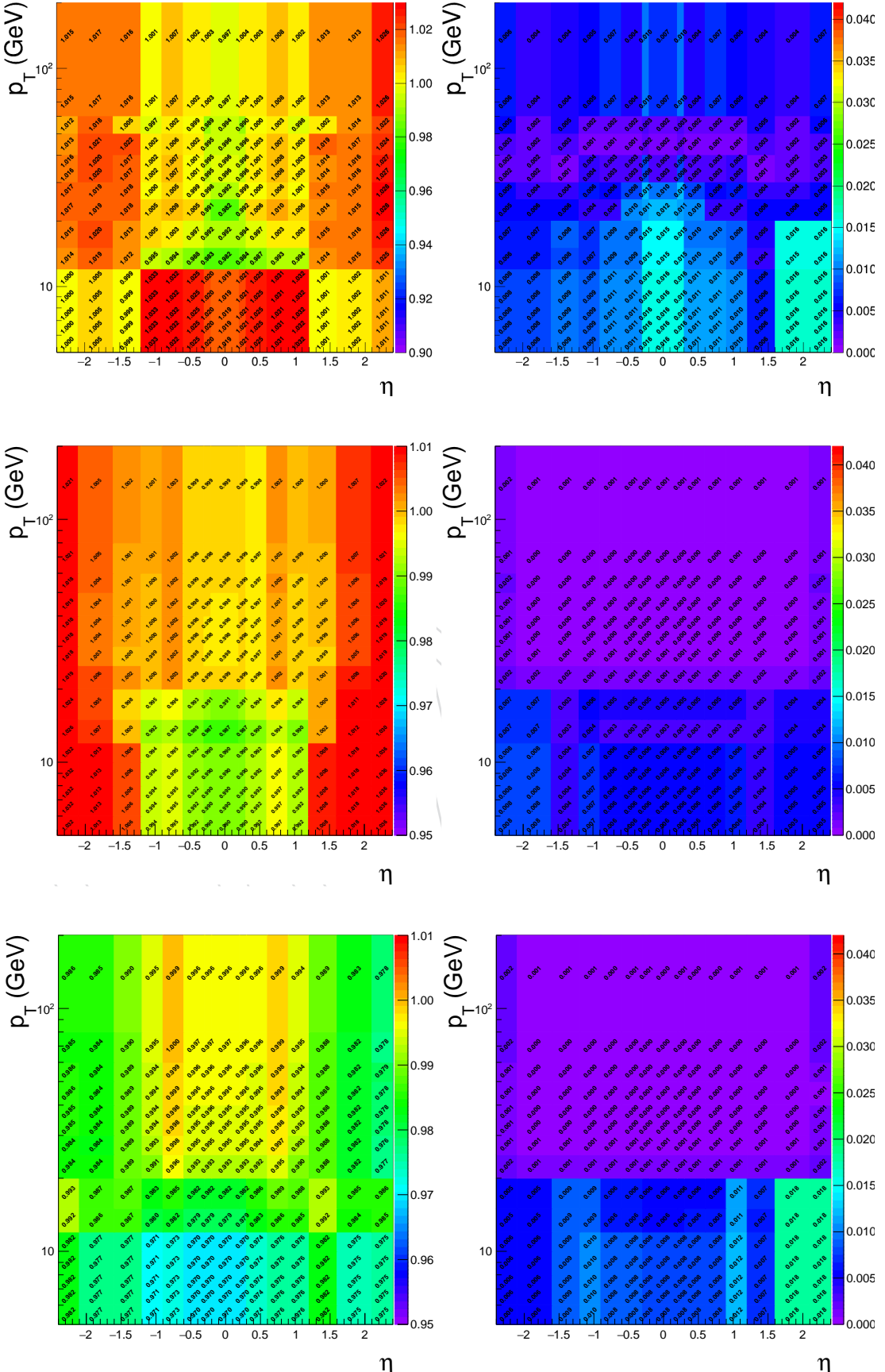


Figure 3: Left: Overall data to simulation scale factors for muons, as function of p_T and η . Right: Uncertainties on data to simulation scale factors for muons, as function of p_T and η . Results are shown for 2016 (top), 2017 (middle) and 2018 (bottom).

¹⁸⁶ **4 Signal Modelling**

¹⁸⁷ Referred to AN [19]

DRAFT

188 5 Background Estimation

189 Details on the background processes and their modeling is discussed in detail in AN [19]. In
 190 order to perform the differential measurements, the background four-lepton mass spectrum
 191 need to be extracted at the reconstruction level for each bin of the considered observable. In
 192 general, the background mass spectrum shape is not the same in every bin of the considered
 193 observable because the background does not have a resonance structure. The mass spectrum
 194 also can have non-negligible correlation with the observables.

195 In case of the irreducible backgrounds, the four-lepton mass spectra are extracted as the m_{4l}
 196 template shapes using Monte Carlo simulated events for each bin of the observable considered
 197 for the measurement. Similarly, in case of the reducible backgrounds the templates are built
 198 from the control regions in data.

In each differential bin of $p_T(4\ell)$ fractions of background events are presented in the Table 10.

Table 10: Estimated fraction of background events in each bin of $p_T(4\ell)$, for each final state using 2018 samples.

Background	final state	0 – 15	15 – 30	30 – 45	45 – 80	80 – 120	120 – 200	200 – 13000
qqZZ	2e2μ	0.483668	0.239196	0.130151	0.105276	0.0266332	0.011809	0.00326633
qqZZ	4e	0.459665	0.234399	0.136986	0.114916	0.0388128	0.00989346	0.00532725
qqZZ	4μ	0.492632	0.241203	0.110977	0.109173	0.0297744	0.0129323	0.00330827
ggZZ	2e2μ	0.310446	0.309859	0.191901	0.168134	0.0187793	0.000880282	0.0
ggZZ	4e	0.3085	0.306332	0.19247	0.17433	0.0169994	0.00136908	0.0
ggZZ	4μ	0.321332	0.319311	0.194863	0.150987	0.0128703	0.000638196	0.0
Z+X (CR)	4l	0.0992521	0.211153	0.209307	0.305327	0.120303	0.0483797	0.00627828

199

200 5.1 Estimation of ZZ normalization from Data

201 In earlier analyses, both the shape and the normalization for $q\bar{q} \rightarrow ZZ$ background were
 202 measured from simulation. However, with full Run 2 statistics, we can benefit from enough
 203 statistics to extend $m_{4\ell}$ range to fit ZZ normalization from data, still taking shapes from sim-
 204 ulation. This would help to improve the estimation and as well as reduction in uncertainties
 205 because luminosity and other theoretical uncertainties no longer contribute to the normaliza-
 206 tion. (studies in under validation)

207 6 Analysis Strategy

208 6.1 Event Selection

209 6.1.1 Trigger Selection

210 The events are required to have fired the High-Level Trigger paths described in subsection 2.1.
 211 Unlike in the Run I analysis, the trigger requirement does not depend on the selected final state:
 212 it is always the OR of all HLT paths. The reason is in Run II we will be targeting associated
 213 production modes that can come with additional leptons, thus improving trigger efficiency
 214 further.

215 6.1.2 Vertex Selection

216 The events are required to have at least one good primary vertex (PV) fulfilling the following
 217 criteria: high number of degree of freedom ($N_{PV} > 4$), collisions restricted along the z -axis
 218 ($z_{PV} < 24$ cm) and small radius of the PV ($r_{PV} < 2$ cm).

219 6.1.3 Z, ZZ and best ZZ Candidate Selection

220 The four-lepton candidates are built from what we call **selected leptons**, which are the tight
 221 leptons that pass the $SIP_{3D} < 4$ vertex constraint and the isolation cuts, where FSR photons
 222 are subtracted as described in [19]. A lepton cross cleaning is applied by discarding electrons
 223 which are within $\Delta R < 0.05$ of selected muons.

224 The construction and selection of four-lepton candidates proceeds according to the following
 225 sequence:

226 1. **Z candidates** are defined as pairs of selected leptons of opposite charge and matching
 227 flavour (e^+e^- , $\mu^+\mu^-$) that satisfy $12 < m_{\ell\ell(\gamma)} < 120$ GeV/ c^2 , where the Z candidate mass
 228 includes the selected FSR photons if any.

229 2. **ZZ candidates** are defined as pairs of non-overlapping Z candidates. The Z candidate
 230 with reconstructed mass $m_{\ell\ell}$ closest to the nominal Z boson mass is denoted as Z_1 , and
 231 the second one is denoted as Z_2 . ZZ candidates are required to satisfy the following list
 232 of requirements:

- 233 • **Ghost removal** : $\Delta R(\eta, \phi) > 0.02$ between each of the four leptons.
- 234 • **lepton p_T** : Two of the four selected leptons should pass $p_{T,i} > 20$ GeV/ c and
 $p_{T,j} > 10$ GeV/ c . FSR photons are used.
- 236 • **QCD suppression**: all four opposite-sign pairs that can be built with the four
 237 leptons (regardless of lepton flavor) must satisfy $m_{\ell\ell} > 4$ GeV/ c^2 . Here, se-
 238 lected FSR photons are not used in computing $m_{\ell\ell}$, since a QCD-induced low
 239 mass dilepton (eg. J/Ψ) may have photons nearby (e.g. from π_0).
- 240 • **Z_1 mass**: $m_{Z_1} > 40$ GeV/ c^2
- 241 • **'smart cut'**: defining Z_a and Z_b as the mass-sorted alternative pairing Z candi-
 242 dates (Z_a being the one closest to the nominal Z boson mass), require NOT($|m_{Z_a} -$
 $m_Z| < |m_{Z_1} - m_Z|$ AND $m_{Z_b} < 12$). Selected FSR photons are included in m_Z 's
 243 computations. This cut discards 4μ and $4e$ candidates where the alternative
 244 pairing looks like an on-shell Z + low-mass $\ell^+\ell^-$. (NB. In Run I, such a situa-
 245 tion was avoided by choosing the best ZZ candidate before applying kinematic
 246 cuts to it, most precisely before the $m_{Z_2} > 12$ GeV/ c^2 cut. The present smart
 247 cut allows to choose the best ZZ candidate after all kinematic cuts.)

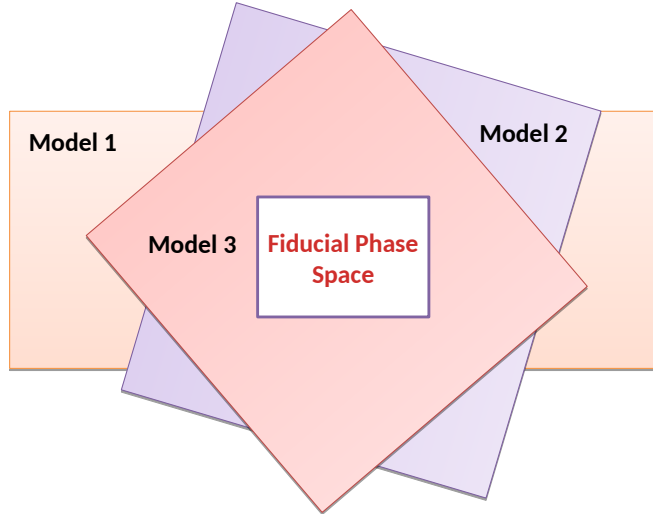
- 249 • **four-lepton invariant mass:** $m_{4\ell} > 70 \text{ GeV}/c^2$ (selected FSR photons are in-
250 cluded).

251 3. Events containing at least one selected ZZ candidate form the **signal region**.

252 4. **Best ZZ candidate selection:** If more than one ZZ candidates survive the above selection,
253 we choose the one with Z_1 closest in mass to nominal Z boson mass and Z_2 from the
254 candidates whose lepton give higher p_T sum.

255 6.2 Fiducial Volume Significance and Definition

256 To minimize the model dependence, results are extracted in the fiducial volume that closely
257 matches with the detector geometry as shown in Figure 4.



257 Figure 4: Fiducial phase definition among different models.

258 The differential cross subsections are measured in a fiducial region in order to reduce the ef-
259 fects of model dependent acceptances. The fiducial selection mimics the reconstruction level
260 selection, which is optimised to detect a low mass ($m_H 125\text{GeV}$) Higgs boson decaying to 4 lep-
261 tons through two Z bosons. Since in the standard model there are multiple production modes,
262 the fiducial selection and measurement strategy are designed to be independent of how the
263 Higgs boson is produced. For this reason, the inclusion of isolation in the fiducial selection
264 is necessary in order to make the reconstruction efficiency with respect to the fiducial volume
265 independent of the number of jets.

266 The fiducial volume is defined to match closely the reconstruction level selection and is very
267 similar to the definition used in Refs. [18]. With respect to the Run 1 analysis, the leptons are
268 defined as “dressed” leptons rather than Born level leptons. Leptons are dressed by adding the

269 four-momenta of leptons within $\Delta R < 0.3$ to the bare leptons. The fiducial lepton isolation cri-
 270 teria is also updated to match the Run 2 reconstruction level isolation. Leptons are considered
 271 isolated at generator level if the sum pt of particles within a cone $\Delta R < 0.3$ is less than 0.35. The
 272 fiducial volume definition can be seen in Table 11. The fiducial volume acceptance for various
 273 SM production modes can be seen in Table 15.

Table 11: Summary of requirements and selections used in the definition of the fiducial phase space for the $H \rightarrow 4\ell$ cross subsection measurements.

Requirements for the $H \rightarrow 4\ell$ fiducial phase space	
Lepton kinematics and isolation	
leading lepton p_T	$p_T > 20 \text{ GeV}$
next-to-leading lepton p_T	$p_T > 10 \text{ GeV}$
additional electrons (muons) p_T	$p_T > 7(5) \text{ GeV}$
pseudorapidity of electrons (muons)	$ \eta < 2.5(2.4)$
p_T sum of all stable particles within $\Delta R < 0.3$ from lepton	less than $0.35 \cdot p_T$
Event topology	
existence of at least two SFOS lepton pairs, where leptons satisfy criteria above	
inv. mass of the Z_1 candidate	$40 \text{ GeV} < m(Z_1) < 120 \text{ GeV}$
inv. mass of the Z_2 candidate	$12 \text{ GeV} < m(Z_2) < 120 \text{ GeV}$
distance between selected four leptons	$\Delta R(\ell_i \ell_j) > 0.02$ for any $i \neq j$
inv. mass of any opposite sign lepton pair	$m(\ell^+ \ell^-) > 4 \text{ GeV}$
inv. mass of the selected four leptons	$105 \text{ GeV} < m_{4\ell} < 140 \text{ GeV}$
the selected four leptons must originate from the $H \rightarrow 4\ell$ decay	

274 6.3 Unfolding

275 The effects of imperfect detector resolution can in general have an non-negligible impact on
 276 the shape of the distribution of the measured observables. For this reason, in case of the dif-
 277 ferential cross sections measurements, a procedure to correct for the detection efficiencies and
 278 resolution effects is applied. Throughout this document, this procedure will be referred to as
 279 the unfolding procedure, and the unfolded differential distributions will be referred to as dis-
 280 tributions at the fiducial level. Currently adopted procedure is “bin-by-bin unfolding”. This
 281 procedure for the unfolding of the detector effects from the observed distributions is the same
 282 as in Refs. [18] and [36]. The finite efficiencies and resolution effects are encoded in a detec-
 283 tor response matrix which describes how events migrate from a given observable bin at the
 284 fiducial level to a given bin at the reconstruction level. This matrix is diagonally dominant,
 285 with sizeable off-diagonal elements for observables involving jets. It is aimed we would also
 286 perform matrix inversion method as a validation tool for preceding method.

287 Examples of the efficiency matrices for gluon fusion and VBF production can be seen in Fig. 5.
 288 The matrices for the p_{TH} and $N(\text{jets})$ observables are shown.

289 6.4 Acceptance and other correction factors

290 In this section the acceptance and other correction factors while measuring the cross sections
 291 are discussed in details.

292 6.4.1 Acceptance

293 Ratio of the total number of events passing the fiducial level selectons $N_{fid.}$ to the total number
 294 of the generated events $N_{gen.}$ are is called acceptance as given in Equation 1.

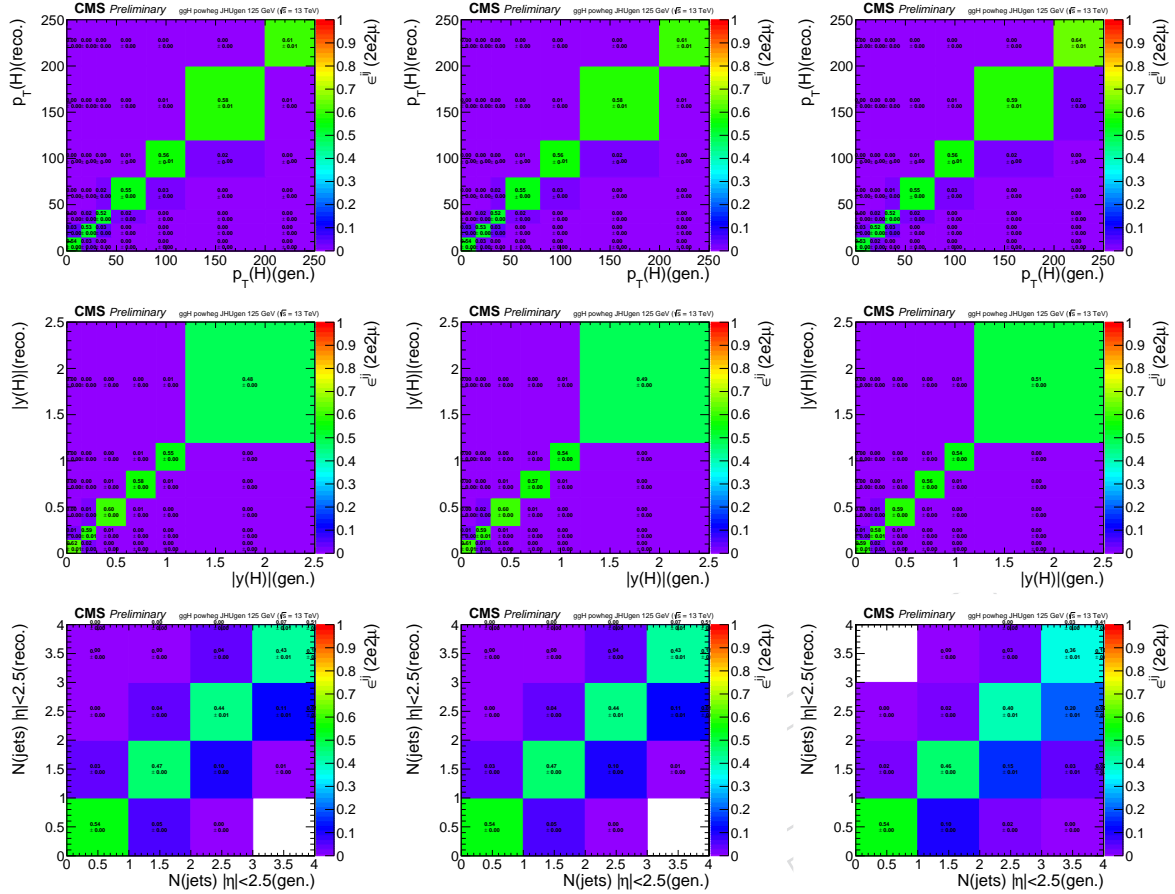


Figure 5: Efficiency matrices for the $p_T(H)$ (top) and $y(H)$ (middle) and $N(\text{jets})$ (bottom) observables for gluon fusion production modes in the $2e2\mu$ final state in 2016 (left) 2017 (middle) and 2018 (right) (TBU).

$$A = \frac{N_{fid.}}{N_{gen.}} \quad (1)$$

295 6.4.2 Other correction factors

296 Measurement strategy and definition of the fiducial volume is optimized to:

- 297 • detect a low mass Higgs ($m_H=125.38$ GeV) boson decaying to 4 leptons through a
298 pair of Z bosons
- 299 • keep the measurements independent of how the Higgs boson is produced.

300 For reconstruction efficiency to be independent of fiducial phase space, it is necessary to include
301 isolation in the definition of fiducial phase space.

302 In case of associated production of Higgs with vector bosons where the bosons can decay lep-
303 tonically, there is possibility that Higgs is reconstructed from wrong combination of leptons.
304 This makes it necessary to consider such “wrong combination” events as a background in or-
305 der to keep complete information from unbinned simultaneous fit of signal and background
306 parameterizations to four-lepton invariant mass.

307 Also, signal events which pass the fiducial level selections but fail the reconstruction are ac-
308 counted in the fiducial efficiency (ϵ) and the events which pass the reconstruction but fail the

309 fiducial selections are referred to as “nonfiducial signal” events (f_{nonfid}) and are treated as a
 310 background as illustrated in Figure 6.

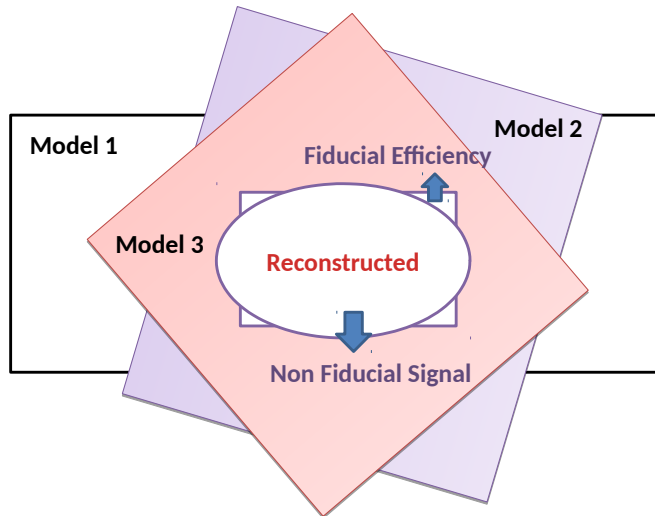


Figure 6: Fiducial efficiency(ϵ) and nonfiducial(f_{nonfid}) signal definition.

311 The summary of acceptance and other factors for full Run 2 periods are given Table. 15.

Table 12: Summary of different Standard Model signal models (2016).

Signal process	\mathcal{A}_{fid}	ϵ	f_{nonfid}	$(1 + f_{nonfid})\epsilon$
Individual Higgs boson production modes				
gg \rightarrow H (POWHEG) 125 GeV	0.397 ± 0.001	0.604 ± 0.001	0.051 ± 0.001	0.635 ± 0.001
VBF 125 GeV	0.446 ± 0.001	0.618 ± 0.002	0.039 ± 0.001	0.642 ± 0.002
WH 125 GeV	0.328 ± 0.001	0.593 ± 0.002	0.077 ± 0.001	0.638 ± 0.002
ZH 125 GeV	0.340 ± 0.002	0.608 ± 0.003	0.077 ± 0.002	0.655 ± 0.004
ttH 125 GeV	0.312 ± 0.002	0.585 ± 0.003	0.169 ± 0.004	0.684 ± 0.004

Table 13: Summary of different Standard Model signal models (2017).

Signal process	\mathcal{A}_{fid}	ϵ	f_{nonfid}	$(1 + f_{nonfid})\epsilon$
Individual Higgs boson production modes				
gg \rightarrow H (POWHEG) 125 GeV	0.403 ± 0.001	0.593 ± 0.001	0.056 ± 0.001	0.626 ± 0.001
VBF 125 GeV	0.445 ± 0.001	0.609 ± 0.001	0.044 ± 0.001	0.636 ± 0.001
WH 125 GeV	0.329 ± 0.001	0.583 ± 0.002	0.081 ± 0.001	0.631 ± 0.002
ZH 125 GeV	0.341 ± 0.002	0.594 ± 0.003	0.084 ± 0.002	0.644 ± 0.004
ttH 125 GeV	0.318 ± 0.003	0.589 ± 0.006	0.187 ± 0.007	0.699 ± 0.008

Table 14: Summary of different Standard Model signal models (2018).

Signal process	\mathcal{A}_{fid}	ϵ	f_{nonfid}	$(1 + f_{\text{nonfid}})\epsilon$
Individual Higgs boson production modes				
gg \rightarrow H (POWHEG) 125 GeV	0.403 ± 0.001	0.599 ± 0.001	0.055 ± 0.001	0.632 ± 0.001
VBF 125 GeV	0.443 ± 0.001	0.617 ± 0.002	0.043 ± 0.001	0.644 ± 0.002
WH 125 GeV	0.330 ± 0.001	0.625 ± 0.002	0.075 ± 0.001	0.672 ± 0.002
ZH 125 GeV	0.339 ± 0.002	0.629 ± 0.003	0.083 ± 0.002	0.681 ± 0.004
t \bar{t} H 125 GeV	0.314 ± 0.002	0.589 ± 0.003	0.184 ± 0.004	0.698 ± 0.004

Table 15: Summary of different Standard Model signal models.(Full Run 2)

Signal process	\mathcal{A}_{fid}	ϵ	f_{nonfid}	$(1 + f_{\text{nonfid}})\epsilon$
Individual Higgs boson production modes				
gg \rightarrow H (POWHEG) 125 GeV	0.402 ± 0.001	0.598 ± 0.002	0.054 ± 0.001	0.631 ± 0.002
VBF 125 GeV	0.445 ± 0.002	0.615 ± 0.002	0.043 ± 0.001	0.641 ± 0.003
WH 125 GeV	0.329 ± 0.002	0.604 ± 0.003	0.078 ± 0.002	0.651 ± 0.004
ZH 125 GeV	0.340 ± 0.003	0.613 ± 0.005	0.082 ± 0.004	0.663 ± 0.006
t \bar{t} H 125 GeV	0.315 ± 0.004	0.588 ± 0.007	0.181 ± 0.009	0.694 ± 0.010

6.5 Statistical Procedure

We measure differential fiducial cross subsection for $pp \rightarrow H \rightarrow 4\ell$ by performing a maximum likelihood fit of the signal and background parameterisations to the observed 4ℓ mass distribution, $N_{\text{obs}}(m_{4\ell})$, and the fiducial cross subsection (σ_{fid}) is directly extracted from the fit. The systematic uncertainties are included in the form of nuisance parameters and are effectively integrated out in the fit procedure. The results are obtained using an asymptotic approach [37] with a test statistic based on the profile likelihood ratio [38]. Following the models for signal and background contributions described above, the number of expected events in each final state f and in each bin i of a considered observable is expressed as a function of $m_{4\ell}$ given by:

$$\begin{aligned} N_{\text{obs}}^{f,i}(m_{4\ell}) &= N_{\text{fid}}^{f,i}(m_{4\ell}) + N_{\text{nonfid}}^{f,i}(m_{4\ell}) + N_{\text{nonres}}^{f,i}(m_{4\ell}) + N_{\text{bkg}}^{f,i}(m_{4\ell}) \\ &= \epsilon_{i,j}^f \cdot \left(1 + f_{\text{nonfid}}^{f,i}\right) \cdot \sigma_{\text{fid}}^{f,j} \cdot \mathcal{L} \cdot \mathcal{P}_{\text{res}}(m_{4\ell}) \\ &\quad + N_{\text{nonres}}^{f,i} \cdot \mathcal{P}_{\text{nonres}}(m_{4\ell}) + N_{\text{bkg}}^{f,i} \cdot \mathcal{P}_{\text{bkg}}(m_{4\ell}), \end{aligned} \quad (2)$$

The parameter $\sigma_{\text{fid}}^{f,j}$ is the signal cross subsection in bin j of the fiducial phase space, and it is the parameter extracted from the measurement.

The shape of the resonant signal contribution, $\mathcal{P}_{\text{res}}(m_{4\ell})$, is described by a double-sided Crystal Ball function, as described in previous sections, whose normalisation is proportional to the fiducial cross subsection. The shape of the non-resonant signal contribution, $\mathcal{P}_{\text{nonres}}(m_{4\ell})$, which arises from WH, ZH, and t \bar{t} H production where one of the leptons from the Higgs boson decay is lost or not selected, is empirically modelled by a Landau distribution whose shape parameters are constrained in the fit to be within a range determined from simulation. This contribution is treated as a background and hereafter we will refer to this contribution as the “non-resonant signal” contribution.

The $\epsilon_{i,j}^f$ represents the detector response matrix that maps the number of expected events in a given observable bin j at the fiducial level to the number of expected events in the bin i at the reconstruction level. The $f_{\text{nonfid}}^{i,j}$ fraction describes the ratio of the non-fiducial and fiducial

334 signal contribution in bin i at the reconstruction level. The efficiency is measured using signal
 335 simulation samples and corrected for residual differences between data and simulation. In the
 336 case of the integrated fiducial cross subsection measurement the efficiencies reduce to a single
 337 values.

338 An additional resonant contribution arises from events which are reconstructed but which do
 339 not originate from the fiducial phase space. These events are due to detector effects which
 340 cause differences between the quantities used for the fiducial phase space definition and the
 341 analogous quantities at the reconstruction level. This contribution is treated as background
 342 and is referred to as the “non-fiducial signal” contribution. The shape of these events is verified
 343 using simulation to be identical to the shape of the fiducial signal and its normalisation is fixed
 344 to be a fraction of the fiducial signal component. The value of this fraction, which we denote
 345 by f_{nonfid} , which has been determined from simulation for each of the studied signal models.

346 The variation between different models of the factor in the final column of Table 15, $(1 + f_{\text{nonfid}})\epsilon$, is directly related to the model dependence of the measurement. The model depen-
 347 dence is defined as the variation of the factor $(1 + f_{\text{nonfid}})\epsilon$ when the relative fraction of each
 348 the production modes are varied within their experimental constraints.

350 6.6 Extraction of differential $H \rightarrow 4\ell$ cross section

351 6.6.1 Considered observables

352 The differential fiducial cross sections are presented as a function of several kinematic observ-
 353 ables which are sensitive to the Higgs-boson production mechanisms. Examples are rapidity
 354 and transverse momentum of the four-lepton system, associated jet multiplicity and transverse
 355 momentum of the leading jet $p_T(H)$ or $p_T(4\ell)$, $|y(H)|$ or $|y(4\ell)|$, $N(\text{jets})$, and $p_T(\text{jet})$. These
 356 measurements are important to test the Standard Model predictions in the Higgs sector and
 357 can be used to constrain phase spaces of many theories beyond the Standard Model. In addi-
 358 tion, several other observables related to decay of Higgs boson are also studied. These include
 359 m_{Z_1} , m_{Z_2} , ϕ , $\cos\theta^*$ and several other observables which are sensitive to spin and CP or Higgs
 360 bosons.

361 6.6.2 Choice of bin boundaries

362 For each kinematic or differential observable, selection procedure of the binning boundaries
 363 has been optimized in order to have a similar expected measured cross-section for every bin.
 364 Relative uncertainties for p_T of Higgs observables are given in Table. 16.

365 6.6.3 Applying the Statistical Procedure

366 The fiducial differential cross section is extracted in the bins of kinematic observables at the
 367 fiducial level following the procedure outlined in previous. For signal yields, mass spectrum
 368 of signal is built in each cell of the response matrix using a Double Crystal Ball (DCB) function,
 369 similar to what was done in Ref. [?]. In practice, the same parameters of the CB function are
 370 used in each cell and the systematic uncertainties assigned on the energy scale and resolution
 371 generally cover discrepancy of signal mass spectrum among each cell.

372 Examples of the fitted signal line shapes for differential bins of $p_T(H)$ from $gg \rightarrow H$ (POWHEG
 373 + JHUGEN 125 GeV 2018 sample) in the individual final states are shown in Figure 29, and
 374 examples of the efficiency matrices for $p_T(H)$ for the $2e2\mu$ final state are shown in Fig 8. Many
 375 more examples can be seen in Appendix A.

Table 16: Differential cross section results for the $p_T(H)$ observable.

Bin range (GeV)	$d\sigma_{fid}$ (fb)	Δ_{tot} (% fb)	Δ_{rel} (%)	δ_{stat} (% fb)	δ_{syst} (% fb)
CMS preliminary choice					
0 - 10	0.34	+0.11 −0.096	+33 −28	+0.1 −0.091	+0.048 −0.031
10 - 20	0.53	+0.13 −0.11	+25 −21	+0.12 −0.11	+0.056 −0.037
20 - 30	0.42	+0.11 −0.097	+27 −23	+0.1 −0.093	+0.044 −0.027
30 - 45	0.43	+0.11 −0.094	+25 −22	+0.1 −0.089	+0.044 −0.029
45 - 80	0.52	+0.11 −0.1	+22 −19	+0.1 −0.092	+0.05 −0.038
80 - 120	0.25	+0.073 −0.062	+29 −25	+0.069 −0.06	+0.024 −0.018
120 - 200	0.18	+0.057 −0.048	+31 −26	+0.055 −0.046	+0.016 −0.011
200 - 13000	0.082	+0.036 −0.028	+44 −34	+0.035 −0.028	+0.008 −0.004
Total bins = 8	$\sigma_{fid} = \sum d\sigma_{fid} = 2.8$ (fb)				

376 Figure 9 shows the four lepton mass distributions for an Asimov dataset generated using SM
 377 cross section values and efficiencies from the $gg \rightarrow H$ production mode from POWHEG+JHUGEN,
 378 and resulting fitted values of PDFs of signal and background for different bins of $p_T(H)$ (all fi-
 379 final states combined).

DRAFT

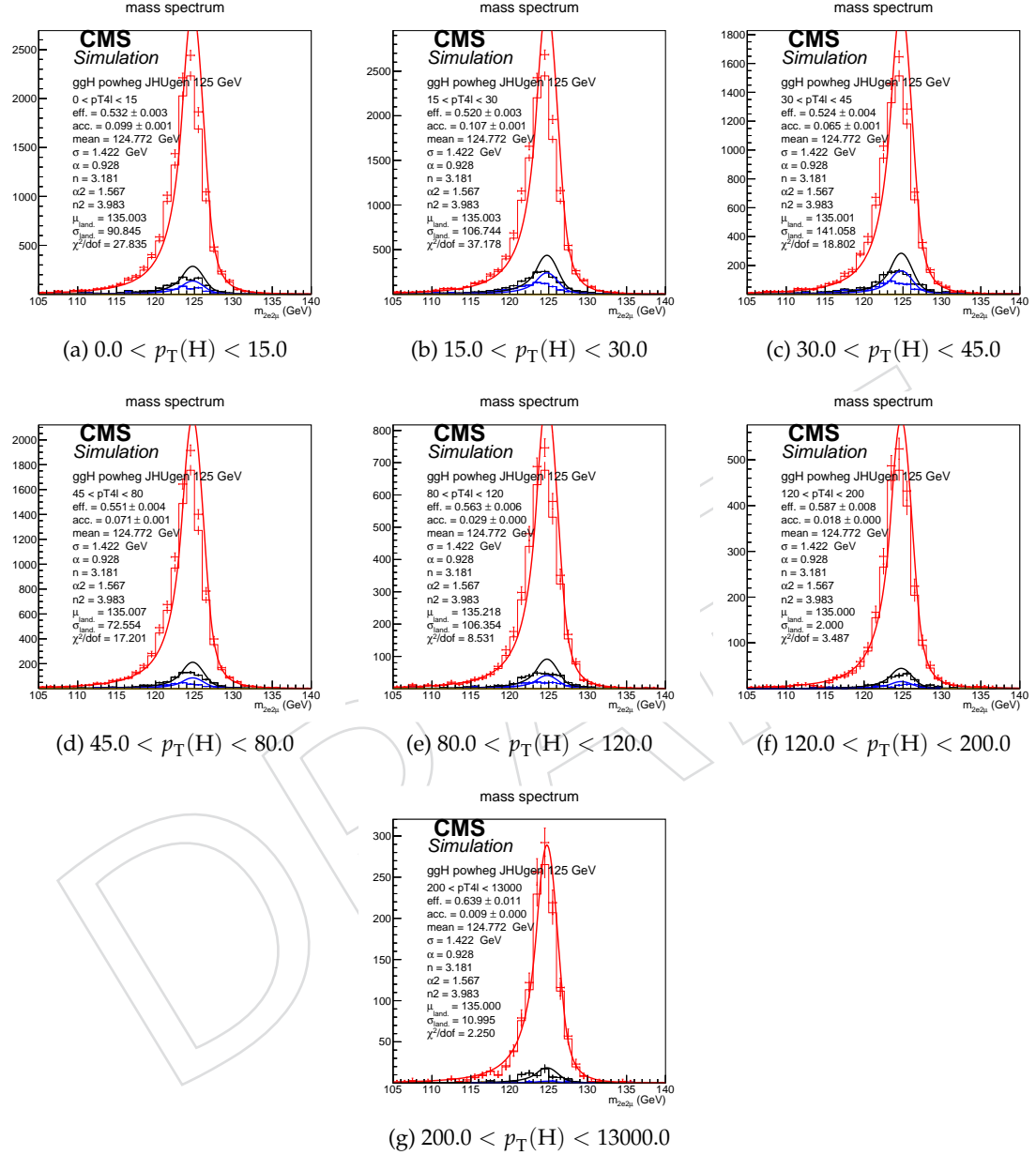


Figure 7: Example signal shapes at reconstruction level for a resonance of $m(4\ell)$ in $2e2\mu$ final state for the $gg \rightarrow H$ production mode from POWHEG+JHUGEN in different bins of $p_T(H)$. The black curve represents events which do not pass the fiducial volume selection. The curve has no effect on the result.

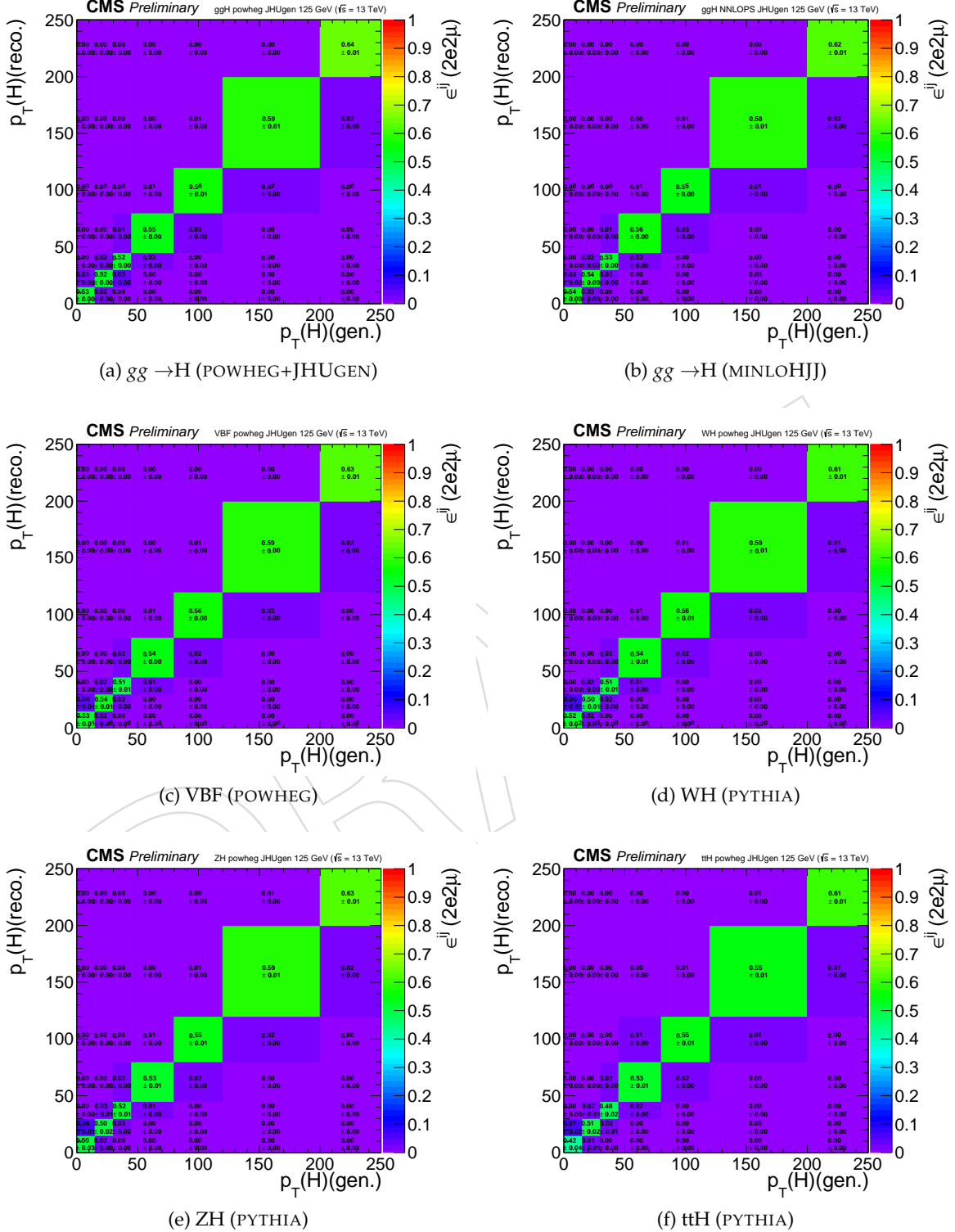


Figure 8: Efficiency response matrices for $p_T(H)$ for different SM production modes in the $2e2\mu$ final state using 2018 samples.

³⁸⁰ **6.7 Effective Field Theory interpretations for Differential measurements**

³⁸¹ To be updated

DRAFT

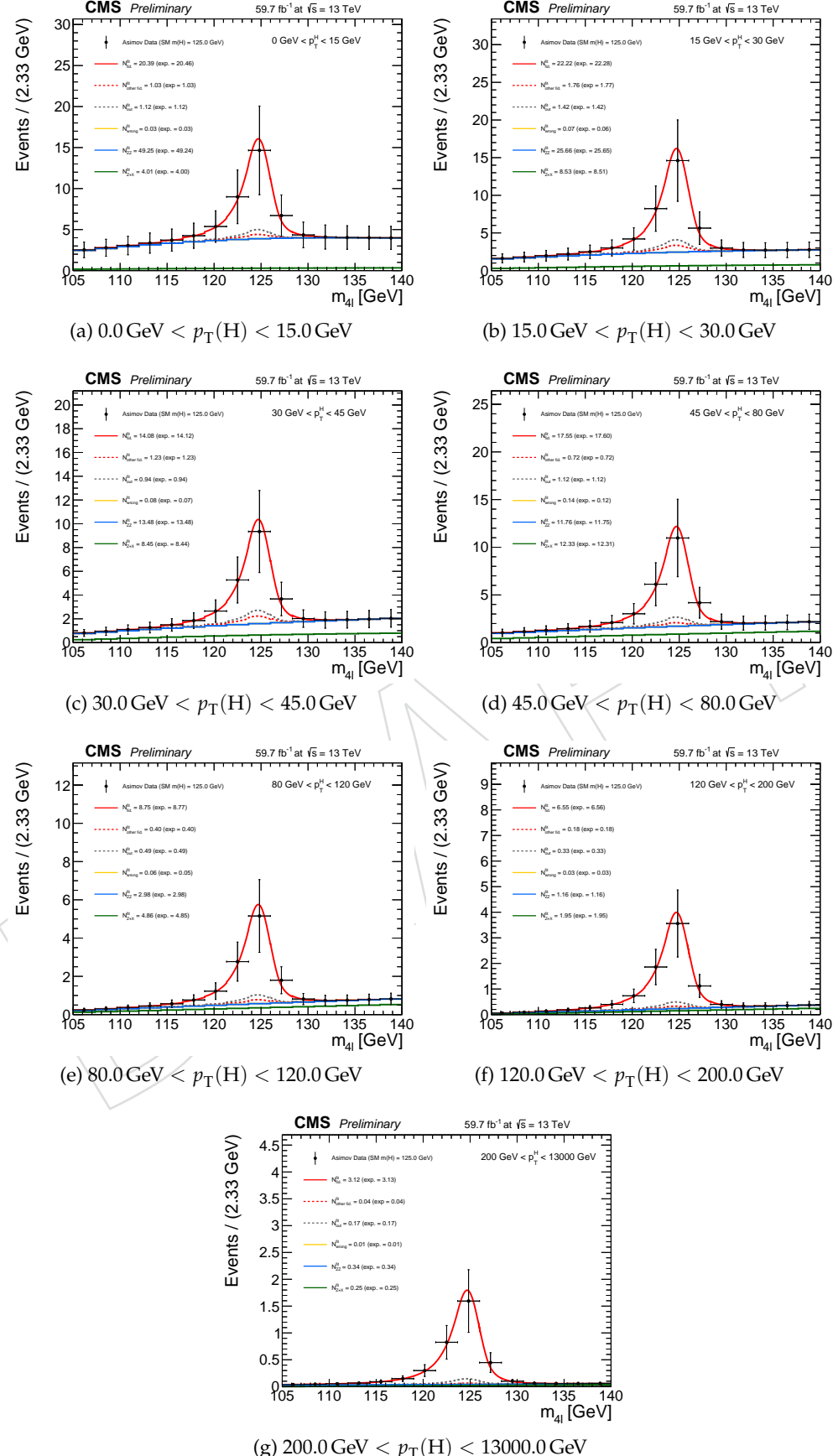


Figure 9: Four lepton mass distributions for an Asimov dataset generated using SM cross section values and SM efficiencies where the $gg \rightarrow H$ prediction is from POWHEG+JHUGEN and resulting fitted values of PDFs of signal and background for different bins of $p_T(\text{H})$ (all final states combined).

382 7 Systematic uncertainties

383 The main experimental uncertainties which affect both signal and background are the uncer-
 384 tainty on the integrated luminosity (from to 2.3% to 2.6%, depending on the data taking period)
 385 and the uncertainty on the lepton identification and reconstruction efficiency (ranging from 1
 386 to 2.5% and from 11 to 15.5% on the overall yields, in the 4μ and $4e$ channels, respectively).
 387 Experimental uncertainties for the reducible background estimation, described in Section ??,
 388 vary between 6% to 32% from the variation of the fake rates. The mismatch in the composition
 389 of backgrounds between the samples where the fake rate is derived and where it is applied
 390 accounts for about 30%.

391 The uncertainty of the lepton energy scale is assessed by propagating down to the four-leptons
 392 invariant mass the uncertainty associated the lepton momentum corrections on each individual
 393 lepton. The uncertainty is treated as uncorrelated (all up or all down). The new four-leptons
 394 invariant mass obtained this way is then fitted with only the mean value floating. The differ-
 395 ence between the new mean value and the default one gives an estimation of the impact of the
 396 lepton energy scale. The values are reported in the Table 17, together with the estimation of the
 397 impact of lepton momentum resolution, following a similar procedure.

Table 17: Difference (in %) between the nominal mean and width of the four-leptons Higgs mass distribution and those where the lepton momentum scale and resolution uncertainties have been propagated.

	4e	4μ	$2e2\mu$
Scale Difference (%)	0.087	0.049	0.069
Resolution Difference (%)	17	12	17

398 The results obtained this way suggest that the uncertainties from 2016 (20% on the resolution,
 399 0.3% for the $4e$ channel for scale) are still valid.

400 Theoretical uncertainties which affect both the signal and background estimation include un-
 401 certainties from the renormalization and factorization scale and choice of PDF set. The uncer-
 402 tainty from the renormalization and factorization scale is determined by varying these scales
 403 between 0.5 and 2 times their nominal value while keeping their ratio between 0.5 and 2. In the
 404 case of ggF production mode, the QCD scale uncertainty is broken down to 9 different sources.
 405 The renormalization and factorization scale affect the overall cross section, the migration of
 406 the stage1.1 bins in different Higgs pT and number of jets, top loop effects are treated as inde-
 407 pendent uncertainties, and correlated among different stage 1.1 bins. The numbers are shown
 408 in Fig ???. The uncertainty from the PDF set is determined by taking the root mean square of
 409 the variation when using different replicas of the default NNPDF set. PDF uncertainty arises
 410 from uncertainty is also taken into account. On the background, an additional uncertainty of
 411 10% on the K factor used for the $gg \rightarrow ZZ$ prediction is applied as described in Section ???. A
 412 systematic uncertainty of 2% on the branching ratio of $H \rightarrow ZZ \rightarrow 4\ell$ only affects the signal
 413 yield. In the case of event categorization, experimental and theoretical uncertainties which ac-
 414 count for possible migration of signal and background events between categories are included.
 415 The main sources of uncertainty on the event categorization include the QCD scale, PDF set,
 416 and the modeling of hadronization and the underlying event. These uncertainties amount to
 417 between 4–20% for the signal and 3–20% for the background depending on the category. The
 418 lower range corresponds to the VBF and VH processes and the upper range corresponds to the
 419 $gg \rightarrow H$ process yield in the VBF-2jet-tagged category. Additional uncertainties come from the
 420 imprecise knowledge of the jet energy scale (from 2% for the $gg \rightarrow H$ yield in the untagged
 421 category to 22% for $gg \rightarrow H$ yield in the VBF-2jet-tagged category) and b-tagging efficiency

⁴²² and mistag rate (up to 10% in the $t\bar{t}H$ -tagged category). In the cross section measurement, the
⁴²³ signal cross section uncertainties arise from theoretical sources are removed.

Table 18: Summary of the experimental systematic uncertainties in the $H \rightarrow 4\ell$ measurements of 2016, 2017 and 2018 data.

Summary of relative systematic uncertainties			
Common experimental uncertainties			
	2016	2017	2018
Luminosity	2.6 %	2.3 %	2.5 %
Lepton identification/reconstruction efficiencies	1.2 – 15.5 %	1.1 – 12 %	0.7 – 11 %
Background related uncertainties			
Reducible background ($Z+X$)	31 – 42 %	31 – 38 %	31 – 37 %
Signal related uncertainties			
Lepton energy scale	0.04 – 0.3 %	0 %	0 %
Lepton energy resolution	20 %	20 %	20 %

Table 19: Summary of the theory systematic uncertainties in the $H \rightarrow 4\ell$ measurements for the inclusive analysis

Summary of inclusive theory uncertainties	
QCD scale (gg)	± 3.9 %
PDF set (gg)	± 3.2 %
Bkg K factor (gg)	± 10 %
QCD scale (VBF)	+0.4/-0.3 %
PDF set (VBF)	± 2.1 %
QCD scale (WH)	+0.5/-0.7 %
PDF set (WH)	± 1.9 %
QCD scale (ZH)	+3.8/-3.1 %
PDF set (ZH)	± 1.6 %
QCD scale ($t\bar{t}H$)	+5.8/-9.2 %
PDF set ($t\bar{t}H$)	± 3.6 %
BR($H \rightarrow ZZ \rightarrow 4\ell$)	2 %
QCD scale ($q\bar{q} \rightarrow ZZ$)	+3.2/-4.2 % %
PDF set ($q\bar{q} \rightarrow ZZ$)	+3.1/-3.4 %
Electroweak corrections ($q\bar{q} \rightarrow ZZ$)	± 0.1 %

⁴²⁴ 7.1 Systematic uncertainties treatment when combining the data sets

⁴²⁵ In this Section we describe how different systematic uncertainties are treated when combining
⁴²⁶ the data sets. The theoretical uncertainties are correlated. All the experimental systematics are
⁴²⁷ treated independently.

⁴²⁸ In this subsection we summarize the status of the analysis after selection, showing the inputs to
⁴²⁹ the final results, namely the event yields and errors in the full signal region and in a restricted
⁴³⁰ $m_{4\ell}$ range, and the distributions of the main kinematic variables in data and MC.

⁴³¹ 7.1.1 Signal Region Yields

⁴³² The number of candidates observed in data and the expected yields for the backgrounds and
⁴³³ Higgs boson signal after the full event selection are reported in Table 21 for the full range of
⁴³⁴ $m_{4\ell}$. Table ?? shows the expected and observed yields for each of the 22 event categories, for a
⁴³⁵ $118 < m_{4\ell} < 130$ GeV mass window around the Higgs boson peak.

Table 20: The number of expected background and signal events and number observed candidates after full analysis selection, for each final state, for the full mass range $m_{4\ell} > 70$ GeV, for an integrated luminosity of 137 fb^{-1} . Signal and ZZ backgrounds are estimated from Monte Carlo simulation, Z+X is estimated from data.

Channel	4μ	$4e$	$2e2\mu$	$4l$
qqZZ	1414.85	748.64	1835.05	3998.54
ggZZ	268.48	163.45	399.78	831.70
ZX	112.84	48.62	151.71	313.18
EW bkg	15.13	12.73	27.83	55.69
Sum of backgrounds	1811.30	973.45	2414.36	5199.11
Signal ($m_H = 125$ GeV)	95.27	46.01	118.53	259.82
Total expected	1906.57	1019.46	2532.90	5458.93
Data	1970	1032	2646	5648

⁴³⁶ 7.1.2 Signal Region Distributions

⁴³⁷ The reconstructed four-lepton invariant mass distribution is shown in Figure 12 for the full
⁴³⁸ dataset, and compared to expectations from the SM backgrounds, first for the full mass range,
⁴³⁹ and then zooming on the low-mass range and high-mass range. In Figure 13, the same dis-
⁴⁴⁰ tributions are shown split by final state ($4e$, 4μ , and $2e2\mu$), for the two same mass ranges. In
⁴⁴¹ Figure ??, they are split by event category, for the low-mass range. The SM background dis-
⁴⁴² tributions are obtained combining the rate normalization from data-driven methods and knowl-
⁴⁴³ edge on shapes taken from the MC samples.

⁴⁴⁴

⁴⁴⁵ The reconstructed dilepton invariant masses selected as Z_1 and Z_2 are shown in Figures ??
⁴⁴⁶ together with their correlation, both full range of $m_{4\ell}$ and focusing on a $118 < m_{4\ell} < 130$ GeV
⁴⁴⁷ mass window around the Higgs boson peak.

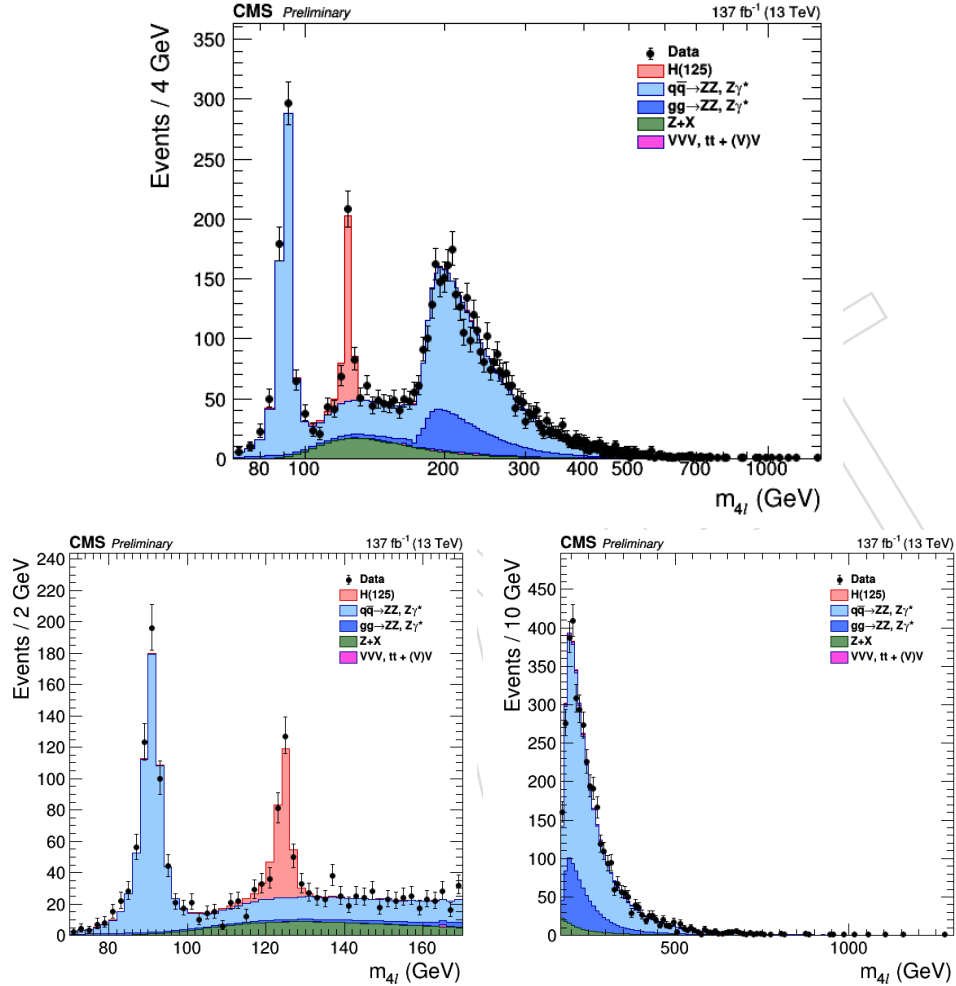


Figure 10: Distribution of the four-lepton reconstructed invariant mass m_{4l} in the full mass range (top) and the low-mass range (bottom left) and high-mass range (bottom right). Points with error bars represent the data and stacked histograms represent expected distributions. The 125 GeV Higgs boson signal and the ZZ backgrounds are normalized to the SM expectation, the $Z+X$ background to the estimation from data.

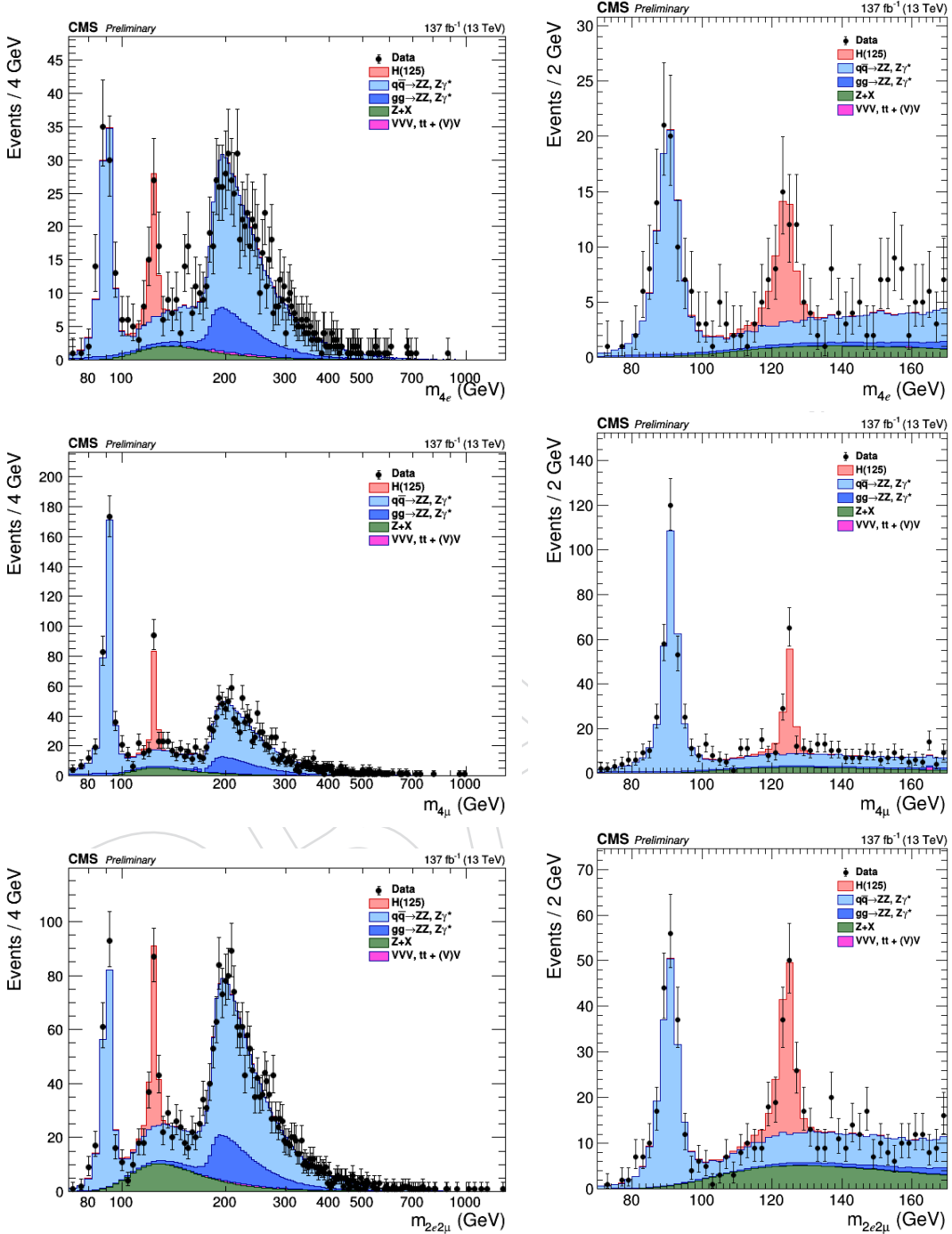
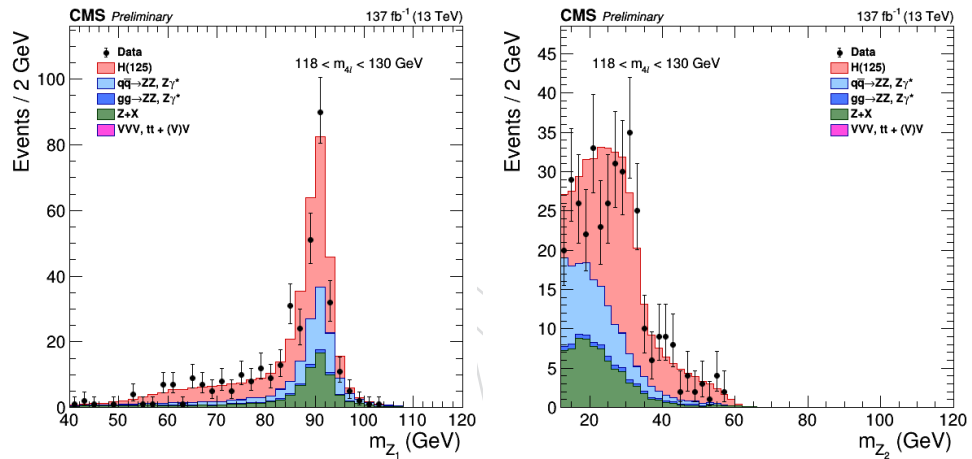


Figure 11: Distribution of the four-lepton reconstructed mass in several sub-channels: $4e$ (top), 4μ (middle), $2e2\mu$ for the low-mass range (bottom) for the full mass range (left) and the low-mass range (right).



Distribution of the Z_1 (left) and Z_2 (right) reconstructed invariant masses for the full mass range (left) and the low mass ($118 < m_{4\ell} < 130$ GeV) range (right). The stacked histograms and the gray scale represent expected distributions, and points represent the data. The 125 GeV Higgs boson signal and the ZZ backgrounds are normalized to the SM expectation, the Z+X background to the estimation from data.

448 8 Results

449 In this section, we describe the methods used for the estimation of the significance of the ex-
 450 cess of events above the SM backgrounds observed in the low-mass region, and of the signal
 451 strength, i.e. its cross section normalized to the one expected for a SM Higgs.

452 To exploit all the properties of the resonance under study or search, a multi-dimensional fit is
 453 implemented. For each of the categories defined in Section ??, the variable used in the maxi-
 454 mum likelihood fit is the four-lepton mass without kinematic refitting $m_{4\ell}$.

455 8.1 Yields and distributions

456 In this subsection we summarize the status of the analysis after selection, showing the inputs to
 457 the final results, namely the event yields and errors in the full signal region and in a restricted
 458 $m_{4\ell}$ range, and the distributions of the main kinematic variables in data and MC.

459 8.1.1 Signal Region Yields

460 The number of candidates observed in data and the expected yields for the backgrounds and
 461 Higgs boson signal after the full event selection are reported in Table 21 for the full range of
 462 $m_{4\ell}$. Table ?? shows the expected and observed yields for each of the 22 event categories, for a
 463 $118 < m_{4\ell} < 130$ GeV mass window around the Higgs boson peak.

Table 21: The number of expected background and signal events and number observed candi-
 dates after full analysis selection, for each final state, for the full mass range $m_{4\ell} > 70$ GeV, for
 an integrated luminosity of 137 fb^{-1} . Signal and ZZ backgrounds are estimated from Monte
 Carlo simulation, Z+X is estimated from data.

Channel	4μ	$4e$	$2e2\mu$	$4l$
qqZZ	1414.85	748.64	1835.05	3998.54
ggZZ	268.48	163.45	399.78	831.70
ZX	112.84	48.62	151.71	313.18
EW bkg	15.13	12.73	27.83	55.69
Sum of backgrounds	1811.30	973.45	2414.36	5199.11
Signal ($m_H = 125$ GeV)	95.27	46.01	118.53	259.82
Total expected	1906.57	1019.46	2532.90	5458.93
Data	1970	1032	2646	5648

464 8.1.2 Signal Region Distributions

465 The reconstructed four-lepton invariant mass distribution is shown in Figure 12 for the full
 466 dataset, and compared to expectations from the SM backgrounds, first for the full mass range,
 467 and then zooming on the low-mass range and high-mass range. In Figure 13, the same dis-
 468 tributions are shown split by final state ($4e$, 4μ , and $2e2\mu$), for the two same mass ranges. In
 469 Figure ??, they are split by event category, for the low-mass range. The SM background distri-
 470 butions are obtained combining the rate normalization from data-driven methods and knowl-
 471 edge on shapes taken from the MC samples.

472

473 The reconstructed dilepton invariant masses selected as Z_1 and Z_2 are shown in Figures ??
 474 together with their correlation, both full range of $m_{4\ell}$ and focusing on a $118 < m_{4\ell} < 130$ GeV
 475 mass window around the Higgs boson peak.

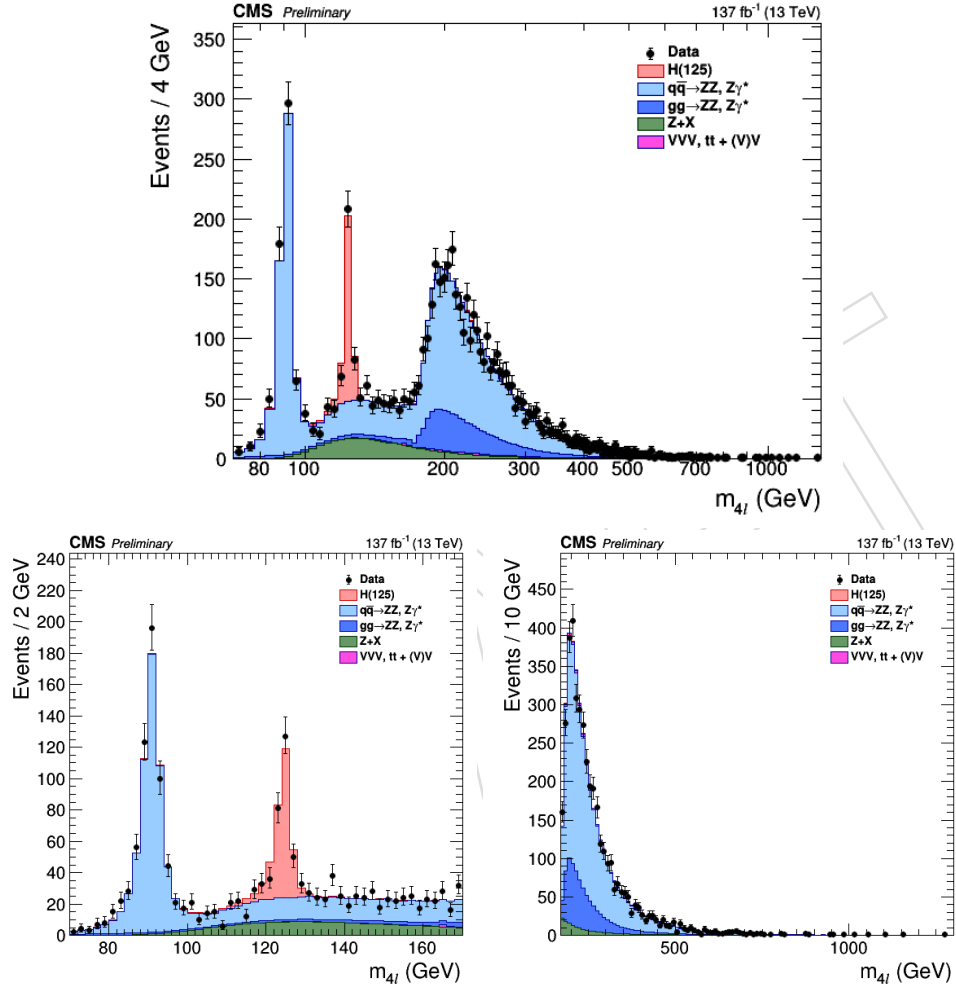


Figure 12: Distribution of the four-lepton reconstructed invariant mass $m_{4\ell}$ in the full mass range (top) and the low-mass range (bottom left) and high-mass range (bottom right). Points with error bars represent the data and stacked histograms represent expected distributions. The 125 GeV Higgs boson signal and the ZZ backgrounds are normalized to the SM expectation, the Z+X background to the estimation from data.

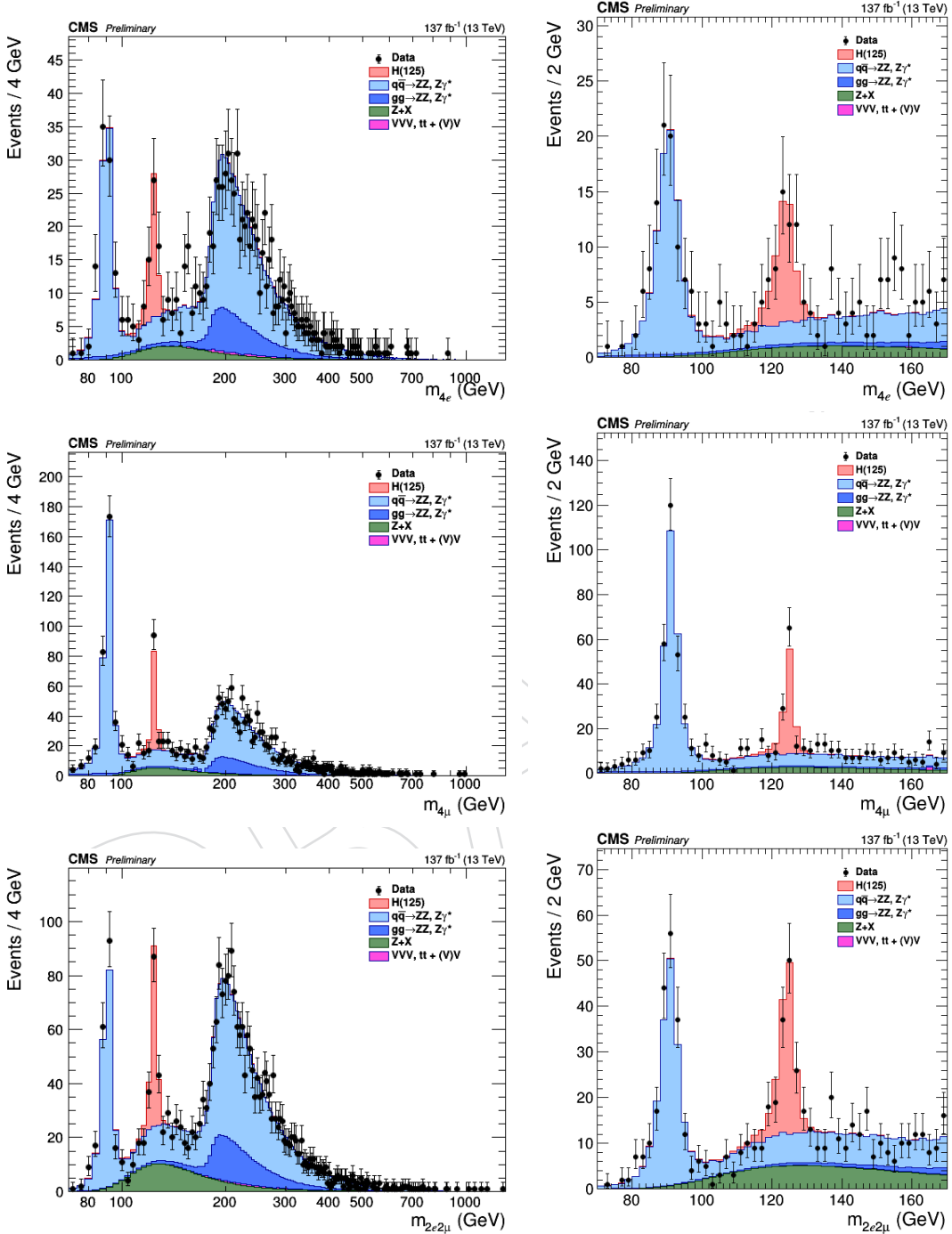
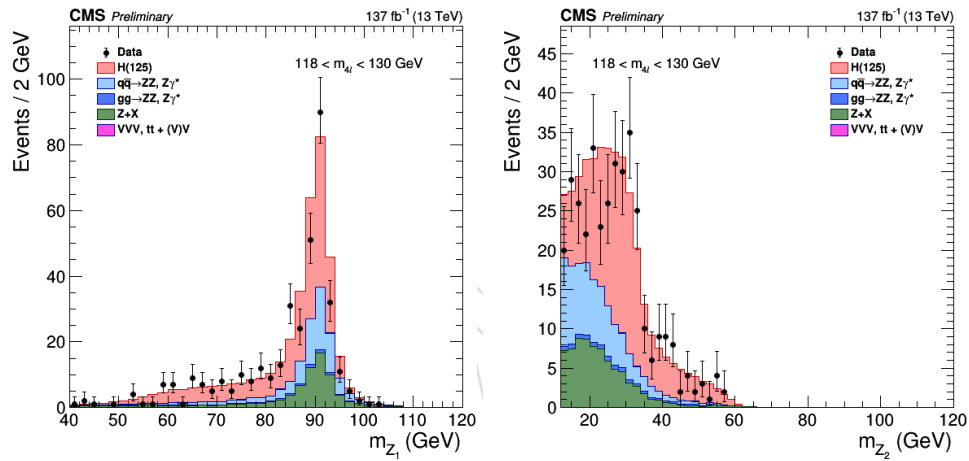


Figure 13: Distribution of the four-lepton reconstructed mass in several sub-channels: $4e$ (top), 4μ (middle), $2e2\mu$ for the low-mass range (bottom) for the full mass range (left) and the low-mass range (right).



Distribution of the Z_1 (left) and Z_2 (right) reconstructed invariant masses for the full mass range (left) and the low mass ($118 < m_{4\ell} < 130$ GeV) range (right). The stacked histograms and the gray scale represent expected distributions, and points represent the data. The 125 GeV Higgs boson signal and the ZZ backgrounds are normalized to the SM expectation, the Z+X background to the estimation from data.

476 8.2 Differential Cross Sections measurement results

477 **FIXME:** Results to be updated with final processing

478 8.2.1 Results for Higgs production observables

479 The expected differential cross section results can be seen in Fig. 14.

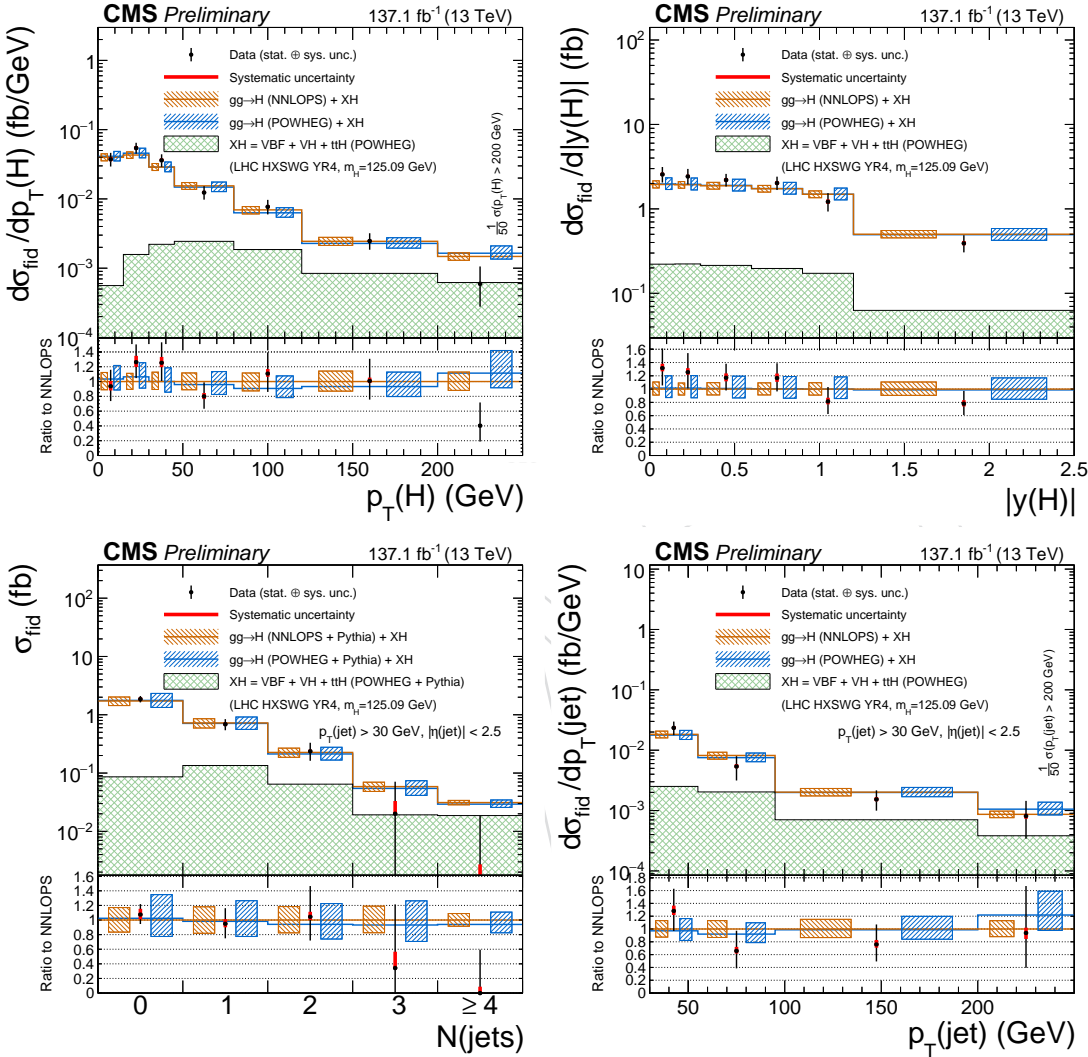


Figure 14: The results of the differential cross section measurement for $p_T(H)$ (middle left), $|y(H)|$ (middle right) and $N(\text{jets})$ (bottom left), p_T of the leading jet (bottom right). The acceptance and theoretical uncertainties in the differential bins are calculated using POWHEG. The sub-dominant component of the signal ($\text{VBF} + \text{VH} + \text{ttH}$) is denoted as XH .

480 8.2.2 Results for Higgs decay observables

481 Additional decay observables include Φ , Φ_1 , $m(Z_1)$, $m(Z_2)$, $|\cos\theta^*|$, $|\cos\theta_1|$ and $|\cos\theta_2|$ which
482 are studied in $H \rightarrow 4\ell$ using full Run 2 toy data and compared with the theoretical predictions.

483 In each plot shown below, systematic uncertainty is indicated by red bars and black bars show
484 total statistical and the systematic uncertainties, combined in quadrature. The blue and brown
485 colors show the theoretical predictions. The acceptances and the theoretical uncertainties in
486 differential bins are computed using POWHEG. Sub-dominant production contributions XH

⁴⁸⁷ = VBF + VH + ttH are shown in green separately. The systematic uncertainties correspond to
⁴⁸⁸ the generators accuracy are also taken in to account for differential predictions. The fraction of
⁴⁸⁹ 4 μ , 4e and 2e2 μ in each differential bin is allowed to float in fit.

DRAFT

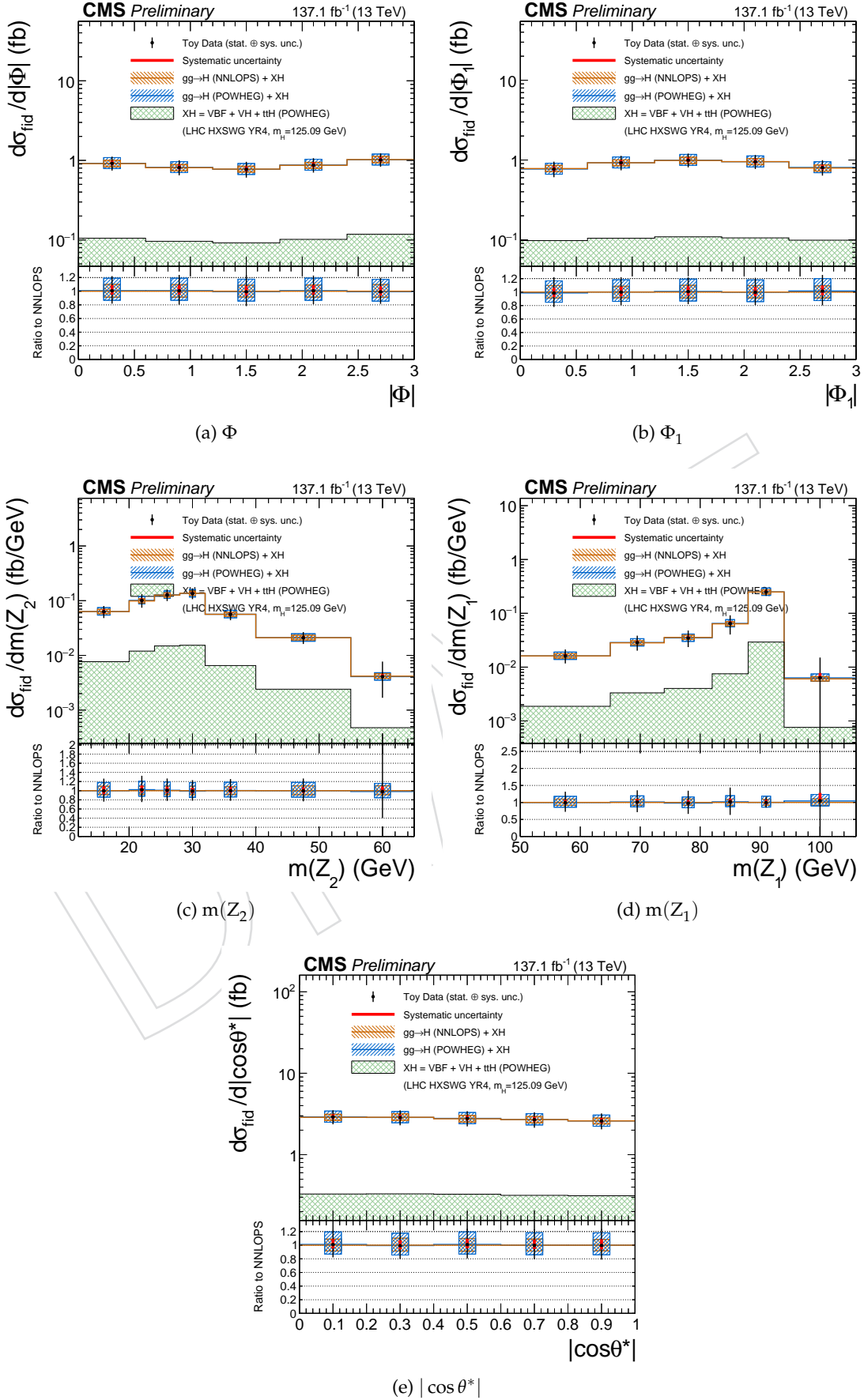


Figure 15: Differential fiducial cross section results using full Run 2 toy data for Φ , Φ_1 , $m(Z_1)$, $m(Z_2)$ and $|\cos\theta^*|$ in $H \rightarrow 4\ell$ and comparison with the theoretical predictions.

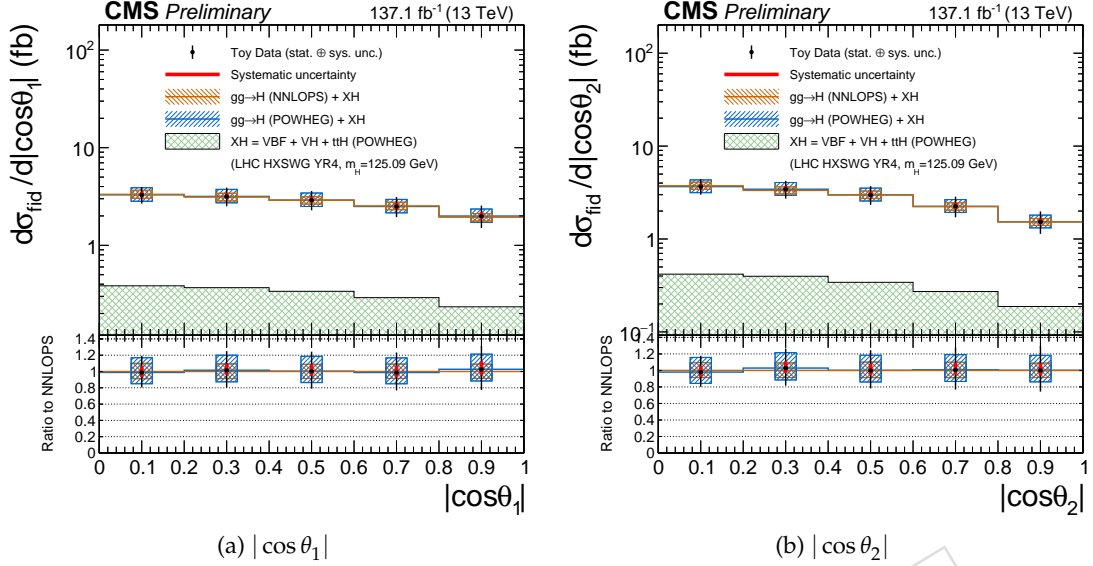


Figure 16: Differential fiducial cross section results using full Run 2 toy data for $|\cos \theta_1|$, $|\cos \theta_2|$ in $H \rightarrow 4\ell$ and comparison with the theoretical predictions. Systematic uncertainty is indicated by red bars and black bars show total statistical and the systematic uncertainties, combined in quadrature. The blue and brown colors show the theoretical predictions. The acceptances and the theoretical uncertainties in differential bins are computed using POWHEG. Sub-dominant production contributions $XH = VBF + VH + t\bar{t}H$ are shown in green separately. The systematic uncertainties correspond to the generators accuracy are also taken in to account for differential predictions. The fraction of 4μ , $4e$ and $2e2\mu$ in each differential bin is allowed to float in fit.

490 8.3 Double differential cross section measurements

491 Differential measurements are extended upto higher dimension upto 2. Several 2D combina-
492 tion are aimed to be measured e.g. $m(Z_1)$ vs $m(Z_2)$ and so forth. To be updated further.

493 8.4 Effective Field Theory interpretations

494 To be updated.

DRAFT

495 Appendix

496 **A Signal Shapes and Efficiencies**

497 For all plots showing fits to the signal distributions, the red histograms show the distribution of
498 events which pass both the fiducial selection at generator level and pass the full reconstruction
499 level selection, including the selection on $p_T(H)$. The red curve shows a fit to this distribution
500 using a double-sided crystal ball function, and the resulting σ of the fit is also shown on the
501 plot. The blue histograms show events which pass the full reconstruction level selection, and
502 pass the fiducial selection at generator level within a different $p_T(H)$ bin. The blue curves show
503 a fit to this distribution using the same function as the red curve with a different normalization.
504 The black histograms show the distribution of events which pass the full reconstruction level
505 selection but do not pass the fiducial selection at generator level, and the black curve shows a fit
506 to this distribution using the same function as the red curve but with a different normalization.
507 The yellow histogram shows events which pass the full reconstruction level selection but where
508 one of the four selected leptons does not originate from the Higgs boson. The yellow curve
509 shows a fit to this distribution using a Landau function.

510 **A.1 Fits in different bins of $p_T(H)$**

DRAFT

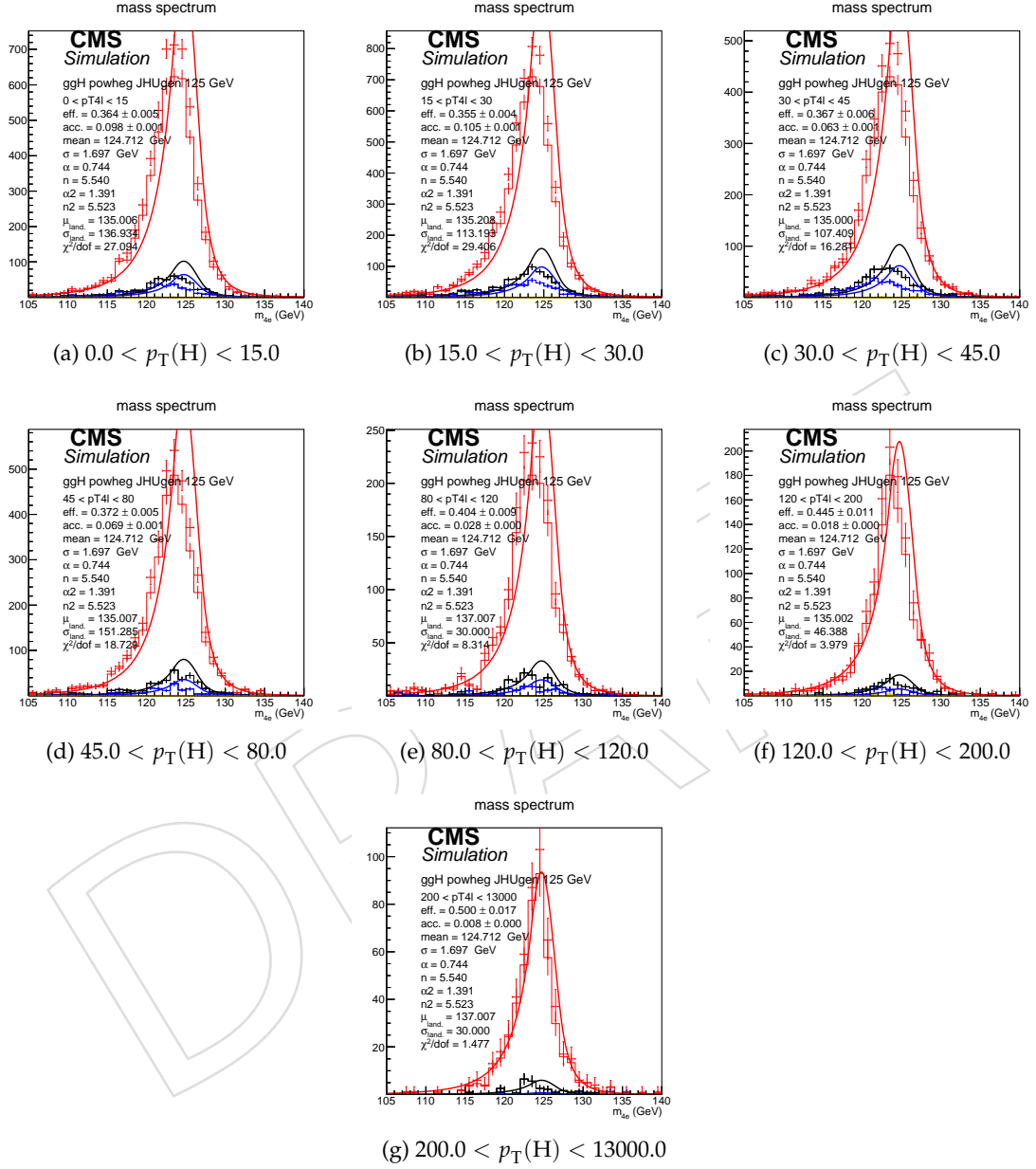


Figure 17: Example signal shapes at reconstruction level for a resonance of $m(4\ell)$ in $4e$ final state for the $gg \rightarrow H$ production mode from POWHEG+JHUGEN in different bins of $p_T(H)$. The black curve represents events which do not pass the fiducial volume selection. The curve has no effect on the result.

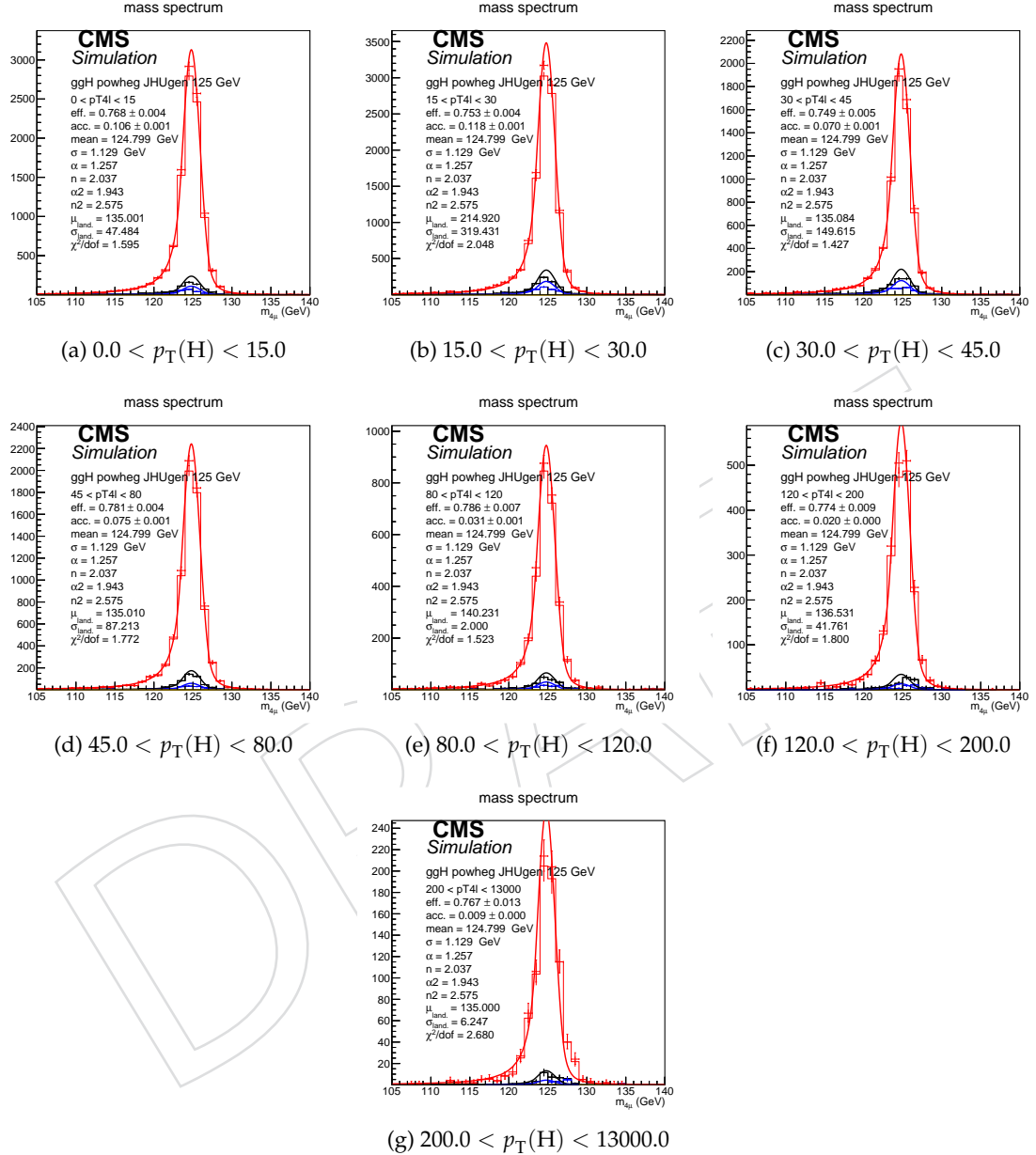


Figure 18: Example signal shapes at reconstruction level for a resonance of $m(4\ell)$ in 4μ final state for the $gg \rightarrow H$ production mode from POWHEG+JHUGEN in different bins of $p_T(H)$. The black curve represents events which do not pass the fiducial volume selection. The curve has no effect on the result.

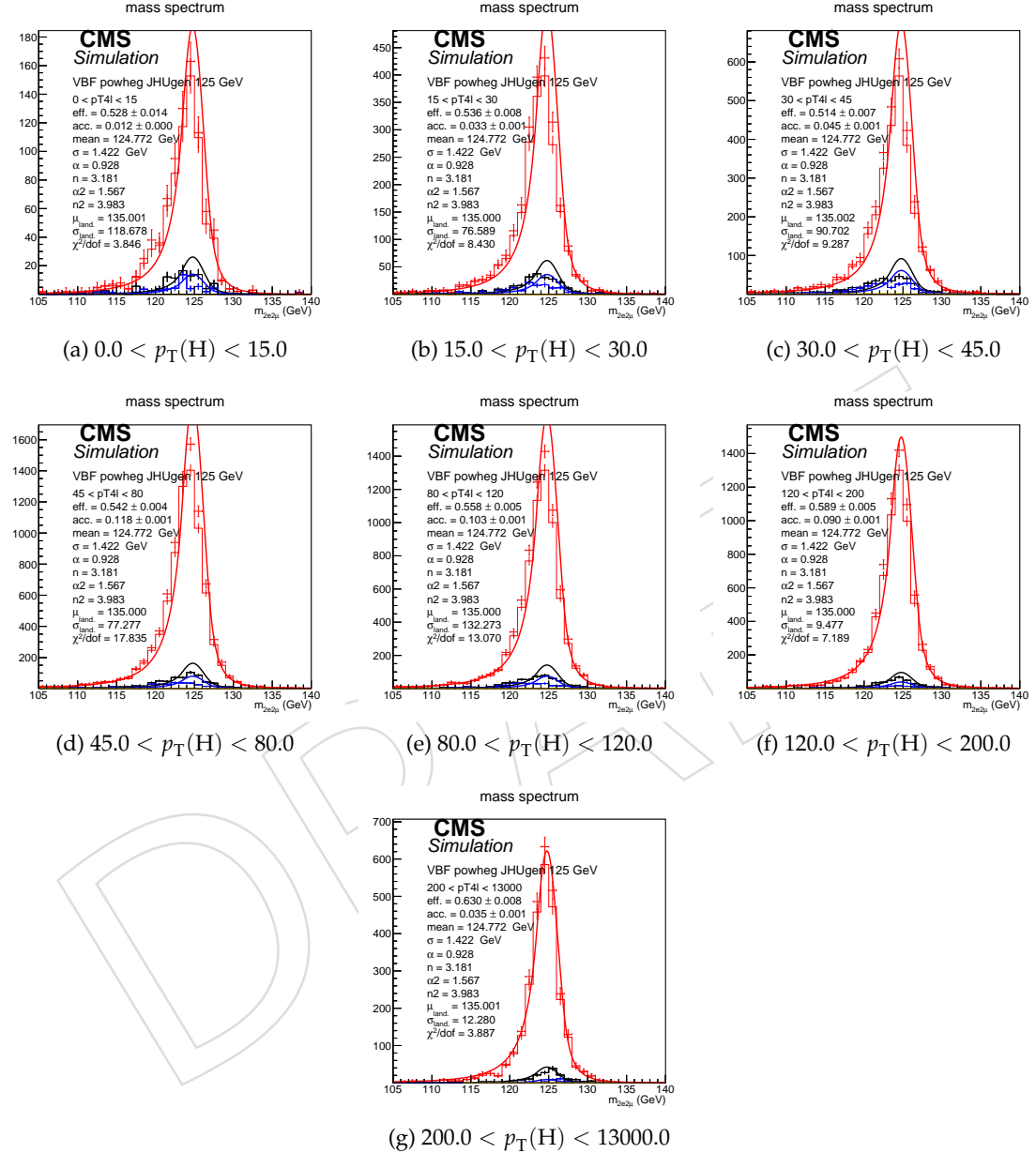


Figure 19: Example signal shapes at reconstruction level for a resonance of $m(4\ell)$ in $2e2\mu$ final state for the VBF production mode from POWHEG+JHUGEN in different bins of $p_T(H)$. The black curve represents events which do not pass the fiducial volume selection. The curve has no effect on the result.

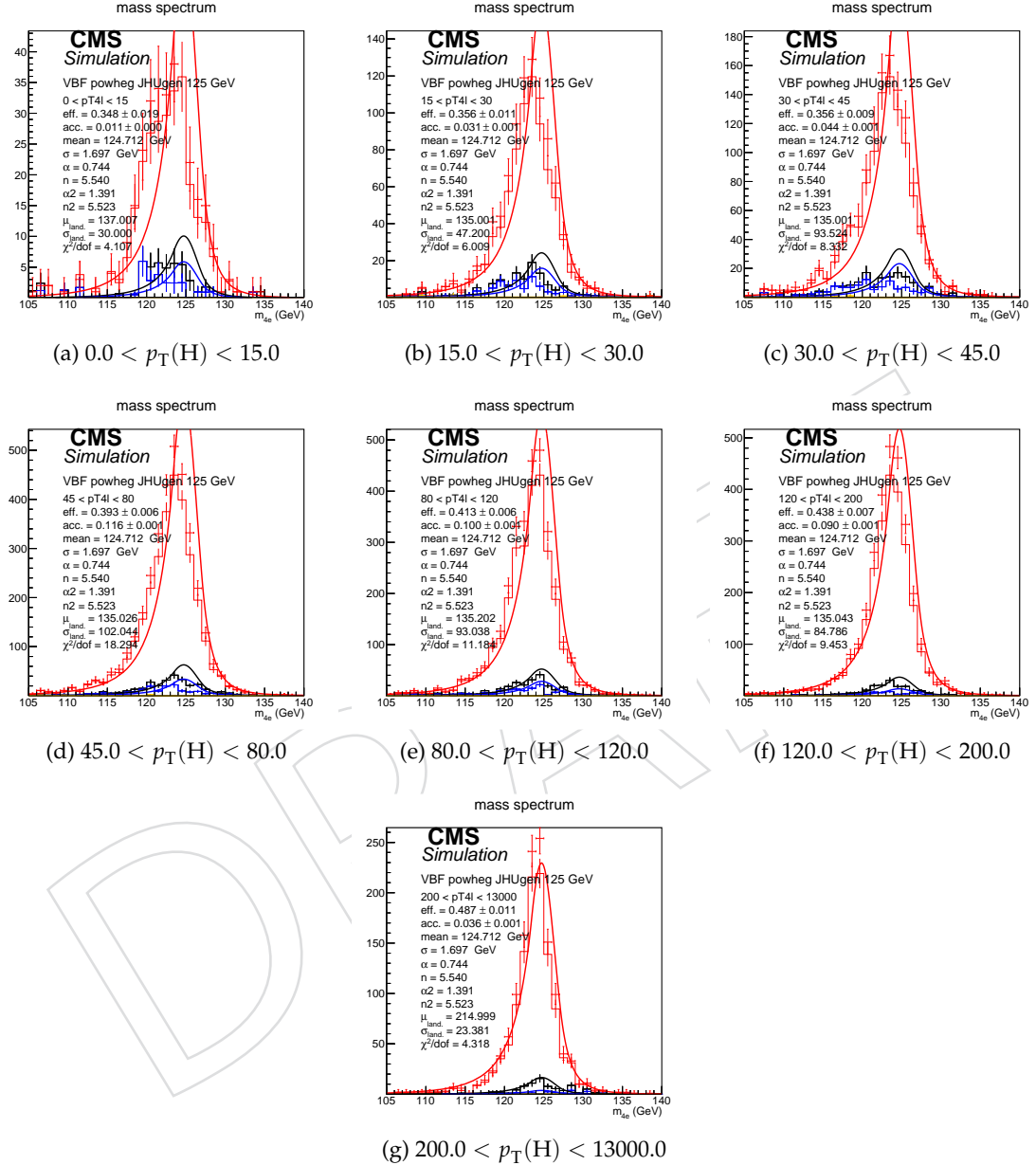


Figure 20: Example signal shapes at reconstruction level for a resonance of $m(4\ell)$ in $4e$ final state for the VBF production mode from POWHEG+JHUGEN in different bins of $p_{\text{T}}(\text{H})$. The black curve represents events which do not pass the fiducial volume selection. The curve has no effect on the result.

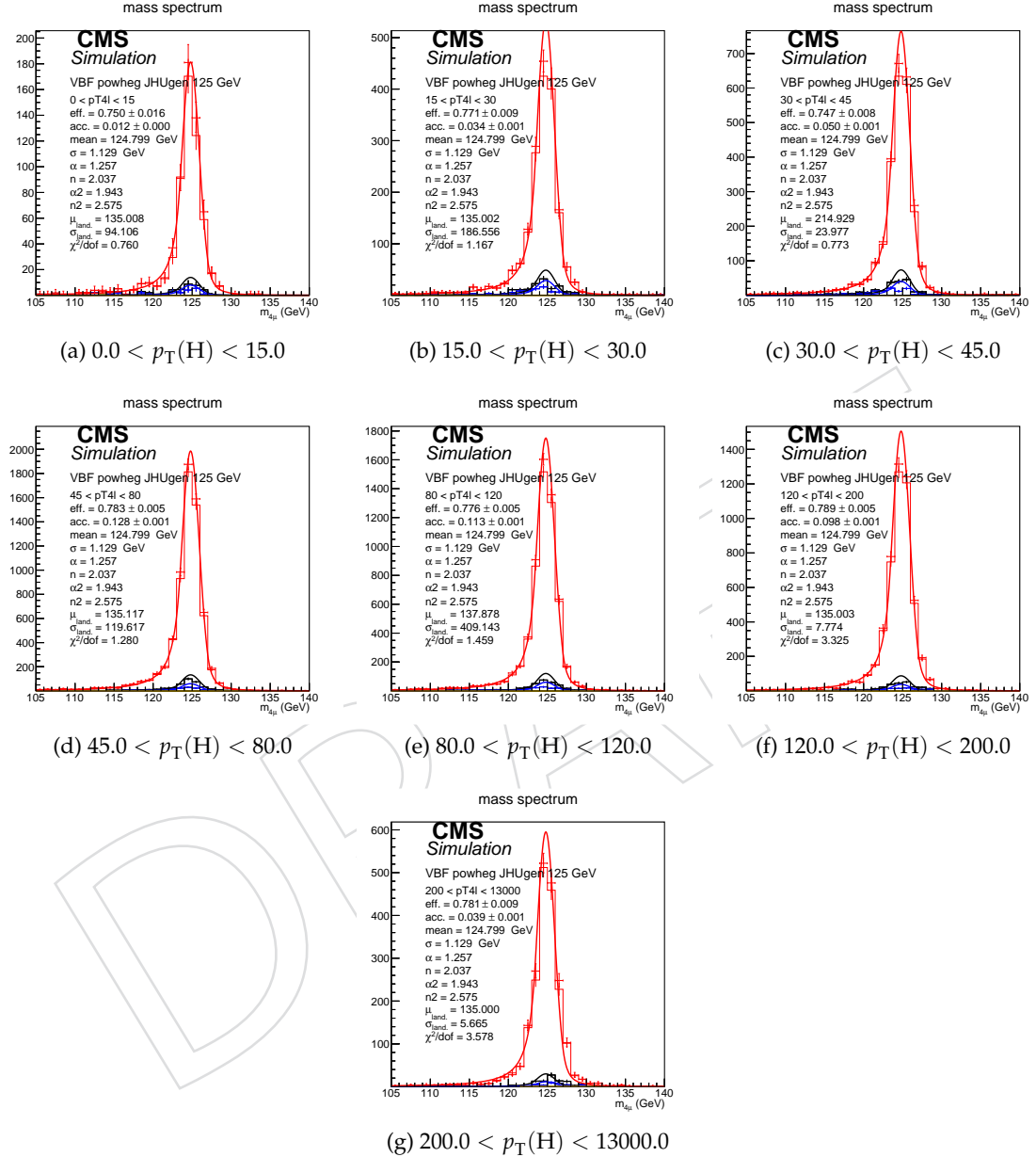


Figure 21: Example signal shapes at reconstruction level for a resonance of $m(4\ell)$ in 4μ final state for the VBF production mode from POWHEG+JHUGEN in different bins of $p_T(H)$. The black curve represents events which do not pass the fiducial volume selection. The curve has no effect on the result.

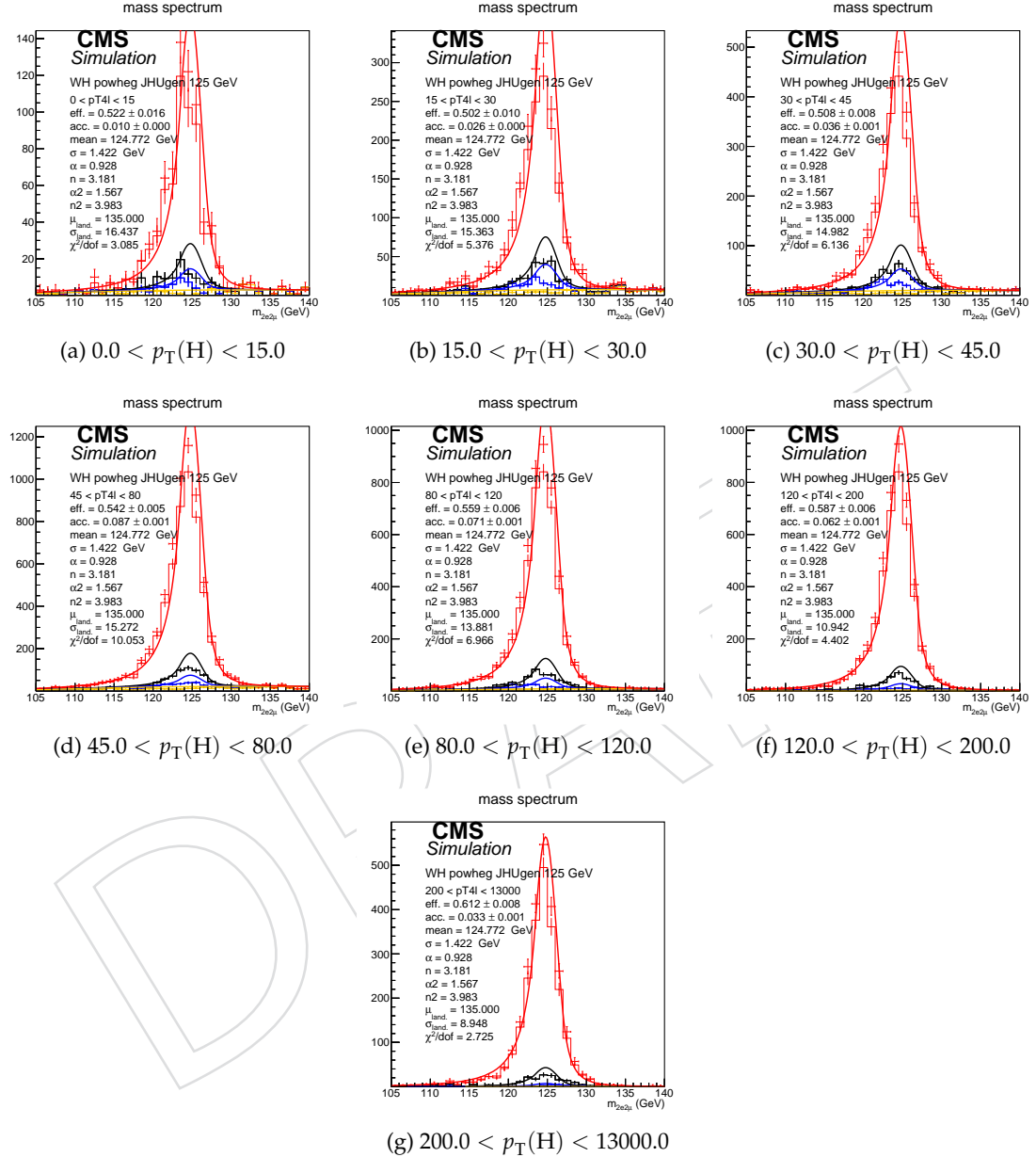


Figure 22: Example signal shapes at reconstruction level for a resonance of $m(4\ell)$ in $2e2\mu$ final state for the WH production mode from POWHEG+JHUGEN in different bins of $p_T(H)$. The black curve represents events which do not pass the fiducial volume selection. The curve has no effect on the result.

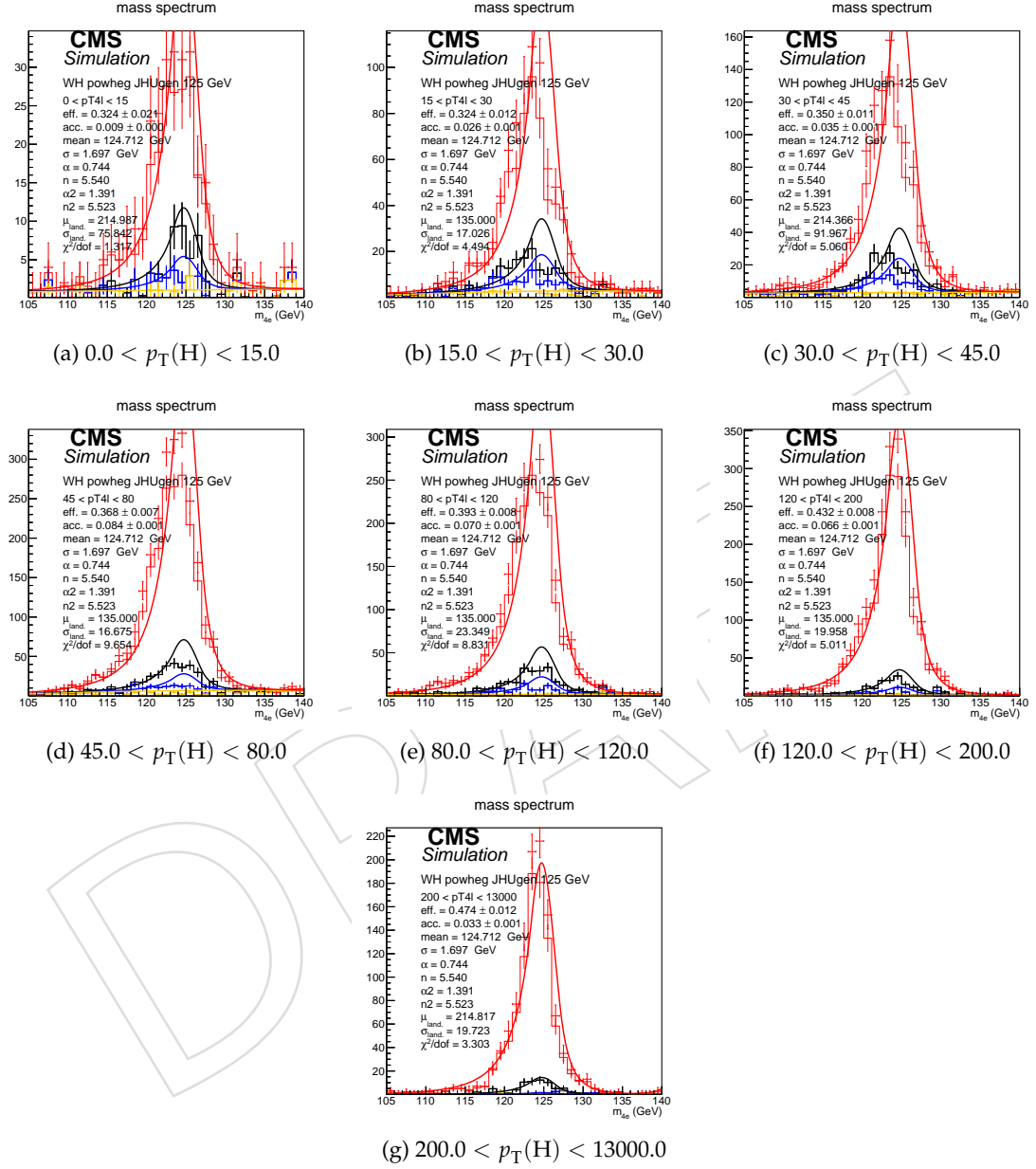


Figure 23: Example signal shapes at reconstruction level for a resonance of $m(4\ell)$ in $4e$ final state for the WH production mode from POWHEG+JHUGEN in different bins of $p_T(H)$. The black curve represents events which do not pass the fiducial volume selection. The curve has no effect on the result.

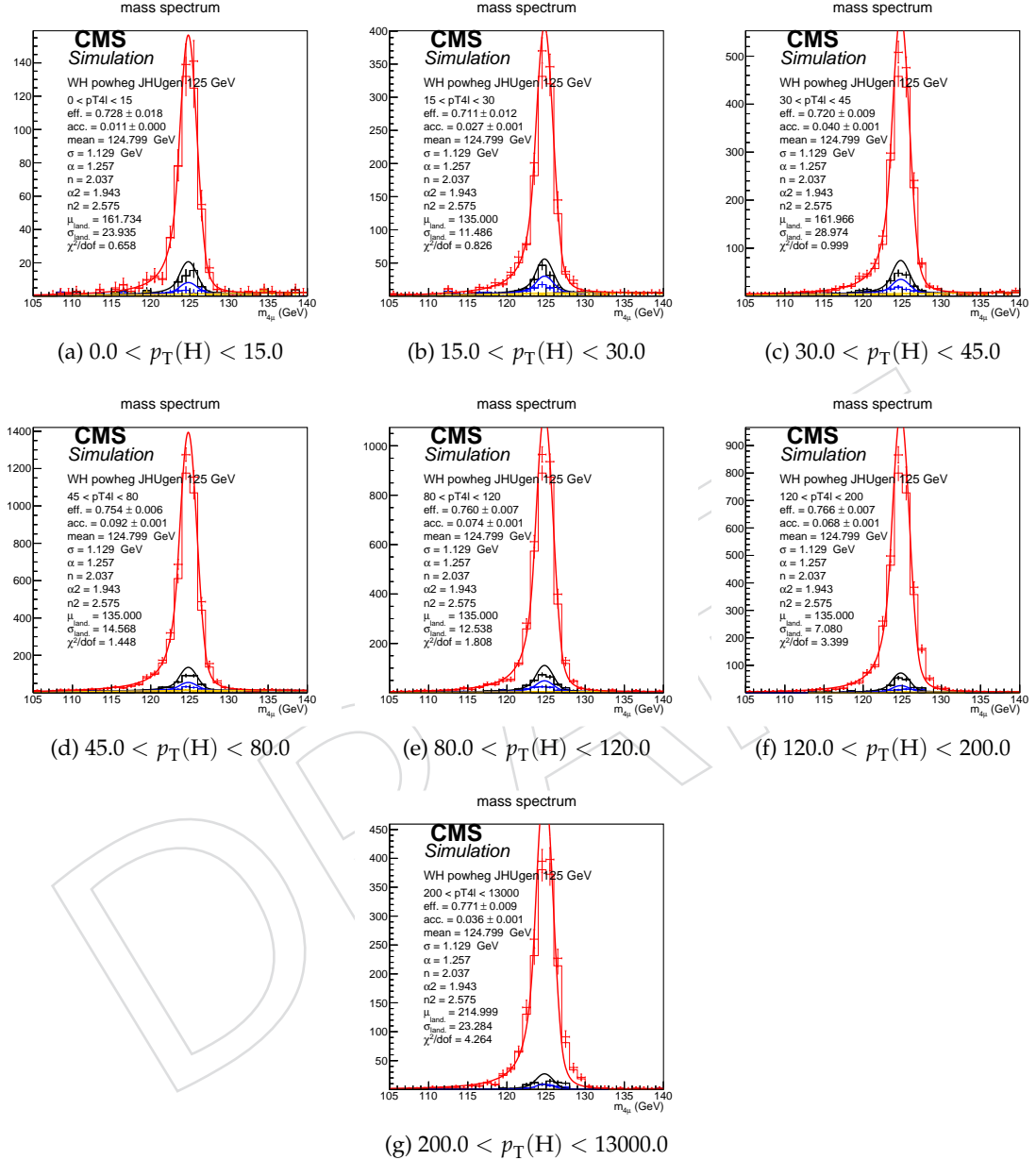


Figure 24: Example signal shapes at reconstruction level for a resonance of $m(4\ell)$ in 4μ final state for the $gg \rightarrow H$ production mode from POWHEG+JHUGEN in different bins of $p_T(H)$. The black curve represents events which do not pass the fiducial volume selection. The curve has no effect on the result.

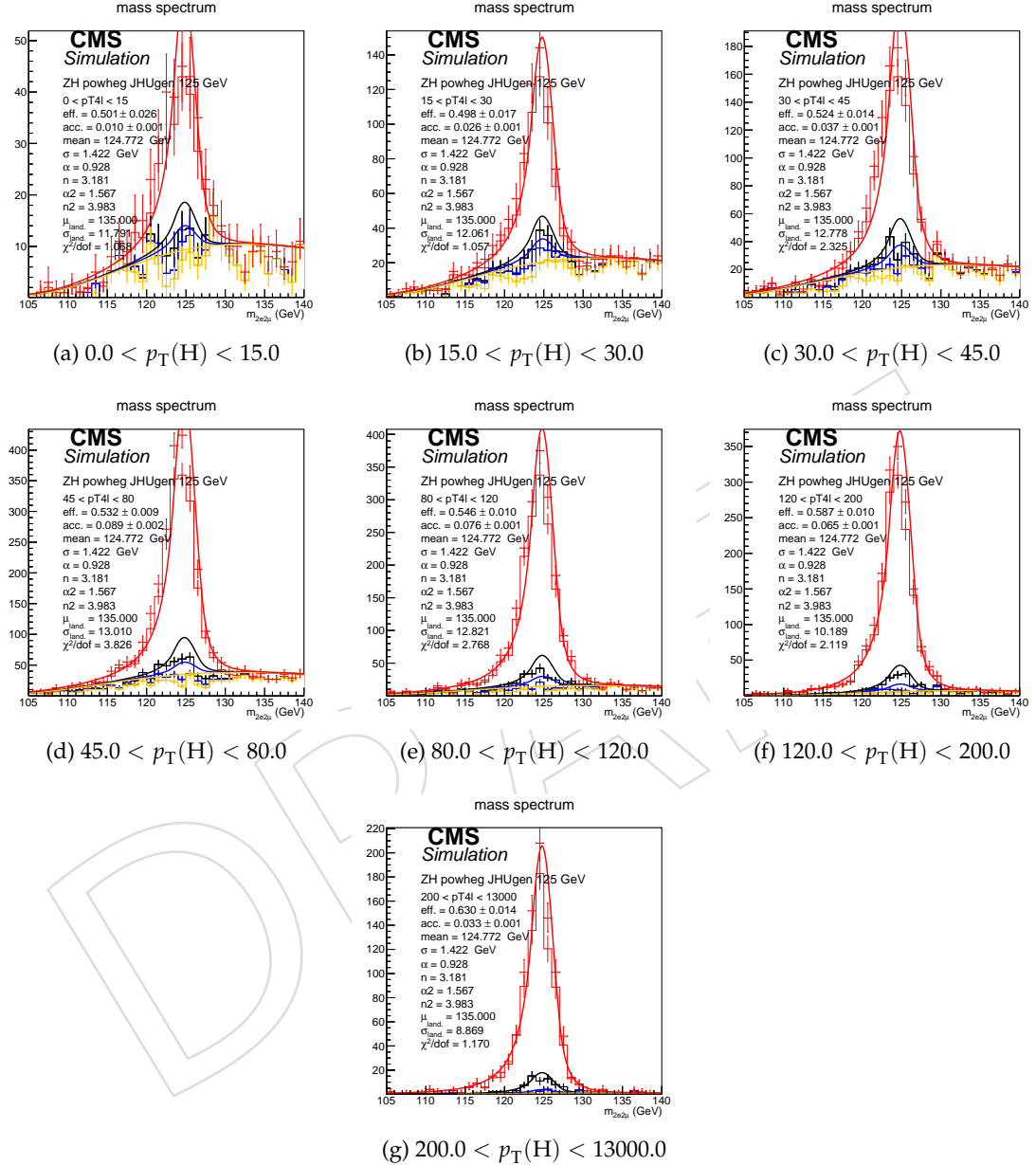


Figure 25: Example signal shapes at reconstruction level for a resonance of $m(4\ell)$ in $2e2\mu$ final state for the ZH production mode from POWHEG+JHUGEN in different bins of $p_{\text{T}}(\text{H})$. The black curve represents events which do not pass the fiducial volume selection. The curve has no effect on the result.

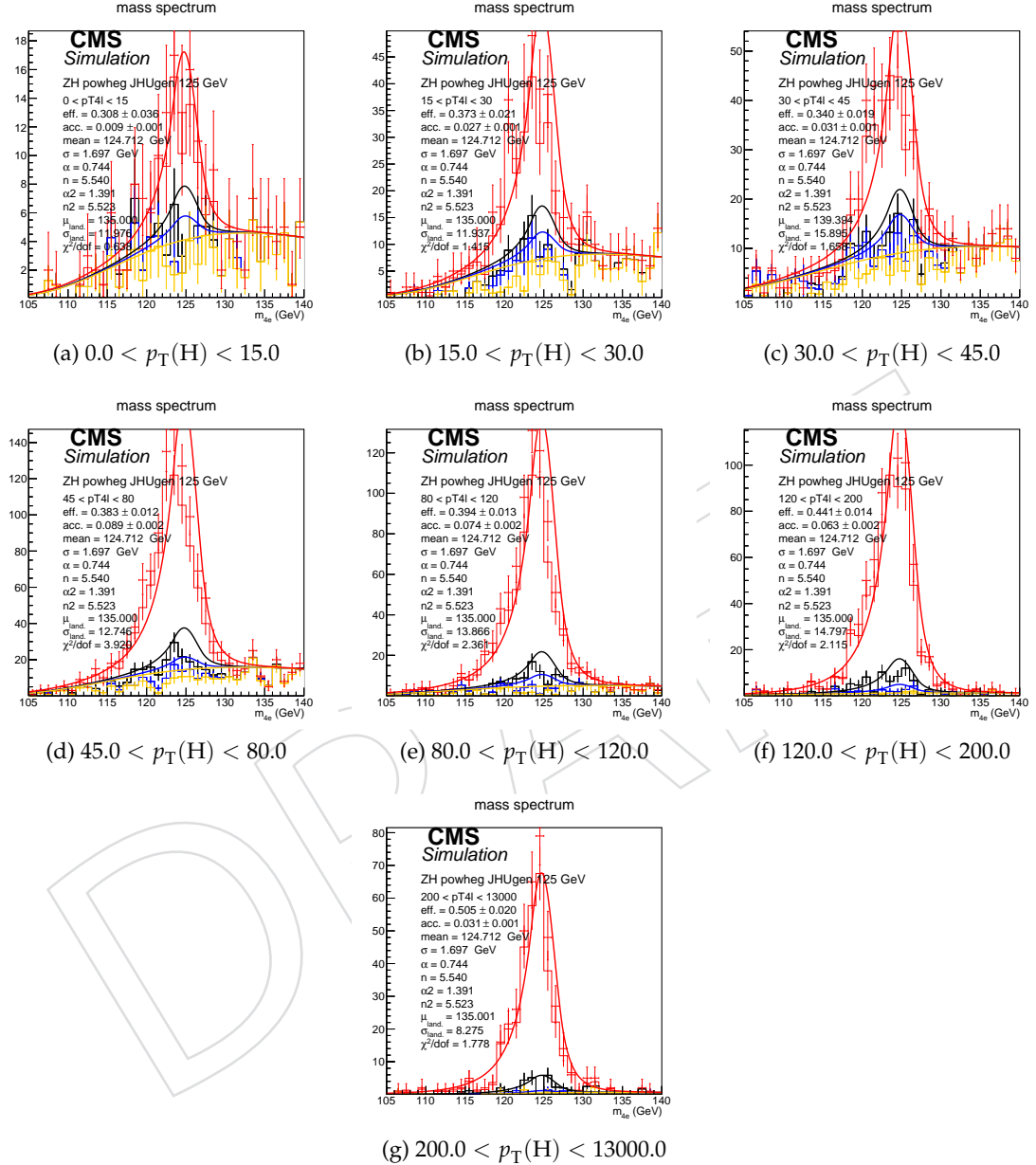


Figure 26: Example signal shapes at reconstruction level for a resonance of $m(4\ell)$ in $4e$ final state for the ZH production mode from POWHEG+JHUGEN in different bins of $p_T(H)$. The black curve represents events which do not pass the fiducial volume selection. The curve has no effect on the result.

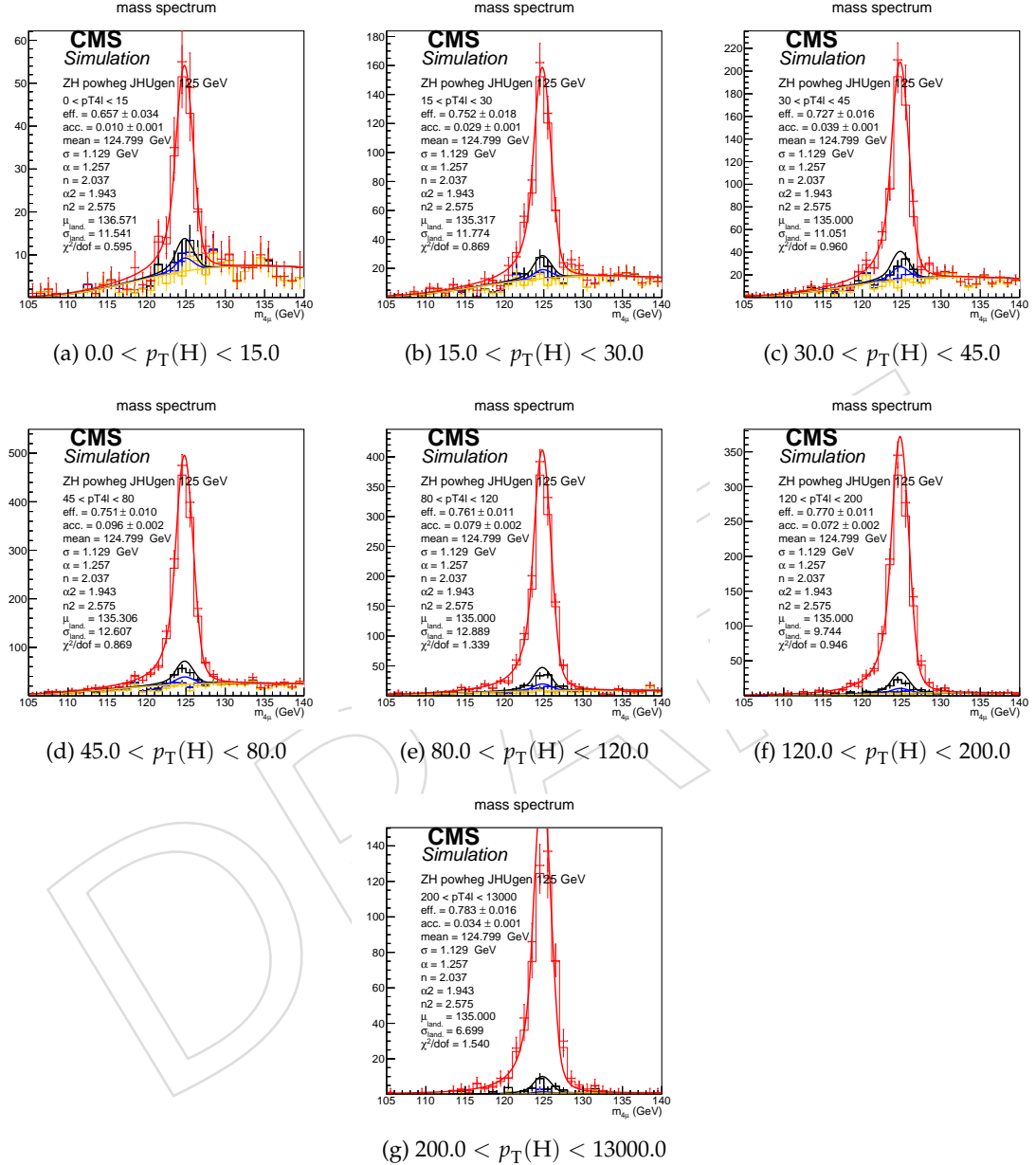


Figure 27: Example signal shapes at reconstruction level for a resonance of $m(4\ell)$ in 4μ final state for the ZH production mode from POWHEG+JHUGEN in different bins of $p_T(H)$. The black curve represents events which do not pass the fiducial volume selection. The curve has no effect on the result.

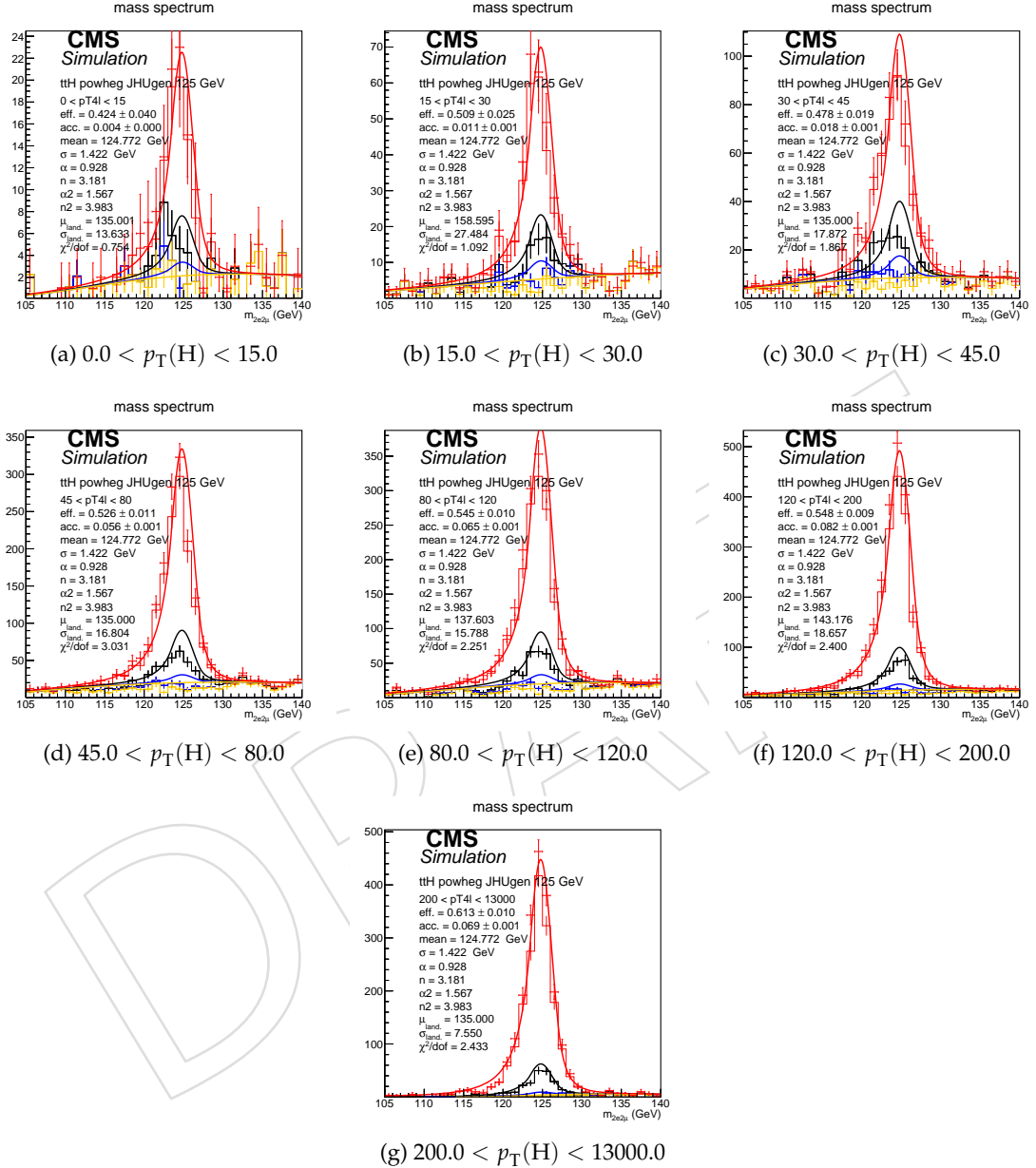


Figure 28: Example signal shapes at reconstruction level for a resonance of $m(4\ell)$ in $2e2\mu$ final state for the $t\bar{t}H$ production mode from POWHEG+JHUGEN in different bins of $p_T(H)$. The black curve represents events which do not pass the fiducial volume selection. The curve has no effect on the result.

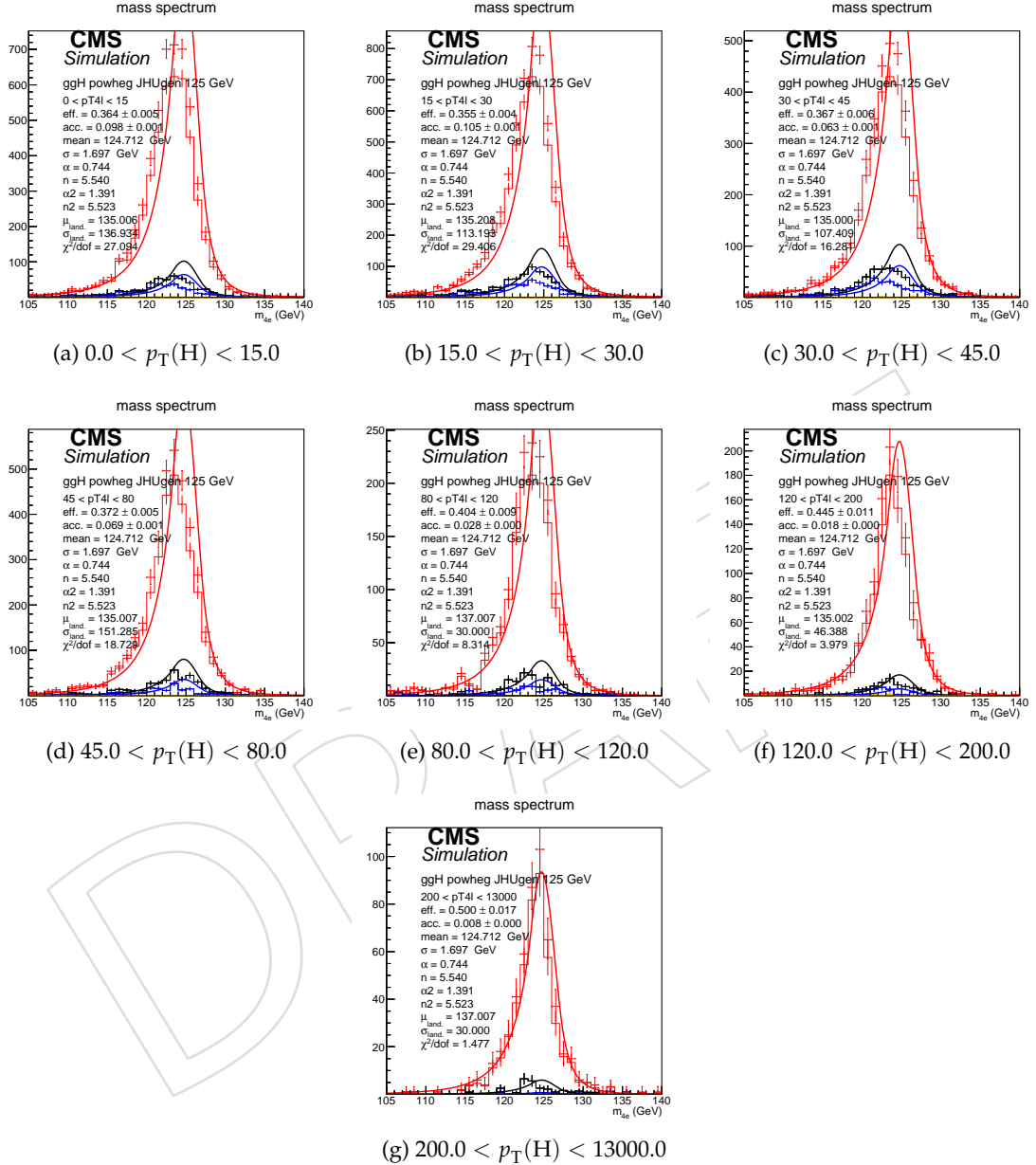


Figure 29: Example signal shapes at reconstruction level for a resonance of $m(4\ell)$ in $4e$ final state for the $t\bar{t}H$ production mode from POWHEG+JHUGEN in different bins of $p_T(H)$. The black curve represents events which do not pass the fiducial volume selection. The curve has no effect on the result.

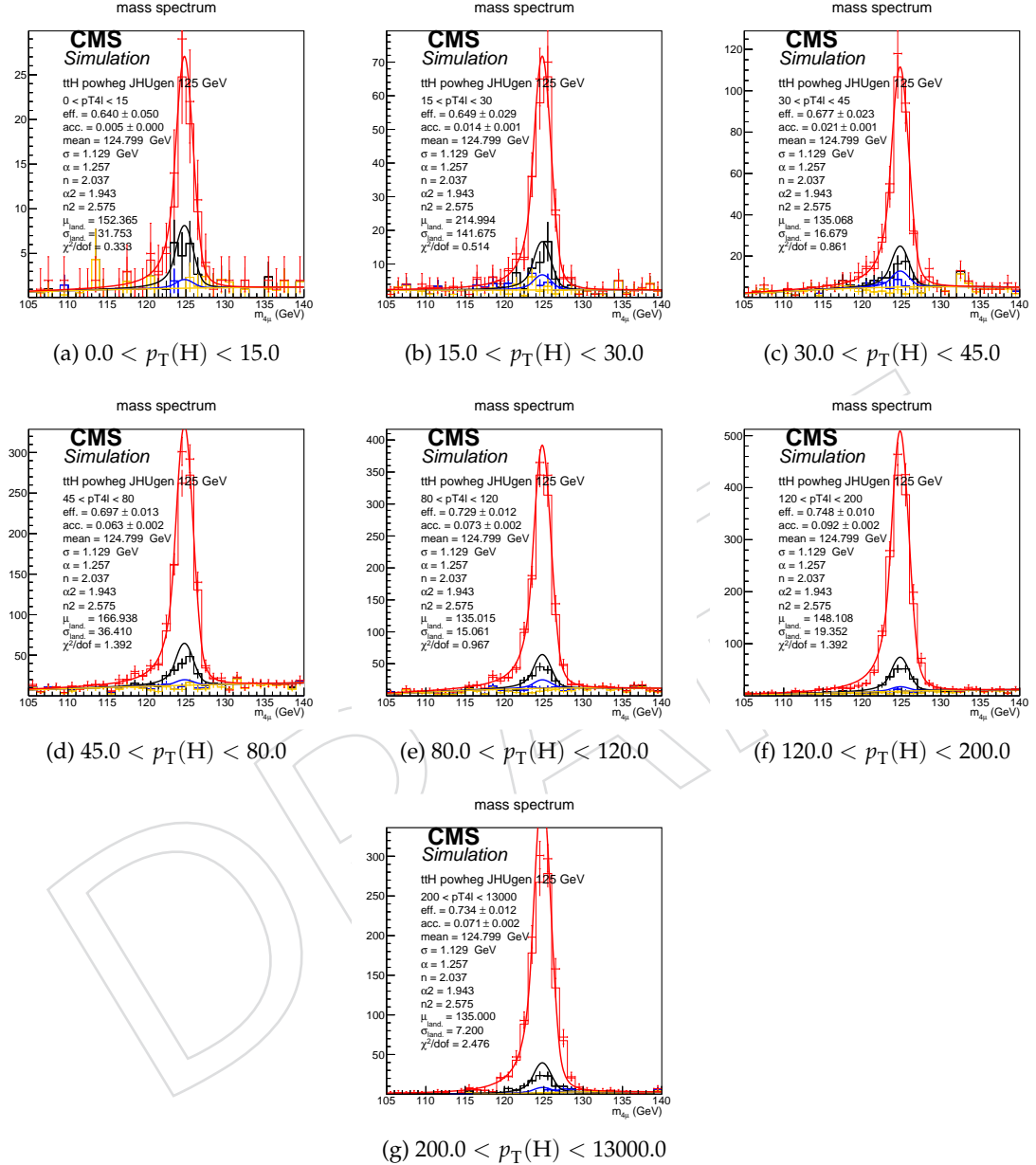


Figure 30: Example signal shapes at reconstruction level for a resonance of $m(4\ell)$ in 4μ final state for the $t\bar{t}H$ production mode from POWHEG+JHUGEN in different bins of $p_T(H)$. The black curve represents events which do not pass the fiducial volume selection. The curve has no effect on the result.

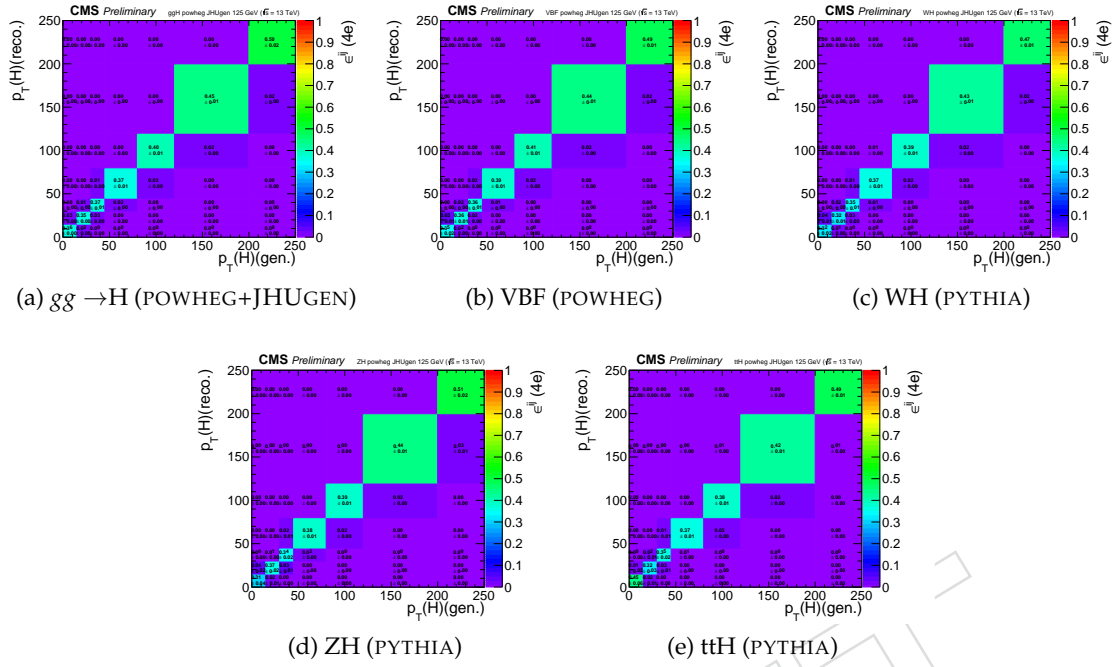


Figure 31: Efficiency matrices for $p_T(H)$ for different SM production modes in the $4e$ final state.

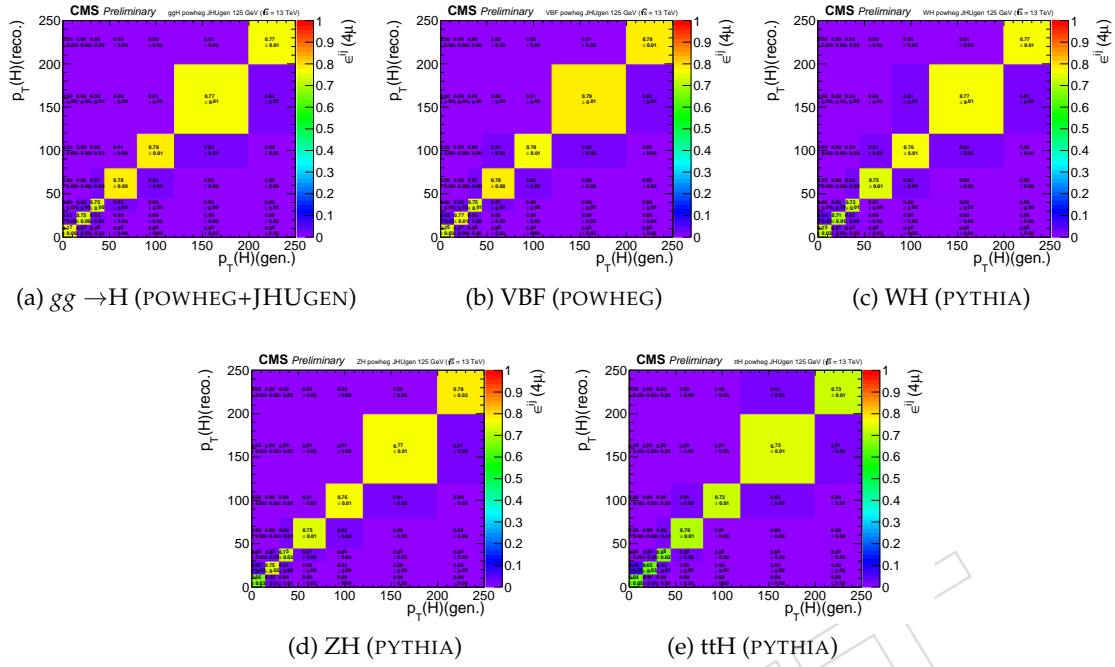


Figure 32: Efficiency matrices for $p_T(H)$ for different SM production modes in the 4μ final state.

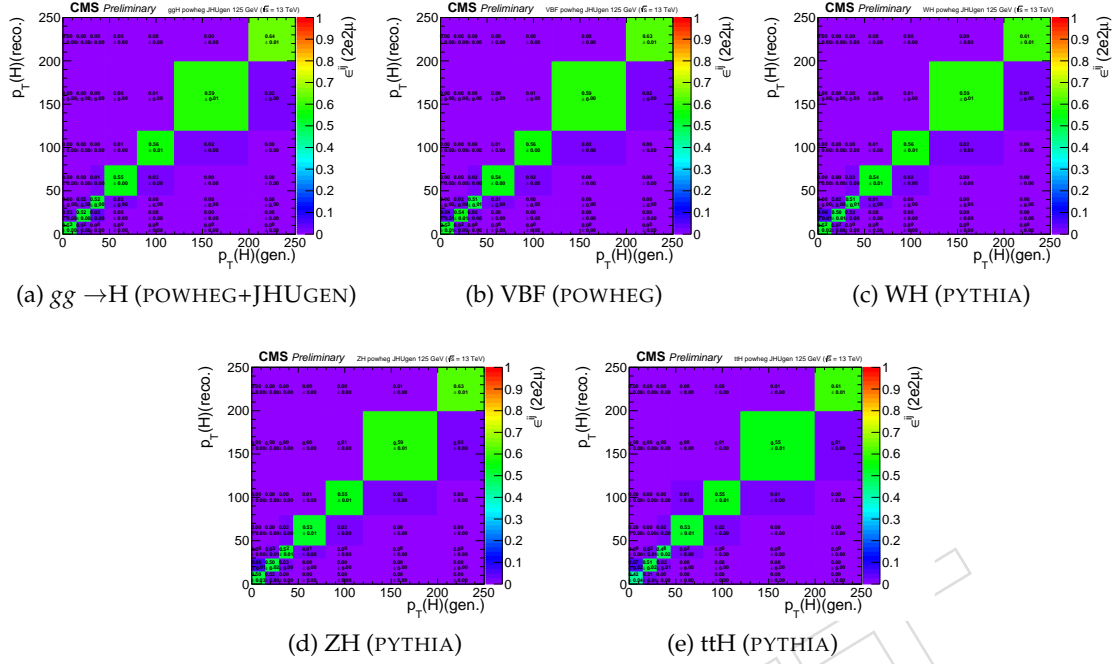


Figure 33: Efficiency matrices for $p_T(H)$ for different SM production modes in the $2e2\mu$ final state.

511 **A.2 Signal inputs in different bins of $|y(H)|$**

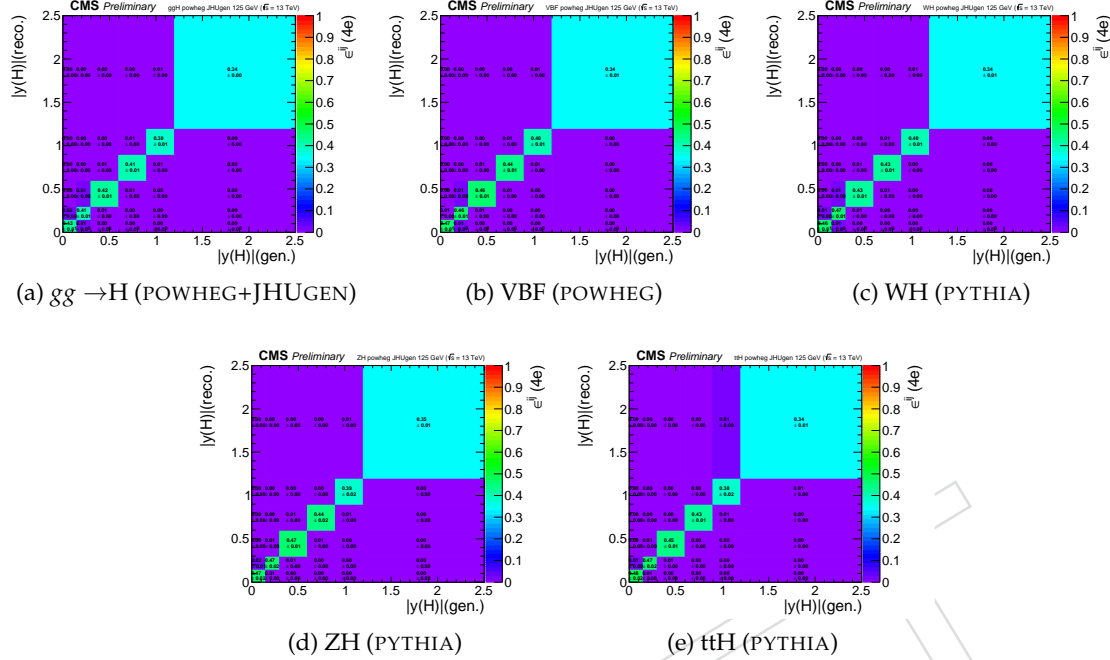


Figure 34: Efficiency matrices for $|y(H)|$ for different SM production modes in the $4e$ final state.

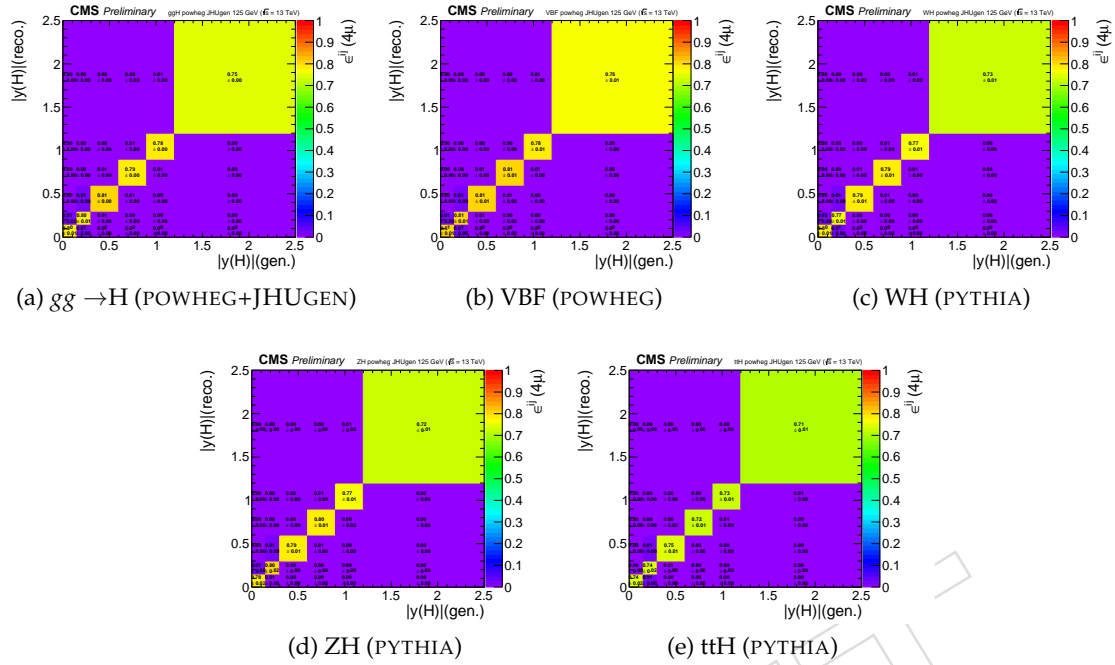


Figure 35: Efficiency matrices for $|y(H)|$ for different SM production modes in the 4μ final state.

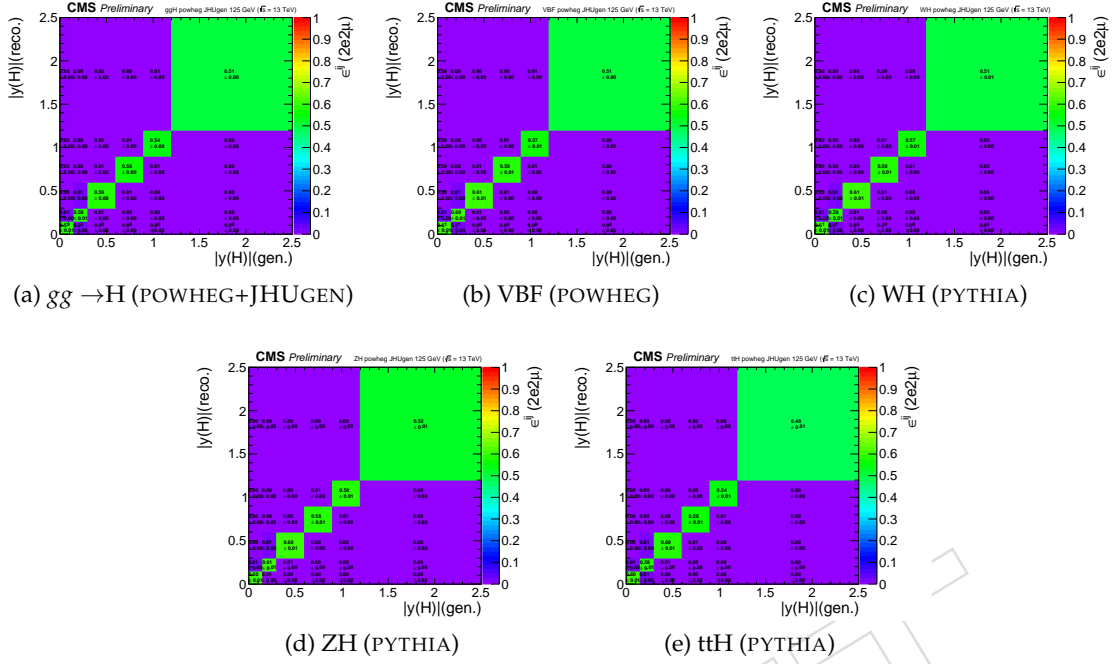


Figure 36: Efficiency matrices for $|y(H)|$ for different SM production modes in the $2e2\mu$ final state.

512 **A.3 Fits in different bins of N(jets)**

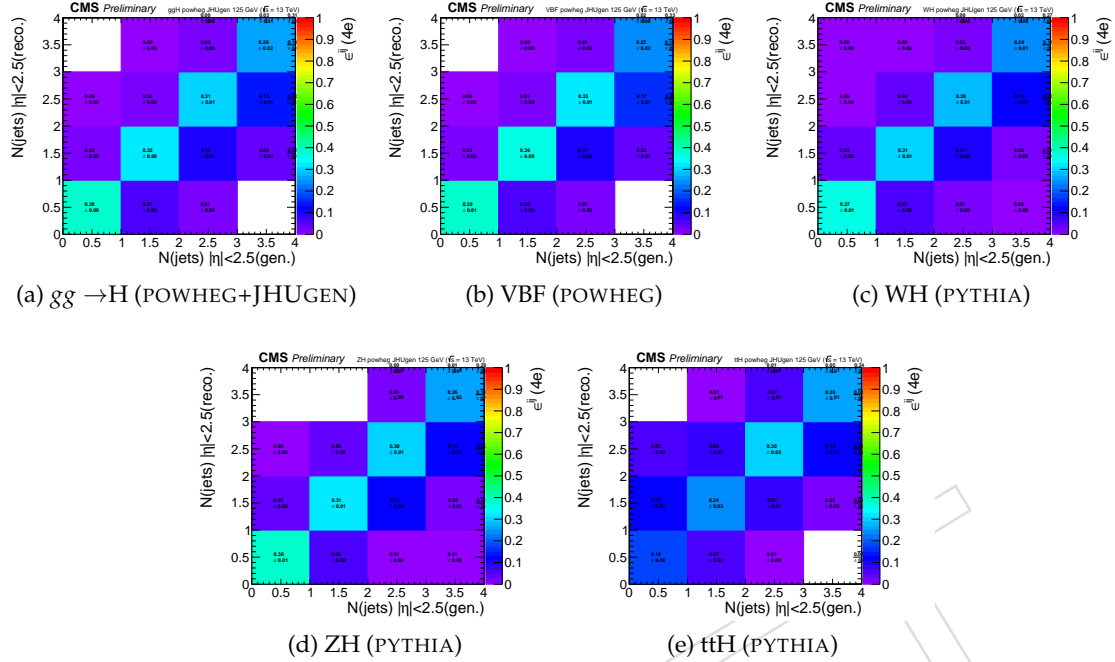


Figure 37: Efficiency matrices for $N(\text{jets})$ for different SM production modes in the $4e$ final state.

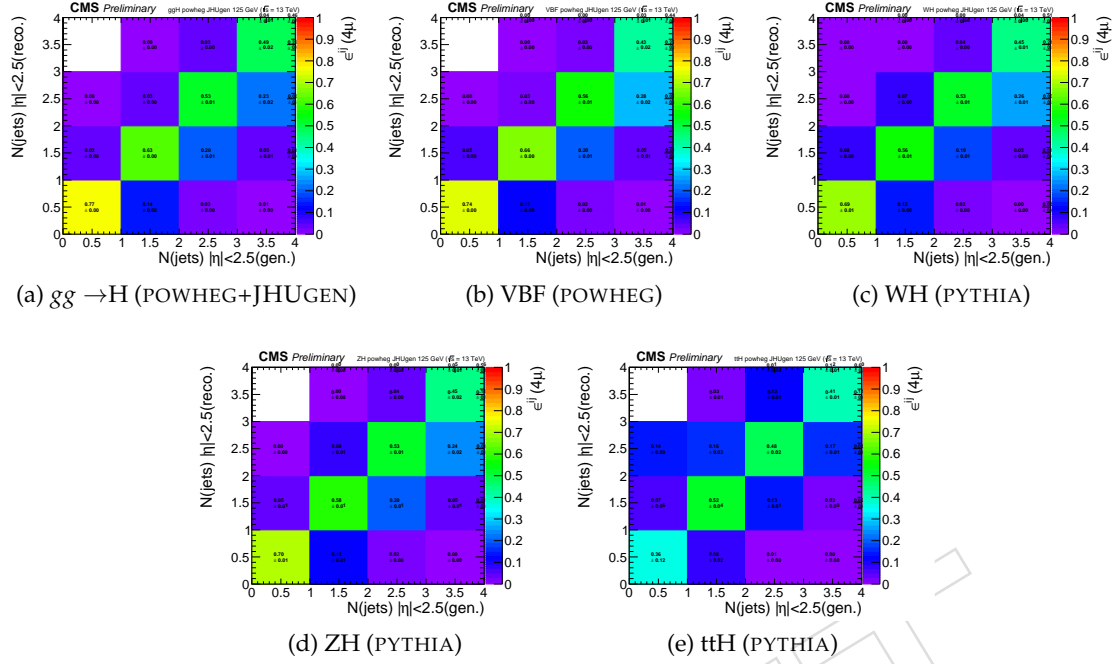


Figure 38: Efficiency matrices for $N(\text{jets})$ for different SM production modes in the 4μ final state.

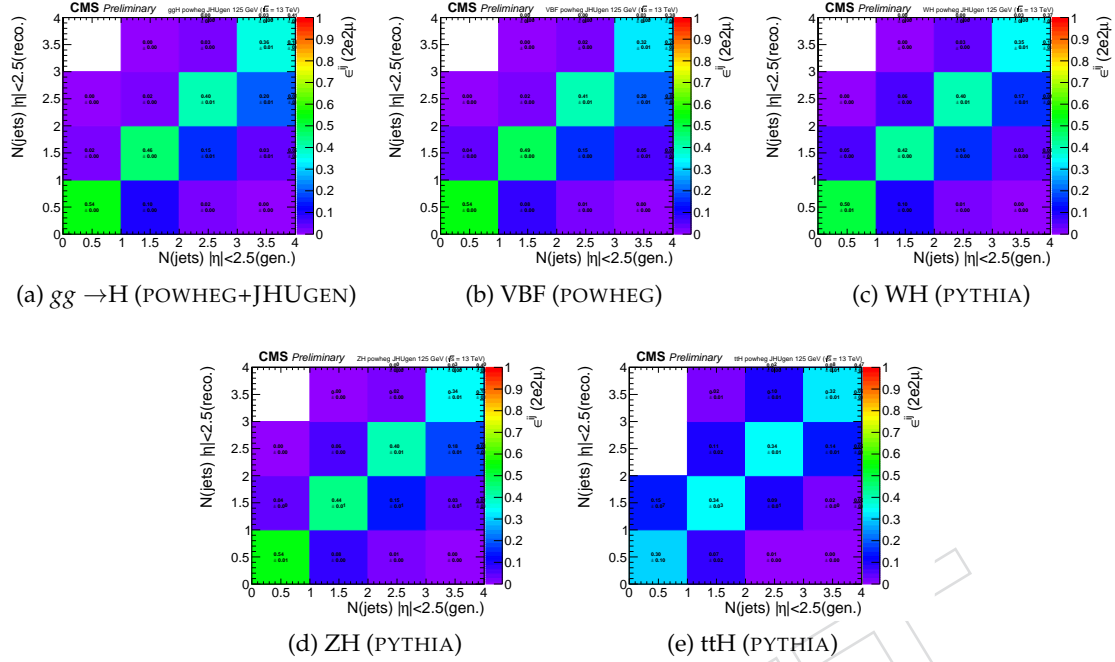


Figure 39: Efficiency matrices for $N(\text{jets})$ for different SM production modes in the $2e2\mu$ final state.

513 References

- 514 [1] CMS Collaboration, "Observation of a new boson at a mass of 125 GeV with the CMS
 515 experiment at the LHC", *Phys. Lett. B* **716** (2012) 30,
 516 doi:10.1016/j.physletb.2012.08.021, arXiv:1207.7235.
- 517 [2] ATLAS Collaboration, "Observation of a new particle in the search for the Standard
 518 Model Higgs boson with the ATLAS detector at the LHC", *Phys. Lett. B* **716** (2012) 1,
 519 doi:10.1016/j.physletb.2012.08.020, arXiv:1207.7214.
- 520 [3] F. Englert and R. Brout, "Broken Symmetry and the Mass of Gauge Vector Mesons",
 521 *Phys. Rev. Lett.* **13** (1964) 321, doi:10.1103/PhysRevLett.13.321.
- 522 [4] P. W. Higgs, "Broken symmetries, massless particles and gauge fields", *Phys. Lett.* **12**
 523 (1964) 132, doi:10.1016/0031-9163(64)91136-9.
- 524 [5] P. W. Higgs, "Broken Symmetries and the Masses of Gauge Bosons", *Phys. Rev. Lett.* **13**
 525 (1964) 508, doi:10.1103/PhysRevLett.13.508.
- 526 [6] G. Guralnik, C. Hagen, and T. Kibble, "Global Conservation Laws and Massless
 527 Particles", *Phys. Rev. Lett.* **13** (1964) 585, doi:10.1103/PhysRevLett.13.585.
- 528 [7] P. W. Higgs, "Spontaneous Symmetry Breakdown without Massless Bosons", *Phys. Rev.*
 529 **145** (1966) 1156, doi:10.1103/PhysRev.145.1156.
- 530 [8] T. Kibble, "Symmetry breaking in nonAbelian gauge theories", *Phys. Rev.* **155** (1967)
 531 1554, doi:10.1103/PhysRev.155.1554.
- 532 [9] CMS Collaboration, "Precise determination of the mass of the Higgs boson and tests of
 533 compatibility of its couplings with the standard model predictions using proton
 534 collisions at 7 and 8 TeV", *Eur. Phys. J. C* **75** (2015) 212,
 535 doi:10.1140/epjc/s10052-015-3351-7, arXiv:1412.8662.
- 536 [10] ATLAS Collaboration, "Measurements of the Higgs boson production and decay rates
 537 and coupling strengths using pp collision data at $\sqrt{s} = 7$ and 8 TeV in the ATLAS
 538 experiment", *Eur. Phys. J. C* **76** (2016) doi:10.1140/epjc/s10052-015-3769-y,
 539 arXiv:1507.04548.
- 540 [11] ATLAS, CMS Collaboration, "Combined Measurement of the Higgs Boson Mass in pp
 541 Collisions at $\sqrt{s} = 7$ and 8 TeV with the ATLAS and CMS Experiments", *Phys. Rev. Lett.*
 542 **114** (2015) 191803, doi:10.1103/PhysRevLett.114.191803, arXiv:1503.07589.
- 543 [12] CMS Collaboration, "Measurements of the Higgs boson production and decay rates and
 544 constraints on its couplings from a combined ATLAS and CMS analysis of the LHC pp
 545 collision data at $\sqrt{s} = 7$ and 8 TeV", CMS Physics Analysis Summary
 546 CMS-PAS-HIG-15-002, 2015.
- 547 [13] CMS Collaboration, "Measurement of the properties of a Higgs boson in the four-lepton
 548 final state", *Phys. Rev. D* **89** (2014) 092007, doi:10.1103/PhysRevD.89.092007,
 549 arXiv:1312.5353.
- 550 [14] CMS Collaboration, "Study of the Mass and Spin-Parity of the Higgs Boson Candidate
 551 via Its Decays to Z Boson Pairs", *Phys. Rev. Lett.* **110** (2013) 081803,
 552 doi:10.1103/PhysRevLett.110.081803, arXiv:1212.6639.

- 553 [15] CMS Collaboration, “Constraints on the spin-parity and anomalous HVV couplings of
554 the Higgs boson in proton collisions at 7 and 8 TeV”, *Phys. Rev. D* **92** (2015) 012004,
555 doi:[10.1103/PhysRevD.92.012004](https://doi.org/10.1103/PhysRevD.92.012004), arXiv:[1411.3441](https://arxiv.org/abs/1411.3441).
- 556 [16] CMS Collaboration, “Constraints on the Higgs boson width from off-shell production
557 and decay to Z-boson pairs”, *Phys. Lett. B* **736** (2014) 64,
558 doi:[10.1016/j.physletb.2014.06.077](https://doi.org/10.1016/j.physletb.2014.06.077), arXiv:[1405.3455](https://arxiv.org/abs/1405.3455).
- 559 [17] CMS Collaboration, “Limits on the Higgs boson lifetime and width from its decay to four
560 charged leptons”, *Phys. Rev. D* **92** (2015) 072010,
561 doi:[10.1103/PhysRevD.92.072010](https://doi.org/10.1103/PhysRevD.92.072010), arXiv:[1507.06656](https://arxiv.org/abs/1507.06656).
- 562 [18] CMS Collaboration, “Measurement of differential and integrated fiducial cross sections
563 for higgs boson production in the four-lepton decay channel in pp collisions at $\sqrt{s} = 7$
564 and 8 tev”, arXiv:[1512.08377](https://arxiv.org/abs/1512.08377).
- 565 [19] CMS Collaboration, “Measurements of properties of the higgs boson in the four-lepton
566 final state at $\sqrt{s}=13$ tev with full run ii data”, CMS Physics Analysis Summary
567 CMS-PAS-HIG-19-001, 2019.
- 568 [20] S. Alioli, P. Nason, C. Oleari, and E. Re, “NLO vector-boson production matched with
569 shower in POWHEG”, *JHEP* **07** (2008) 060,
570 doi:[10.1088/1126-6708/2008/07/060](https://doi.org/10.1088/1126-6708/2008/07/060), arXiv:[0805.4802](https://arxiv.org/abs/0805.4802).
- 571 [21] P. Nason, “A new method for combining NLO QCD with shower Monte Carlo
572 algorithms”, *JHEP* **11** (2004) 040, doi:[10.1088/1126-6708/2004/11/040](https://doi.org/10.1088/1126-6708/2004/11/040),
573 arXiv:[hep-ph/0409146](https://arxiv.org/abs/hep-ph/0409146).
- 574 [22] S. Frixione, P. Nason, and C. Oleari, “Matching NLO QCD computations with parton
575 shower simulations: the POWHEG method”, *JHEP* **11** (2007) 070,
576 doi:[10.1088/1126-6708/2007/11/070](https://doi.org/10.1088/1126-6708/2007/11/070), arXiv:[0709.2092](https://arxiv.org/abs/0709.2092).
- 577 [23] E. Bagnaschi, G. Degrassi, P. Slavich, and A. Vicini, “Higgs production via gluon fusion
578 in the POWHEG approach in the SM and in the MSSM”, *JHEP* **02** (2012) 088,
579 doi:[10.1007/JHEP02\(2012\)088](https://doi.org/10.1007/JHEP02(2012)088), arXiv:[1111.2854](https://arxiv.org/abs/1111.2854).
- 580 [24] P. Nason and C. Oleari, “NLO Higgs boson production via vector-boson fusion matched
581 with shower in POWHEG”, *JHEP* **02** (2010) 037, doi:[10.1007/JHEP02\(2010\)037](https://doi.org/10.1007/JHEP02(2010)037),
582 arXiv:[0911.5299](https://arxiv.org/abs/0911.5299).
- 583 [25] H. B. Hartanto, B. Jager, L. Reina, and D. Wackerlo, “Higgs boson production in
584 association with top quarks in the POWHEG BOX”, *Phys. Rev. D* **91** (2015), no. 9, 094003,
585 doi:[10.1103/PhysRevD.91.094003](https://doi.org/10.1103/PhysRevD.91.094003), arXiv:[1501.04498](https://arxiv.org/abs/1501.04498).
- 586 [26] G. Luisoni, P. Nason, C. Oleari, and F. Tramontano, “ $HW^\pm/HZ + 0$ and 1 jet at NLO with
587 the POWHEG BOX interfaced to GoSam and their merging within MiNLO”, *JHEP* **10**
588 (2013) 083, doi:[10.1007/JHEP10\(2013\)083](https://doi.org/10.1007/JHEP10(2013)083), arXiv:[1306.2542](https://arxiv.org/abs/1306.2542).
- 589 [27] Y. Gao et al., “Spin determination of single-produced resonances at hadron colliders”,
590 *Phys. Rev. D* **81** (2010) 075022, doi:[10.1103/PhysRevD.81.075022](https://doi.org/10.1103/PhysRevD.81.075022),
591 arXiv:[1001.3396](https://arxiv.org/abs/1001.3396). [Erratum: doi:[10.1103/PhysRevD.81.079905](https://doi.org/10.1103/PhysRevD.81.079905)].
- 592 [28] NNPDF Collaboration, “Parton distributions for the LHC Run II”, *JHEP* **04** (2015) 040,
593 doi:[10.1007/JHEP04\(2015\)040](https://doi.org/10.1007/JHEP04(2015)040), arXiv:[1410.8849](https://arxiv.org/abs/1410.8849).

- 594 [29] P. Nason and G. Zanderighi, “ W^+W^- , WZ and ZZ production in the
595 POWHEG-BOX-V2”, *Eur. Phys. J.* **C74** (2014), no. 1, 2702,
596 doi:10.1140/epjc/s10052-013-2702-5, arXiv:1311.1365.
- 597 [30] J. M. Campbell and R. K. Ellis, “MCFM for the Tevatron and the LHC”, *Nucl. Phys. Proc.*
598 *Suppl.* **205** (2010) 10, doi:10.1016/j.nuclphysbps.2010.08.011,
599 arXiv:1007.3492.
- 600 [31] J. M. Campbell, R. K. Ellis, and C. Williams, “Bounding the Higgs width at the LHC
601 using full analytic results for $gg -> e^-e^+\mu^-\mu^+$ ”, *JHEP* **04** (2014) 060,
602 doi:10.1007/JHEP04(2014)060, arXiv:1311.3589.
- 603 [32] J. Alwall et al., “The automated computation of tree-level and next-to-leading order
604 differential cross sections, and their matching to parton shower simulations”, *JHEP* **07**
605 (2014) 079, doi:10.1007/JHEP07(2014)079, arXiv:1405.0301.
- 606 [33] C. Collaboration, “Measurements of properties of the higgs boson in the four-lepton final
607 state in proton-proton collisions at $\sqrt{s} = 13$ TeV”, CMS-PAS-HIG-19-001 (2019).
- 608 [34] CMS Collaboration, “Measurement of the properties of the Higgs boson in the
609 four-lepton final state at $\sqrt{s} = 13$ TeV”, CMS Physics Analysis Note CMS-AN-15-277,
610 2016.
- 611 [35] CMS Collaboration, “Measurement of the properties of the higgs boson in the four-lepton
612 final state at $\sqrt{s} = 13$ tev”, CMS Physics Analysis Note CMS-AN-15-277, 2016.
- 613 [36] CMS Collaboration, “Measurement of differential cross sections for Higgs boson
614 production in the diphoton decay channel in pp collisions at $\sqrt{s}=8$ TeV”, *Eur. Phys. J. C*
615 **76** (2015) 13, doi:10.1140/epjc/s10052-015-3853-3, arXiv:1508.07819.
- 616 [37] ATLAS and CMS Collaborations, LHC Higgs Combination Group, “Procedure for the lhc
617 higgs boson search combination in summer 2011”, ATL-PHYS-PUB/CMS NOTE 2011-11,
618 2011/005, CERN, 2011.
- 619 [38] G. Cowan, K. Cranmer, E. Gross, and O. Vitells, “Asymptotic formulae for
620 likelihood-based tests of new physics”, *Eur. Phys. J. C* **71** (2011) 1554, doi:10.1140/
621 epjc/s10052-011-1554-0, 10.1140/epjc/s10052-013-2501-z,
622 arXiv:1007.1727.